Spatiotemporal dynamics of photoexcited quasiparticles in two-dimensional crystals studied by ultrafast laser techniques

By

Nardeep Kumar

Submitted to the Department of Physics and Astronomy and the
Graduate Faculty of the University of Kansas
in partial fulfillment of the requirements for the degree of
Doctor of Philosophy

Committee members

Dr. Hui Zhao, Chairperson

Dr. Hsin-Ying Chiu

Dr. Wai-Lun Chan

Dr. Kyoungchul Kong

Dr. Shenqiang Ren

Date defended: August 26, 2014

The Dissertation Committee for Nardeep Kumar certifies
that this is the approved version of the following dissertation :

Spatiotemporal dynamics of photoexcited quasiparticles in two-dimensional crystals studied by ultrafast laser techniques

Dr. Hui Zhao, Chairperson

Date approved: August 28, 2014

Abstract

Layered materials in which atomic sheets are stacked together by weak van der Waals forces can be used to fabricate two-dimensional systems. They represent a diverse and rich, but largely unexplored, source of materials. Atomically-thin structures derived from these materials possess a number of interesting electrical, optical, and mechanical properties, and are attractive for new nanodevices. For their applications in semiconductor industry, it is necessary to understand the dynamics of photoexcited quasiparticles that occur on ultrafast time scales of less than one nanosecond. In this dissertation, I discuss ultrafast optical experimental techniques and results from various two-dimensional materials, which provide information about electronic dynamics. First, a second harmonic generation technique that can be used to find the crystalline orientation, thickness uniformity, layer stacking, and single-crystal domain size is discussed, with results presented on exfoliated and chemical vapor deposition MoS_2 samples. Second, a third harmonic generation technique is discussed, which can be used to explore nonlinear optical properties of materials, and results are presented on graphene and few-layer graphite films. Third, a spatially resolved femtosecond pump-probe is described, which can be used to study hot carrier and photoexcited phonon dynamics and results are presented on Bi_2Se_3 sample. Then, exciton dynamics in MoS_2 and $MoSe_2$ are explored by using transient absorption microscopy with a high spatiotemporal resolution. Finally, a polarization-resolved femtosecond transient absorption spectroscopy that can be used to study valley and spin dynamics is discussed, with results presented on monolayer, few-layer, and bulk $MoSe_2$ samples.

Acknowledgements

Being a graduate student at the University of Kansas (KU), I consider myself as one of the luckiest persons in the field of science. KU has given me a wonderful opportunity to fulfill my dreams with the help of number of great persons. I now acknowledge all those persons who helped me to successfully complete my dissertation.

First and foremost I thank my advisor, Dr. Hui Zhao, for his guidance and support during the course of my research work. It has been an honor to be his Ph.D. student. My first interaction with Dr. Zhao was in my first KU physics course, PHSX 631 - Electromagnetic Theory. I was blessed to meet such a great professor and as well as a great person. He makes a variety of topics so interesting and easy that even an unmotivated person can become motivated to learn more. From my childhood, I was passionate about astronomy and wanted to become an astronomer. After taking Dr. Zhao's class, I was so impressed by his teaching and hard work that I selected him as my Ph.D. advisor. I am very grateful to Dr. Zhao for employing me in his research group. In addition to helping me with the respective experiment-related skills, he has guided me toward career-related opportunities. He also has encouraged me to explore independent projects along with his given projects.

It is a great pleasure to express my appreciation to my lab mates Brian Ruzicka, Lalani Werake, Rui Wang, Frank Ceballos, Qiannan Cui, Chris Gerstenkorn, and Jiaqi He. I learned much from each of you. Each has been a wonderful colleague and assisted me in one way or another with the projects that were presented in this dissertation. I am especially grateful to Brian Ruzicka who helped me during my first major project and shared his experience and techniques. We worked together on the pump-probe study

of topological insulator experiment, and I very much appreciate his help in building the initial setup. I thank Qiannan Cui and Frank Ceballos for assisting me with the second harmonic microscopy of MoS_2 and exciton dynamics in $MoSe_2$ research, Rui Wang and Chris Gerstenkorn for their contributions to the third harmonic generation in graphene work, and Jiaqi He for his participation in the valley and spin dynamics in $MoSe_2$ project. Finally, I thank Lalani Werake, the first graduate student of Dr. Zhao's group, for sharing her experience and knowledge.

I also thank my dissertation committee members: Dr. Hsin-Ying Chiu, Dr. Wai-Lun Chan, Dr. Kyoungchul Kong, and Dr. Shenqiang Ren for their valuable time, interest, and helpful comments. I would like to specifically thank Dr. Hsin-Ying Chiu for providing us with the graphene samples and for sharing her student Jatinder Kumar, who fabricated graphite thin films on silicon substrate for the third harmonic generation experiment. I would also like to thank our several collaborators outside of KU. I owe thanks to Dr. Jun Lou, Dr. Pulickel M. Ajayan, and Sina Najmaei from Rice University for providing us with high quality chemical vapor deposition MoS_2 samples for the second harmonic microscopy of MoS_2 project. I would like to specifically thank Dr. Arthur L. Smirl from the University of Iowa for assisting us with the theoretical calculations for third harmonic generation in graphene project.

Also, I would like to acknowledge Dr. Johnpierre Paglione, Dr. Nicholas P. Butch, Paul Syers, and Kevin Kirshenbaum for providing us with high quality Bi2Se3 samples for the pump-probe study of topological insulator Bi_2Se_3 experiment. Finally, I also acknowledge Dr. Dawei He and Dr. Yongsheng Wang from Beijing Jiaotong University with whom we shared many useful discussions regarding exciton dynamics in Mos_2 and $MoSe_2$. I greatly appreciate all of our collaborators for their excellent work.

For financial support, I acknowledge the US National Science Foundation under Awards No. DMR-0954486 and No. EPS-0903806, and matching support from the State of Kansas through the Kansas Technology Enterprise Corporation. I also acknowledge

the financial supporters of our collaborators work: NSF MRSEC (DMR-0520471) and a DARPA-MTO award (N66001-09-c-2067), CNAM, the Welch Foundation (C-1716), the U.S. Army Research Office MURI grant W911NF-11-1-0362, the National Basic Research Program 973 of China (Grants No. 2011CB932700 and No. 2011CB932703), the Chinese Natural Science Foundation (Grants No. 61335006, No.61378073, and No. 61077044), and the Beijing Natural Science Foundation (Grant No. 4132031).

Finally, I express the greatest gratitude to my family and friends for all their support and encouragement during my time as a graduate student.

Contents

List of Figures

List of publications

1. N. Kumar, J. He, D. He, Y. Wang, and H. Zhao,"Valley and Spin Dynamics in $MoSe_2$ Two-Dimensional Crystals", *Nanoscale*(2014). DOI: 10.1039/C4NR03607G

2. N. Kumar, Q. Cui, F. Ceballos, D. He, Y. Wang, and H. Zhao,"Exciton diffusion in monolayer and bulk $MoSe_2$", *Nanoscale* 6, 4915 (2014).

3. N. Kumar, Q. Cui, F. Ceballos, D. He, Y. Wang, and H. Zhao,"Exciton-exciton annihilation in $MoSe_2$ monolayers", *Phys. Rev. B* 89, 125427 (2014).

4. N. Kumar, S. Najmaei, Q. Cui, F. Ceballos, P.M. Ajayan, J. Lou, and H. Zhao,"Second harmonic microscopy of monolayer MoS_2", *Phys. Rev. B* 87, 161403(R) (2013).

5. N. Kumar, J. Kumar, C. Gerstenkorn, R. Wang, H.Y. Chiu, A.L. Smirl, and H. Zhao,"Third harmonic generation in graphene and graphite thin films", *Phys. Rev. B* 87, 121406(R) (2013).

6. N. Kumar, J. He, D. He, Y. Wang, and H. Zhao,"Charge carrier dynamics in bulk MoS_2 crystal studied by transient absorption microscopy", *J. Appl. Phys.* 113, 133702 (2013).

7. N. Kumar, B.A. Ruzicka, N.P. Butch, P. Syers, K. Kirshenbaum, J. Paglione, and H. Zhao,"Spatially resolved femtosecond pump-probe study of topological insulator Bi_2Se_3", *Phys. Rev. B* 83, 235306 (2011).

8. K. He, N. Kumar, L. Zhao, Z. Wang, K.F. Mak, H. Zhao, and J. Shan,"Tightly Bound Excitons in Monolayer WSe_2", *Phys. Rev. Lett.* 113, 026803 (2014).

9. Q. Cui, F. Ceballos, N. Kumar, and H. Zhao,"Transient Absorption Microscopy of Monolayer and Bulk WSe_2", *ACS Nano* 8, 2970 (2014).

10. R. Wang, H.C. Chien, J. Kumar, N. Kumar, H.Y. Chiu, and H. Zhao,"Third-Harmonic Generation in Ultrathin Films of MoS_2", *ACS Appl. Mater. Interfaces* 6, 314 (2014).

11. C. Rochford, N. Kumar, J. Liu, H. Zhao, and J. Wu,"All-Optical Technique to Correlate Defect Structure and Carrier Transport in Transferred Graphene Films", *ACS Appl. Mater. Interfaces* 15, 7176 (2013).

12. M. Gong, A. Kirkeminde, N. Kumar, H. Zhao, and S. Ren,"Ionic-passivated FeS_2 photocapacitors for energy conversion and storage", *Chem. Commun.* 49, 9260 (2013).

13. R. Wang, B.A. Ruzicka, N. Kumar, M.Z. Bellus, H.-Y. Chiu, and H. Zhao,"Ultrafast and spatially resolved studies of charge carriers in atomically thin molybdenum disulfide", *Phys. Rev. B* 86, 045406 (2012).

14. B.A. Ruzicka, N. Kumar, S. Wang, K.P. Loh, and H. Zhao,"Two-probe study of hot carriers in reduced graphene oxide", *J. Appl. Phys.* 109, 084322 (2011).

List of Symbols and Abbreviations

2D	Two dimensional
3D	Three dimensional
B	Magnetic flux density
c	Speed of light
CCD	Charge-coupled device
CVD	Chemical Vapor Deposition
D	Diffusion coefficient
D	Electric flux density
e	Magnitude of electron charge
E	Electric field
E_g	Band gap energy
f_{rep}	Laser repetition rate
FWHM	Full width at half maximum
g(E)	Density of states
H	Magnetic field
J	Electric current density
J_d	Drift current density
J_f	Diffusion current density
k_B	Boltzmann constant
n	Index of refraction
N	Photoexcited quasiparticle density

N_s	Saturation density
$\mathbf{P}$	Material polarization
R	Reflectance
R_0	Reflection of the probe with no pump
SHG	Second harmonic generation
THG	Third harmonic generation
TMDs	Transition metal dichalcogenides
v_d	Drift velocity
v_F	Fermi velocity
v_g	Group velocity
α_0	Absorption coefficient
χ	Electric susceptibility
$\Delta R/R_0$	Differential reflection
ΔR	Change in reflection of the probe caused by the pump
ε_0	Permittivity of free space
ε_r	Relative permittivity of a medium
$\hbar$	Reduced Planck's constant
μ_0	Permeability of free space
ρ	electric charge density

Chapter 1

Introduction

1.1 Motivation and introduction to materials studied

The development of silicon has brought the electronics industry to a different level. Due to its remarkable properties and many advantages, including abundance on earth, stable oxide formation, and low cost, silicon has been the best choice for the semiconductor industry for many decades. The performance of electronic devices have greatly improved as a consequence of reducing their component sizes. However, the currently implemented feature sizes are close to the physical limits. As a result, research on alternatives to silicon, particularly those with reduced dimensions, has increased.

In this dissertation, the focus is on newly discovered two-dimensional (2D) crystals including graphene, bismuth selenide (Bi_2Se_3), molybdenum disulfide (MoS_2), and molybdenum diselenide ($MoSe_2$).

Carbon exists in many forms. The two best-known forms of elemental carbon, diamond and graphite, have been examined for several centuries. Although both forms only differ by the arrangement of the carbon atoms, they are very different in terms of physical properties. In diamonds, each carbon atom is strongly bonded by covalent bonds to four other carbon atoms. This gives the diamond crystalline structure a tetrahedral shape. Graphite is made up of layers of thin sheets of

carbon atoms possessing strong covalent bonds between the atoms but weak van der Waals forces between the layers. These layers are called graphene. Graphene is considered a miracle material due to its extraordinary properties.

The interest in 2D systems began with the isolation of these single sheets of carbon atoms from the parent bulk graphite.[8] Graphene exhibits a number of unusual and remarkable transport properties that make it attractive for nanoelectronic applications,[9–11] including high mobility[8,11–13] and nearly ballistic transport at room temperature.[12,14] However, it is the optical properties of graphene that are of primary interest in this dissertation.

Nonlinear optical processes are good tools to understand material properties, including structural symmetry or band structure. Graphene is considered to have a strong nonlinear optical response. However, second-order nonlinearities in graphene are expected to be weak because of symmetry considerations. For example, graphene mounted on a substrate has C_{6v} symmetry. Therefore, the only allowed sources of second-order responses are the interfaces.[15] On the other hand, the third-order response is not restricted by the inversion symmetry. In this dissertation, I will discuss third harmonic generation in graphene.

Graphene is a very good 2D material to investigate nonlinear optical effects. However, pristine graphene lacks a proper bandgap, a critical property for electronic devices. It is possible to generate a bandgap in graphene but carrier mobility is sacrificed.

Following the discovery of graphene, another group of layered materials, called transition metal dichalcogenides (TMDs), has attracted significant attention. Unlike graphene, thin films of TMDs behave like semiconductors possessing a large bandgap. As a result, TMDs are promising candidates for electronic device materials. In this dissertation, research related to two key examples of TMDs, MoS_2 and $MoSe_2$, will be discussed.

Monolayer MoS_2 is a direct semiconductor with a bandgap in the visible-light range. Investigations on MoS_2's potential applications in logic electronics were stimulated by MoS_2's large bandgap and its structural similarity with the widely-studied graphene.[16,17] Since monolayer MoS_2's bandgap resides in the visible range, it is an attractive candidate for various optoelectronic

and photonic applications, such as phototransistors[18,19] and heterojunction solar cells.[20] An added benefit of MoS_2 is that it has work functions that are compatible with commonly used electrode materials. Finally, MoS_2 has stable charge exciton states even at room temperature,[21] making it an ideal material for optoelectronic applications.

While breakthroughs in the understanding of the mechanical, electronic, and linear optical properties of MoS_2 atomic layers have been made, little is known about their nonlinear optical properties and exciton dynamics. Nonlinear optical responses are important aspects of light-matter interactions and can play important roles in various photonic and optoelectronic applications, especially in those involving high-intensity laser beams. As mentioned earlier, graphene has inversion symmetry, making its second-order response vanish. However, odd thin layers of MoS_2 are non-inversion symmetric. Moreover, bulk and even layers of MoS_2 are centrosymmetric. For the sake of understanding, the nonlinear optical properties and second harmonic generation microscopy of monolayer MoS_2 are studied in this dissertation.

In addition, a transient absorption microscopy of bulk MoS_2 will also be discussed in this dissertation. Studies on bulk MoS_2 can provide complementary information for understanding monolayers and their interaction with environments and substrates, since the properties of monolayer MoS_2 are different from, but related to, the bulk.

Monolayer $MoSe_2$ possesses a similar structure as MoS_2 and exhibits several properties that make it an attractive alternative. For example, $MoSe_2$'s direct bandgap is close to the optimal bandgap value of single-junction photovoltaic devices. Several studies have demonstrated applications of $MoSe_2$ in photovoltaic[22,23] and photocatalysis.[24] Few-layer $MoSe_2$ has nearly degenerate direct and indirect bandgaps. Hence, it is possible to modulate the nature of the bandgap, and therefore control its optical properties, via temperature[25] and strain.[25,26] It was proposed that these 2D crystals can be used as building blocks to fabricate new van der Waals heterostructures and even new 3D crystals.[27–29] Very recently, such structures have been fabricated and investigated for applications in photovoltaics,[30] vertical field-effect tunneling transistors,[31,32] and memory devices.[33] $MoSe_2$ is expected to play an important role in this new form of material discovery and design.

TMDs have unique spin and valley properties.[34–36] Hence, they have emerged as promising materials for spintronics[37–39] and valleytronics,[40] where the spin degree of freedom or the valley index of electrons is used for information processing. In this dissertation, I also demonstrate optical injection and detection of valley- and spin-polarized excitons in $MoSe_2$ monolayers at room temperature by polarization-resolve transient absorption measurements.

Along with graphene and TMDs, another important novel 2D material, Bi_2Se_3, will also be discussed in this dissertation. Bi_2Se_3 is a member of topological insulator family. As a new insulating state of matter, a topological insulator behaves like a bulk insulator with a large bandgap in its interior, but with a gapless surface state that is protected by time-reversal symmetry.[41–44] Two-dimensional topologically protected edge states, also known as quantum spin Hall effect, were predicted in 2005,[45] and soon thereafter demonstrated in mercury telluride (HgTe) quantum wells.[46] More recently, three-dimensional bulk topological insulators were also predicted[47,48] and demonstrated in several binary bismuth compounds.[49–51]

1.2 Overview of the dissertation

The majority of the work presented in this dissertation belongs to photoexcited quasiparticles. The basic structure of my dissertation are as follows.

In Chapter 2, a general theory of optics, with emphasis on nonlinear optics, will be discussed. This chapter includes the concepts of the nonlinear interactions between light and matter. Two important aspects of nonlinear interactions between light and matter, one relating to second-order nonlinearity and the other corresponding to third-order nonlinearity, are also discussed.

In Chapter 3, experimentation detailing second- and third-order nonlinearity will be discussed, with results on MoS_2 and graphene presented. Experiments associated with second-order nonlinearity show that the lack of inversion symmetry in monolayer MoS_2 allows a strong optical second harmonic generation.

Chapter 4 begins with a theoretical discussion of photoexcited quasiparticle dynamics in 2D

materials and is followed, in chapter 5, by possible experimental techniques to probe such dynamics.

In Chapter 6, results on photoexcited quasiparticle dynamics of Bi_2Se_3, MoS_2, and $MoSe_2$ will be shared. This chapter has three sections. In the first section, carrier and phonon dynamics in Bi_2Se_3 crystal are studied through a spatially resolved ultrafast pump-probe technique. Pronounced oscillations in differential reflection are observed with two distinct frequencies. In the second section, a transient absorption microscopy study of exciton dynamics in bulk MoS_2 crystals at room temperature is given. In the final section of Chapter 6, a study of excitonic dynamics in $MoSe_2$ monolayer and bulk samples by femtosecond transient absorption is examined. The study shows a strong density-dependent initial decay of the exciton population in monolayers, which can be well described by the exciton-exciton annihilation.

Chapter 7 and Chapter 8 are extensions of Chapter 5 and Chapter 6. They include investigations of photoexcited quasiparticle diffusion coefficient in MoS_2, $MoSe_2$, and Bi_2Se_3. In Chapter 7, a theoretical description of diffusive transport is given followed by experimentation and results in Chapter 8.

Chapter 9 focuses on valley and spin dynamics in monolayer $MoSe_2$ by polarization resolved femtosecond transient absorption spectroscopy. Valley- and spin-polarized excitons are injected by a circularly polarized pulse, with an excess energy of 120 meV. Relaxation of the valley polarization is time-resolved by measuring dynamical circular dichroism of a linearly polarized probe pulse tuned to 790 nm, which is the peak of the exciton resonance of monolayer $MoSe_2$.

Finally, Chapter 10 provides conclusions and discusses possible future work based on the similar experimental techniques.

Chapter 2

Theoretical foundation of optics

2.1 Introduction

In material science, one of the key techniques to study material properties are spectroscopy techniques, which belong to the study of matter through its interaction with electromagnetic radiation. Classically, the ligh-matter interactions are a result of an oscillating electromagnetic field interacting with the electrons of the atoms and molecules of the material. Light matter interactions give rise to various optical processes, such as absorption, transmission, reflection, scattering etc., which are very useful to study optical properties of materials. The electromagnetic theory of optics begins with Maxwell's equations,

$$\nabla \cdot \vec{D} = 4\pi\rho, \tag{2.1}$$

$$\nabla \cdot \vec{B} = 0, \tag{2.2}$$

$$\nabla \times \vec{E} = -\frac{1}{c} \cdot \frac{\partial \vec{B}}{\partial t}, \tag{2.3}$$

$$\nabla \times \vec{H} = \frac{4\pi}{c}\vec{J} + \frac{1}{c} \cdot \frac{\partial \vec{D}}{\partial t}, \tag{2.4}$$

where $\vec{E}$ is the electric field, $\vec{D}$ the electric flux density or displacement, $\vec{H}$ the magnetic field, $\vec{B}$ the magnetic flux density, $\vec{J}$ the electric current density, and ρ the electric charge density. The electric

and magnetic flux densities are defined as

$$\vec{D} = \varepsilon_0 \vec{E} + \vec{P}, \tag{2.5}$$

$$\vec{B} = \mu_0 \vec{H} + \vec{M}, \tag{2.6}$$

where $\vec{P}$ is the polarization and $\vec{M}$ is the magnetization of the optical medium, ε_0 and μ_0 are called permittivity and permeability of free space respectively. We see from above relations that optical characteristics of a medium in presence of electromagnetic radiation are completely determined by how $\vec{P}$ and $\vec{M}$ react to the electromagnetic field.

2.2 Linear interactions between light and matter

Interaction between light and matter can often be assumed to be linear, when the light intensity is relatively low. In this regime, the electric field of light induces a polarization given by,

$$\vec{P} = \varepsilon_0 \chi \vec{E}, \tag{2.7}$$

here χ is the linear susceptibility, which is related to the dielectric constant by,

$$\varepsilon_r = 1 + \chi. \tag{2.8}$$

Usually, the real and imaginary parts of ε_r determines the index of refraction and absorption coefficient, respectively. When light propagate in a solid, these two parameters describes the retardation and attenuation of light caused by the material. Since χ is the foundation of linear optical properties of materials, theoretical and experimental studies of χ of various materials are a major part of optical studies of materials.

The χ, as well as its spectrum, of most materials are well known. When exploring new materials, χ is often among the first set of material parameters to measure. From a fundamental point

of view, since χ is determined by electronic structure and lattice properties, it can reveal even more fundamental properties of materials. For example, absorption spectroscopy is often used to determine the energy bandgap of materials. It is also well known that χ changes with the state of the material, like temperature, pressure, and energy distribution of electrons. For example, when electrons are excited from lower to higher energy levels, absorption coefficient at the wavelength corresponding to the energy difference of these two levels is reduced, because the occupation of the excited level prevent further excitation of electrons to that level. This effect is known as phase-state filling. Although the change of the absorption coefficient if often small, this effect is the foundation transient absorption spectroscopy, which has important applications in time-resolved studies of electronic dynamics.

2.3 Nonlinear interactions between light and matter

As mentioned earlier for a small electric field, the relation between electric field and polarization is linear. However, this linear relationship breaks if the electric field is comparable to interatomic electric fields, typically 10^5 to 10^8 V/m. In other words higher order susceptibilities come into play when the light's electric field becomes sufficiently large. At this point the electric polarization depends on higher powers of the electric field,[15]

$$\overrightarrow{P}(t) = \varepsilon_0[\chi^{(1)}\overrightarrow{E}(t) + \chi^{(2)}\overrightarrow{E}^2(t) + \chi^{(3)}\overrightarrow{E}^3(t) + ...].$$

2.3.1 Second order nonlinear susceptibility

The second-order polarization,

$$\overrightarrow{P}^2(t) = \varepsilon_0\chi^{(2)}\overrightarrow{E}^2(t), \tag{2.9}$$

gives rise to several second-order nonlinear optical processes, such as second harmonic generation(SHG), sum frequency generation (SFG), difference frequency generation (DFG) or optical

rectification (OR).

In the SHG process, a laser beam with electric field of

$$\overrightarrow{E}(t) = Ee^{(-\iota\omega t)} + c.c., \tag{2.10}$$

is incident upon a crystal for which the second order susceptibility, $\chi^{(2)}$ is non-zero. The nonlinear polarization that is created in such a crystal is given by,[15]

$$\overrightarrow{P}^2(t) = 2\varepsilon_0\chi^{(2)}EE^* + \varepsilon_0\chi^{(2)}E^2e^{-\iota 2\omega t} + c.c.. \tag{2.11}$$

We see that the second-order polarization consist of a contribution zero frequency (the first term) and a contribution at frequency 2ω (the second term). This latter contribution can lead to the generation of the radiation at the second-harmonic frequency.

2.3.2 Third order nonlinear susceptibility

The third-order contribution to the nonlinear polarization is given by,

$$\overrightarrow{P}^3(t) = \varepsilon_0\chi^{(3)}\overrightarrow{E}(t)^3. \tag{2.12}$$

If the incident light is monochromatic, the third order polarization is

$$\overrightarrow{P}^3(t) = \frac{1}{4}\varepsilon_0\chi^{(3)}\varepsilon^3 cos3\omega t + \frac{3}{4}\varepsilon_0\chi^{(3)}\varepsilon^3 cos\omega t. \tag{2.13}$$

The first term in the above equation describes a response at frequency 3ω that is created by an applied field at frequency ω. This term leads to the process of third-harmonic generation.

Chapter 3

Harmonic generation in 2D crystals

3.1 Second harmonic generation in MoS_2

3.1.1 Introduction

Recently, significant research has been focused on exploring new types of atomically thin crystals based on layered materials, such as transition metal dichalcogenides (TMDs), MX_2 (M=Mo, W; X=S, Se, Te).[52] The most extensively studied member of this family is MoS_2. In 2010, photoluminescence experiments[53,54] and microscopic calculations[54,55] indicated that, although bulk MoS_2 is an indirect semiconductors, its monolayer is a direct semiconductor with a bandgap of about 1.88 eV. In recent years, based on MoS_2, many devices such as top-gated transistors, integrated circuits for logic operations, p-n-junction based devices, flexible electronics, phototransistors and heterojuctions solar cells are demonstrated.[18–20,56–62]In addition to the mechanical, electronic, and linear optical properties of TMDs, non-linear optical properties are also very crucial to various photonic and optoelectronic applications.

Symmetry plays an important role in linear and nonlinear optical properties of materials. Bulk 2H polytype and even thin films of MoS_2 belong to space group D_{6h} and are inversion symmetric. By symmetry, their second order nonlinear response should be zero.[15] On the other hand odd number of layers of MoS_2 are noncentrosymmteric and hence, have strong second order nonlinear

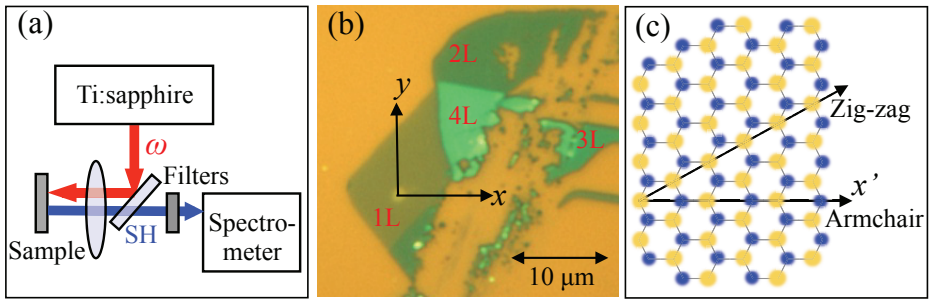

Figure 3.1: (a) Schematics of the experimental setup. (b) Microscope image of a mechanically exfoliated MoS_2 flake. (c) Lattice structure of monolayer MoS_2. Data from Kumar *et al.*[1]

response.

3.1.2 Experimental conditions and band structure of MoS_2

Figure 3.1(a) shows the experimental setup. Second harmonic generation experiments were performed with a Ti:sapphire laser, providing 130 fs fundamental pulses at 810 nm with an angular frequency ω. The fundamental pump beam was focused at an angle of incidence of 90° onto the samples using a 0.12 numerical aperture microscope objective, to a Gaussian spot of 2 μm full width at half maximum (FWHM). The 410 nm SHG was collected by the same lens, optically filtered and detected using a spectrometer equipped with a thermoelectric cooled silicon charge-coupled device camera.

Figure 3.1(b) represents a microscopic image of mechanically exfoliated MoS_2 onto a Si/SiO_2 substrate of 90 nm SiO_2 thickness. By measuring the optical contrast,[63–65] Raman spectrum,[66,67] photoluminesence spectrum[53,54] and relative optical contrast, the number of MoS_2 layers are identified as 1L for monolayer, 2L for bilayer, 3L for trilayer and 4L for quadrilayer layer. Simplified geometry of monolayer MoS_2 is schematically shown in Fig. 3.1(c), where each yellow circle represents two S atoms vertically separated by 0.65 nm, and blue circles indicate plane of Mo atoms located between the two S atomic planes.

3.1.3 SHG in mechanically exfoliated MoS_2 samples

The MoS_2 crystal possesses D_{3h} symmetry. With the D_{3h} symmetry, the second-order nonlinear susceptibility tensor has nonzero elements of $\chi^{(2)}_{y'y'y'} = -\chi^{(2)}_{y'x'x'} = -\chi^{(2)}_{x'x'y'} = -\chi^{(2)}_{x'y'x'} \equiv \chi^{(2)}$,[15] where $x'y'z'$ are crystalline coordinates. Here, x' is along the armchair direction, which is 30° from the zig-zag direction, along which the mirror symmetry is broken. In the experiment, the fundamental beam is normal incident (along $-z'$) and is linearly polarized along horizontal direction [defined as x in the laboratory coordinates, as shown in Fig. 3.1(b)]. It is straightforward to show that the parallel (x) and perpendicular (y) components of SH field are proportional to $\sin 3\theta$ and $\cos 3\theta$, respectively, where θ is the angle between x and x'. Hence, the power of the two components varies as $P_x \propto \sin^2 3\theta$ and $P_y \propto \cos^2 3\theta$, while the total power is independent of θ.

3.1.4 Experimental results from mechanically exfoliated sample

Figure 3.2 summarize the SH signal from mechanically exfoliated thin films and bulk MoS_2 flakes. The spectra of the SH light (405nm), from monolayer MoS_2, produce by pump beam (810nm) with an average power of 4mW is shown in the upper inset of Fig. 3.2(a). By removing the color filters used to block fundamental, the spectra of the fundamental was detected with the same detector and the results is plotted on right hand side in the upper inset of Fig. 3.2(a). From the wavelengths of SH and fundamental, we confirm that, SH signal is indeed a SHG.

To further confirm whether it is from MoS_2 flake, we study the bare substrate under the same conditions. The data from the bare substrate is shown by the gray curve in the upper inset of Fig. 3.2(a). The contrast of the monolayer with respect to the substrate is about 10^4 , which is much higher than linear optical microscopy (about 0.3). The main panel of Fig. 3.2(a) shows, the SH signal power dependence w.r.t. the fundamental power. The peak irradiance of the fundamental and SH pulses, deduced from the powers, are also plotted for convenience, as top and right axes.

The solid line shows the expected quadratic dependence of the SH signal on the fundamental intensity. Quadratic response is an another confirmation for its SH character. We also measure the total power of the SH from different thickness MoS_2 flakes shown in Fig. 3.1(b), with a fun-

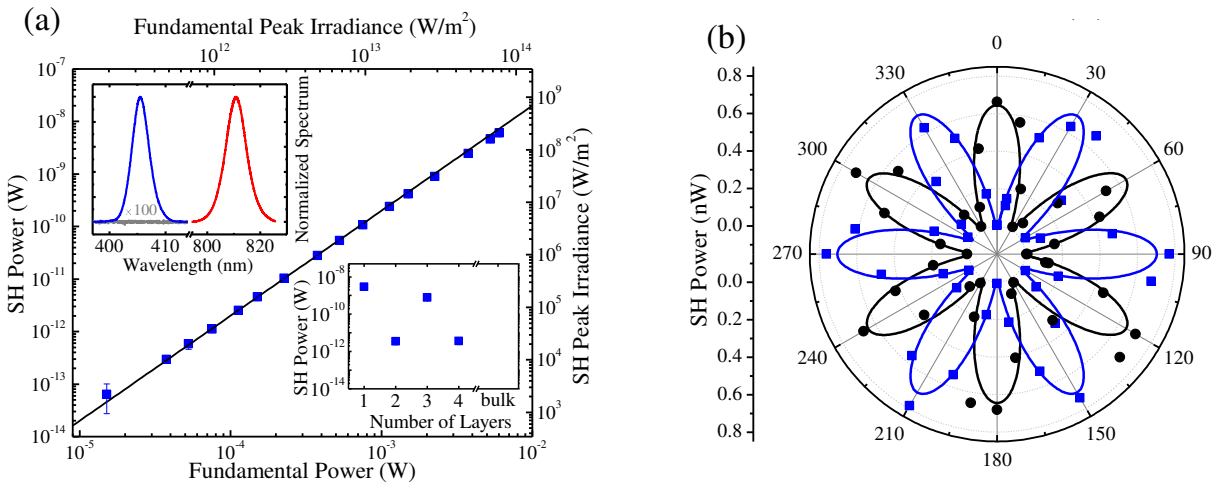

Figure 3.2: Second harmonic generation from mechanically exfoliated MoS_2 sample: The upper inset of (a) shows the spectra of second harmonic from the monolayer MoS_2 and from bare substrate (gray, multiplied by a factor of 100), as well as the fundamental beams (red). The lower inset shows the second harmonic power measured from regions with different atomic layers. The main panel of (a) shows the power dependence of second harmonic generation, with the solid line indicating the expected quadratic dependence. (b) Power of parallel (blue squares) and perpendicular (black circles) components of second harmonic as a function of θ, the angle between the laboratory and the crystalline coordinates. The blue (black) solid line indicates the expected $\sin^2 3\theta$ ($\cos^2 3\theta$) dependence. Data from Kumar *et al.*[1]

damental power of 4 mW.The results are summarized in the lower inset of Fig. 3.2(a). Since the total power is independent of θ, the measurement is not influenced by potentially different crystal orientations of these regions.

From thickness dependence SHG, we see that the second order response of trilayer is about a factor of seven smaller than the monolayer, while those of the bilayer and quadralayer are about two orders of magnitude smaller than the monolayer. Since flakes with an even number of atomic layers are centrosymmteric, their second-order response should be zero. The smaller but nonzero SH signal from even number of atomic layers can be attributed to surface and interface effects. Our measurement shows that the SH intensity of monolayer is 10^4 times stronger that bilayer and quadralayer. A thick exfoliated MoS_2 flake that can be considered as a bulk MoS_2 sample shows a very weak SH response, as expected, as a results of centrosymmetry, about five orders of magnitude smaller than the monolayer.

Next, by placing a linear polarizer in front of the spectrometer, we measure P_x and P_y as a

function of θ, the angle between x and x', by rotating the sample about z axis. To obtain this orientation dependence of the SH response, we mount the sample on a high precision rotation stage for the sake of keeping the sample position stable at the pump focus. Figure 3.2(b) shows the results, along with the expected θ dependence (solid lines) from the D_{3h} symmetry.

3.1.5 SHG in CVD MoS_2 samples

The observed SHG can be used to fast and *in-situ* characterize atomically thin films of MoS_2 and similar materials. Although high quality monolayer MoS_2 can be produced by simple mechanical exfoliation[68] and identified by optical contrast with certain substrates[63,64] and Raman spectroscopy,[66,67] applications of this material rely on development of scalable techniques. Following initial works of mechanical exfoliation, other top-down methods with better potential for large-scale production have been developed, such as lithium ion exfoliation[69–73] and ultrasonic exfoliation in liquids.[74–80] Promising progresses have also been made in developing bottom-up methods, including hydrothermal syn[81,82] and CVD on insulating substrates[83–86] and graphene.[87]

However, one significant obstacle is the lack of techniques for fast and *in-situ* sample characterization. For example, thin films of MoS_2 fabricated by these techniques are polycrystalline. They are composed of single-crystalline domains with random crystal orientations and are separated by grain boundaries, which severely limit performance of the films, especially their conductivity and mechanical strength. However, it is difficult to locate the grain boundaries and monitor size of these domains *in-situ*.

The lower inset of Fig. 3.3(a) shows a microscope photo of some triangular monolayer MoS_2 flakes on a Si/SiO_2(280 nm) substrate fabricated by CVD. The samples were prepared using MoO_3 and sublimated sulfur as precursors. MoO_3 is positioned close to the designated growth substrate at the center of the furnace, while sublimated sulfur is positioned upstream at a zone where evaporation starts at 750°C. The reaction of the precursors at 850°C in a furnace flushed with nitrogen results in nucleation of single crystalline domains. The density of nucleation and samples sizes can be controlled by monitoring the pressure and the closely related sulfur concentration in the

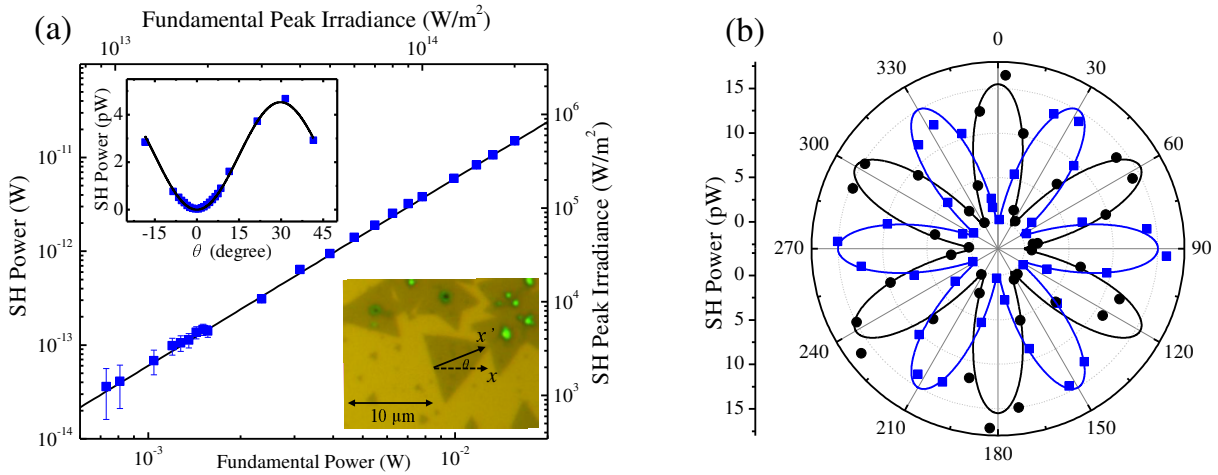

Figure 3.3: Second harmonic generation from a triangular monolayer MoS_2 flake grown by CVD, as shown in the lower inset of (a). The main panel of (a) shows the power dependence of second harmonic generation. The solid line indicates the expected quadratic dependence. Panel (b) shows angular dependence of the parallel (blue squares) and perpendicular (black circles) components of second harmonic, along with the expected dependence (solid lines). The upper inset of (a) shows a separate measurement of the parallel component with a finer step size near $\theta = 0°$. Data from Kumar *et al.*[1]

chamber. By maintaining a positive pressure in the range of 5 - 20 KPa, MoS_2 domains with sizes in the range of 10 - 40 μm are synthesized, with a ramping time of 60 to 90 minutes and 10 minutes at the reaction temperature.[88]

The main panel of Fig. 3.3(a) shows the quadratic power dependence of SHG, similar to Fig. 3.2(a), measured from the well-separated flake on which the crystalline and laboratory coordinates (x' and x, respectively) are plotted [the lower inset of Fig. 3.3(a)]. By rotating the sample, we measure P_x and P_y as a function of θ, as shown in Fig. 3.3(b). The results are similar to the exfoliated sample shown in Fig. 3.2(b). A separate measurement of the parallel component with finer resolution near $\theta = 0°$, shown in the upper inset of Fig. 3.3(a), confirms that the minimal parallel component occurs precisely at $\theta = 0°$. The edges of these triangular flakes are expected to be along zig-zag directions since these are lowest energy configurations.[89,90] The maximum parallel component of SH should occurs when the fundamental is polarized along the zig-zag direction, which is consistent our observation.

Hence, the SHG further confirms that the direction of the edges is zig-zag. We repeat the

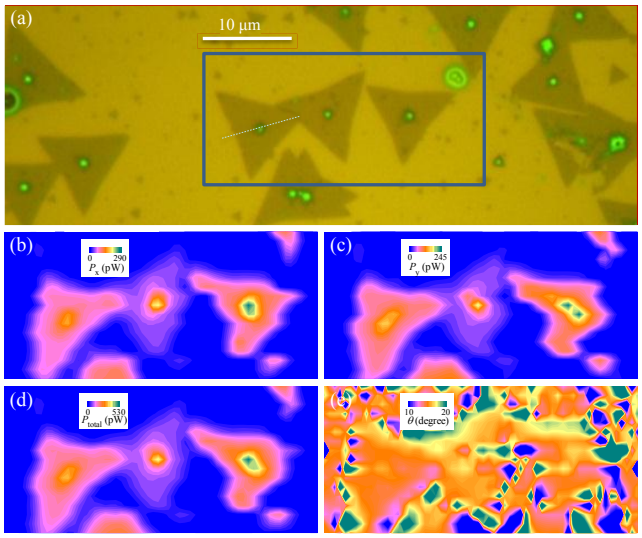

Figure 3.4: (a) Optical microscopy photo of a region of substrate containing flakes grown by CVD. (b) and (c): Maps of P_x and P_y over the region indicated by the box in (a). (d) Map of the total power, $P_x + P_y$. (e) Map of θ calculated from (b) and (c). Data from Kumar *et al.*[1]

measurement with several other similar triangular flakes, and obtained the same result. Such an established relation also allows us to determine the crystal orientation of the mechanically exfoliated sample shown in Fig. 3.1(b): that is, the armchair direction of the 1L region is horizontal, and its lattice orientation is as shown in Fig. 3.1(c).

3.1.6 Feasibility of polarization-revolved SH microscopy

Figure 3.4 summarizes our proof-of-principle demonstration of a polarization-revolved SH microscopy. We study a region on the substrate with quasi-continuos films, as shown in Fig. 3.4(a). It contains a high density but still separated and randomly oriented triangular flakes, so that we can correlate domains observed in SHG to the actual regions. In this measurement, we scan a 20-mW fundamental spot across the region indicated by the box in Fig. 3.4(a), and detect the powers of the parallel and perpendicular components of the SH, as shown in Figs. 3.4(b) and (c), respectively. The errors in these scans are below 2 pW, or smaller than 1% of the maximum signal. Figure 3.4(d) shows the total power, obtained by adding (b) and (c). From (b) and (c), we calculate the angle by using $\theta = (1/3)\tan^{-1}\sqrt{P_x/P_y}$, as shown in (e). The uncertainty on the angle is below 1°.

The combination of linear and nonlinear optical microscopy can provide valuable information on polycrystalline thin films grown by CVD. First, the greenish dots at the central area of some triangles in Fig. 3.4(a) show *higher* SH power and hence behave as uncoupled monolayers. In bilayer MoS_2 exfoliated from $2H$-stacked crystals, the two layers are inversely oriented so that the bilayer possesses inversion symmetry. Hence, it second-order response should vanish, as confirmed in Fig. 3.2(a).

The higher SH power observed from multilayer regions of CVD-grown flakes indicates that these multilayers are not $2H$-stacked. This is similar to multilayer graphene grown by CVD. Clearly, the SH microscopy is capable of probing relative orientations among multilayers of MoS_2. Second, panel (e) shows that θ is uniform over the left flake, which is about 15°. This is consistent with the shape observed in (a) (white dashed line). With further growth time, this flake will merge with other flakes to form a continuous polycrystalline film. Linear optical microscopy would not allow identification of each single-crystalline domains. However the θ map can still distinguish these domains, locate their boundaries, and measure their sizes. Third, the shapes of these flakes are irregular in the SH maps. Especially, the parallel and perpendicular components have different edge shapes. This can be attributed to the roughness on the edges and different termination configurations on the edges.

Although further characterizations are needed to correlate the microscopic structure on the edges to the SH power, this observation illustrates the potential of using SHG to study these edge structures. Finally, although the three flakes look similar in (a), the SH power are different, and the θ of the middle and right flakes are irregular. This illustrates that the SH microscopy can show different properties and qualities of the flakes that the linear optical microscopy cannot. However, further studies are needed to correlate SHG to these specific sample characteristics.

3.1.7 Estimation of second order susceptibility

In order to estimate the magnitude of the second order nonlinear susceptibility $\chi^{(2)}$ from the our measurements, we model the monolayer as a bulk medium. In our case, the SH signal is not

influenced by phase-matching conditions because monolayer MoS_2 thickness ($d = 0.65$ nm) is much smaller than the coherence length. By solving the coupled-wave equations,[15] the SH field amplitude of the parallel component is of the form,

$$\mathscr{E}_x = \frac{1}{4}\frac{i2\omega}{2n_{2\omega}c}\chi^{(2)} d\mathscr{E}_\omega^2 \sin 3\theta, \tag{3.1}$$

where $n_{2\omega}$ is the index of refraction at SH and c is the speed of light in a vacuum, and $\mathscr{E}_\omega$ is the electric field amplitude of the pump beam. The $\mathscr{E}_x$ is related to the irradiance by $I_x = n_{2\omega}\varepsilon_0 c\mathscr{E}_x\mathscr{E}_x^*/2$, which can be calculated from the measured quantity, average power, by considering that I_x is Gaussian in both time and space, with widths (full width at half maxima) of τ and W, respectively. By using W = 2 μm, τ = 200 fs, f = 81 MHz, $n_{2\omega} \approx 6.0$,[65] and reflection coefficient of 0.09 from this multilayer structure, we find that the magnitude of $\chi^{(2)}$ for mechanically exfoliated and CVD grown monolayer MoS_2 are about 10^{-7} m/V and 10^{-9} m/V respectively. We attribute the lower $\chi^{(2)}$ in CVD MoS_2 to doping. Unwanted doping during CVD process can generate free carriers, which give rise to the screening effect. However, further investigations are needed to fully understand these results. As $\chi^{(2)}$ belongs to nonlinear process and it depends upon many experimental factors, such as pump pulse, shape and spot size at the sample locations. Hence, the calculated values should be considered as an order-of-magnitude estimate. However, the relative comparison of $\chi^{(2)}$ between mechanically exfoliated and CVD MoS_2 are not influenced by such uncertainties, and are thus accurate.

3.1.8 Summary

In summary, we demonstrate strong second harmonic generation from monolayer and few odd atomic layers of MoS_2 flakes. We show that the second harmonic microscopy has several advantages over linear optical microscopy as well over other nonlinear optical techniques. Our results show that such a nonlinear optical effect can be used to fast and non-invasively characterize atomically thin films of $MoS_2$and other similar materials. Although other nonlinear optical microscopy

such as Raman microscopy has also been used to characterize the number of atomic layers of MoS_2 and other similar materials, the Raman shift often depends on substrates, and the contrast is relatively low. The strong dependence of SH signal on number of atomic layers, with odd number of atomic layers having strong SHG as compared to even number of layers, shows that inversion symmetry is broken in case of odd layers while even layers have inversion symmetry. We also show that the second harmonic microscopy can probe crystal orientation, single-crystal domain size, and layer stacking. Hence, this nonlinear microscopy can be use to improve material properties and has great potential for various optical device applications. It's worth mentioning here that there are three other papers published at the same time on the same topics.[91–93] There is also a recent paper on edge nonlinear optics on a MoS_2 atomic monolayer.[94]

3.2 Third harmonic generation in graphene

3.2.1 Introduction

Graphene, a single layer of carbon atoms arranged into a two-dimensional (2D) honeycomb lattice, has attracted much attention due to its staggering electronic, optical, mechanical, and thermal properties.[8–14] Although, it became readily available just a decade ago,[8] it is an extremely rapidly growing field of material science. It has a linear dispersion relationship between energy, E, and wavenumber, k, $E(k) = \pm\hbar v_F k$, where the Fermi velocity $v_F \approx 10^6$ m/s [see Fig. 3.5(b)].[95–97] Graphene exhibits a number of unusual and remarkable transport properties that make it attractive for nano-electronic applications,[9–11] including high mobilities[8,11–13] and nearly-ballistic transport at room temperature;[12,14] however, it is the optical properties of graphene that are of primary interest here.

Combined with its superior charge transport properties, graphene can be used as transparent conductors[98–101] in photovoltaic devices,[102,103] and touch screens.[99] The broadband absorption and high carrier mobility also make graphene an ideal candidate for broadband and ultrafast photodetectors.[104–110] The strong and broadband interaction of graphene with light can be used in

optical modulators,[111,112] plasmonic devices,[113–118] broadband polarizers,[119] and magneto-optical devices.[120]

For many photonic and optoelectronic applications, nonlinear optical properties are also desired. So far, nonlinear optical properties of graphene have been less explored, and a clear understanding is still yet to establish. On second-order nonlinear optical properties of graphene, theoretical studies have suggested rather large second-order nonlinear susceptibilities,[121,122] especially AB-stacking bilayer graphene.[123]

However, experiments have shown very weak second-harmonic generation from graphene and few-layer graphite, including AB-stacking bilayer graphene, that are even weaker than silicon substrate used to host graphene flakes.[124,125]

Several third-order nonlinear optical effects have been studied in recent experiments. Two-photon absorption was observed in bilayer graphene, indicating the magnitude of a third-order nonlinear susceptivity, $|\chi^{(3)}|$, on the order of 10^{-16} m^2/V^2,[126] which is consistent with their quantum perturbation theory. In the same study, however, two-photon absorption was not observed in monolayer graphene, and the theory predicted that $|\chi^{(3)}| \approx 10^{-18}$ m^2/V^2.[126]

In contrast, however, ballistic photocurrents have been injected into multilayer epitaxial graphene samples by quantum interference between two-photon absorption and one-photon absorption, which suggests that the strength of the two-photon absorption is significant in graphene.[127] Moreover, $|\chi^{(3)}|$'s as large as 10^{-15} m^2/V^2 have been reported for coherent four-wave mixing experiments in graphene.[128]

3.2.2 Experimental conditions

We fabricated graphene and few-layer graphite samples on a silicon substrate with a 300-nm silicon dioxide layer by mechanically exfoliating graphite flakes with adhesive tapes. Thicknesses of the studied flakes are determined by their optical contrasts, Raman spectroscopy, and atomic force microscopy.

The experimental setup to observed THG is shown in Fig. 3.5(a). We focus a near-infrared

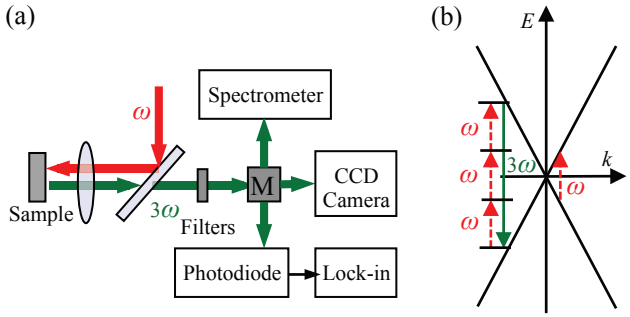

Figure 3.5: (a) Experimental schematic: A fundamental (ω, red) pulse is normally incident on the sample. The third harmonic (3ω, green) is detected in the reflected direction by a CCD camera, a spectrometer or a photodiode connected to a lock-in amplifier. (b) Schematic diagram showing the linear dispersion of graphene, indicating the one-photon absorptions of ω and 3ω and illustrating the energy level description of third harmonic generation. Data from Kumar *et al.*[2]

laser pulse (ω, red) to the sample by a microscope objective lens. The pulses, with an average power in the range of 1-10 mW, are obtained from an optical parametric oscillator pumped by a Ti:sapphire laser with a repetition rate of 81 MHz. Its third harmonic (TH, 3ω, green) generated on the sample is collected by the same lens. A set of color filters is used to block the ω beam and a set of flip mirrors (M) is used to direct the 3ω beam to an imaging charge coupled device (CCD) camera, a spectrometer, or an a silicon photodiode connected to a lock-in amplifier.

The CCD camera is used to rapidly locate a flake having the desired thickness and to spatially image the 3ω spot. The spectrometer, equipped with a thermoelectric cooled silicon CCD camera, allows us to detect weak 3ω signals and to accurately determine it wavelength. The combination of the photodiode, which has an internal amplifier, and the lock-in amplifier provides for the continuous monitoring of the 3ω power as experimental parameters are varied.

3.2.3 Experimental results

The 3ω signal produced by a graphene flake when it is irradiated by an ω beam with horizontal linear polarization is summarized in Fig. 3.6. The spectrum of the emitted 3ω light produced by an ω beam with an average power of 10 mW is shown in the inset of Fig. 3.6. The central wavelength of 575.5 nm is within 0.4% of the separately measured ω wavelength (1720.4 nm) divided by 3

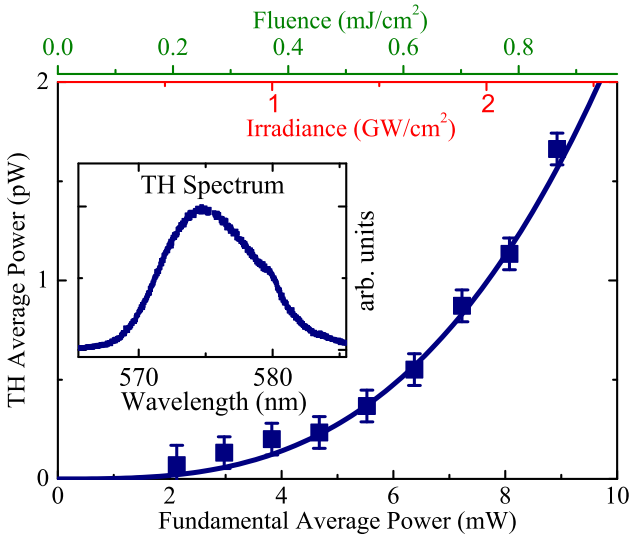

Figure 3.6: The average power of the third harmonic as a function of the average power of the incident fundamental (solid squares), and the spectrum of the third harmonic (solid squares, inset). The solid line is a cubic fit ($\chi^{(3)} = 0.4 \times 10^{-16}$ m^2/V^2) of Eq. (1) to the data using parameters appropriate for our experimental conditions, as discussed in the text. Data from Kumar *et al.*[2]

(*i.e.*, 573.5 nm), which confirms that we are measuring the third harmonic [see Fig. 3.5(b) for the energy diagram of THG]. When the laser spot is moved from the flake to the bare substrate, no 3ω signal is observed under the same conditions. We also note that no second harmonic signal was observed under the same conditions, neither from the graphene flakes nor from the Si/SiO_2 substrate.

Hence, the THG in graphene is much stronger than the second-order responses of both graphene and the substrate. In addition, by using a polarizer in front of the spectrometer as a polarization analyzer, we found that the 3ω pulse is linearly polarized along the same direction as the ω pulse.

We repeat the measurement with different powers of the ω beam. The results are plotted as squares in the main panel of Fig. 3.6. The CCD counts are converted to the actually average power by measuring spectrum of a laser pulse of 560 nm with a known power that incidents to the substrate. Hence, we have included the reflection of the substrate, the loss of all optics, and the sensitivity of the spectrometer. For convenience, the corresponding ω peak on-axis irradiance and pulse fluence are also shown on the top axis. The solid line in the main panel of Fig. 3.6 indicates a cubic dependence. Clearly, the measured TH power is consistent with a cubic dependence, which

is another signature of THG. The small deviation under low power levels could be attributed to some backgrounds in spectra.

3.2.4 Estimation of third order susceptibility

To deduce the magnitude of $\chi^{(3)}$ from our data, we model the THG process with coupled-wave equations,[15] which are greatly simplified owing to the small thickness and almost-constant index of refraction of graphene. The amplitude of the TH field can be written as ,

$$\mathscr{E}_{3\omega} = \frac{1}{4}\frac{i3\omega}{2n_{3\omega}c} d\chi^{(3)}\mathscr{E}_{\omega}^{3}, \tag{3.2}$$

where c is the speed of light in a vacuum, d is the sample thickness, $n_{3\omega}$ is the index of refraction of the material at 3ω, and $\mathscr{E}_{3\omega}$ ($\mathscr{E}_{\omega}$) is the magnitude of the 3ω (ω) field and where each field is related to its irradiance by $I_i = n_i\varepsilon_0 c\mathscr{E}_i\mathscr{E}_i^*/2$. Furthermore, if the irradiance associated with each fundamental pulse is taken to be Gaussian in space and time,

$$I_{\omega}(r,t) = I_0 e^{-4\ln 2(r/W)^2} e^{-4\ln 2(t/\tau)^2}, \tag{3.3}$$

with a diameter W and a pulse width τ (both in full width at half maxima), the peak on-axis irradiance, I_0, is related to the average power, $\bar{P_{\omega}}$, by

$$\bar{P_{\omega}} = f\frac{\sqrt{\pi}\tau}{\sqrt{4\ln 2}}\frac{\pi W^2}{4\ln 2} I_0, \tag{3.4}$$

where f is the repetition rate of the laser. While the use of bulk concepts, such as susceptibilities and indices of refraction, to describe a single atomic layer is questionable, this procedure allows us to assign an effective material parameter that allows comparison of THG in graphene to that in other well-known bulk materials. Using values appropriate to our experiment [i.e., d = 0.33 nm, $n_{\omega} \approx n_{3\omega}$ = 2.4, W = 3.5 μm, τ = 320 fs, λ =1720.4 nm, and f = 81 MHz], these expressions are used to extract a value of $|\chi^{(3)}| \sim 0.4 \times 10^{-16}$ m^2/V^2 from Fig. 3.6.

We note that the error bars shown in Fig. 3.6 reflect the day-to-day accuracy in measuring the average power; however, other uncertainties limit the extraction of an accurate value for $\chi^{(3)}$ from the data. For example, the pulse width, τ, the diameter of the spatial profile, W, (which enters squared) and the repetition rate, f, for the laser are used to calculate the peak on axis irradiance I_0 from the measured average power P_ω. Therefore, since I_0 enters cubed in the extraction of $\chi^{(3)}$, any errors in the measurement of τ, W and f are greatly multiplied. Also, the sample used for these measurements is shaped like a rectangle with a width ~ 1 μm and a length much larger than the focused laser spot diameter. Thus, the overlap between fundamental focused laser spot and the sample is imperfect. The fit shown in Fig. 3.6 is numerically corrected for this incomplete overlap. The fit shown in Fig. 3.6 is not corrected for multiple reflections associated with the layered oxide-Si structure. A calculation based on light propagation through our specific layered structure,[125,129] which incorporates third harmonic polarizations, indicates that the $\chi^{(3)}$ value extracted in this case is changed only by roughly a factor of two, which is within the experimental uncertainty discussed above, and for pedagogical simplification, we ignore those complications here. For these reasons, the absolute value of $\chi^{(3)}$ given in the previous paragraph should be taken as an order of magnitude determination. The upper limit on the fluence (and irradiance) shown in Fig. 3.6 is determined by damage to the sample.

3.2.5 Graphene thickness dependence THG

We also carried out few measurements to investigate the nonlinear response from monolayer graphene to multilayer graphite. To investigate graphene thickness dependence, we measured third harmonic signal from flakes of thicknesses ranging from 1 to 6 atomic layers mounted on a single Si/SiO_2 substrate for an average power of 1 mW, as shown in Fig. 3.8. The solid curve in Fig. 3.8 is a fit of Eq. 1, which assumes that $\chi^{(3)}$ is independent of layer number, to the data for an effective third-order susceptibility of $|\chi^{(3)}| \sim 0.8 \times 10^{-16}$ m^2/V^2. We see that this value is $\sim$ twice larger than that extracted from Fig. 3.6. We attribute this variation to uncontrolled uncertainties in the experiments.

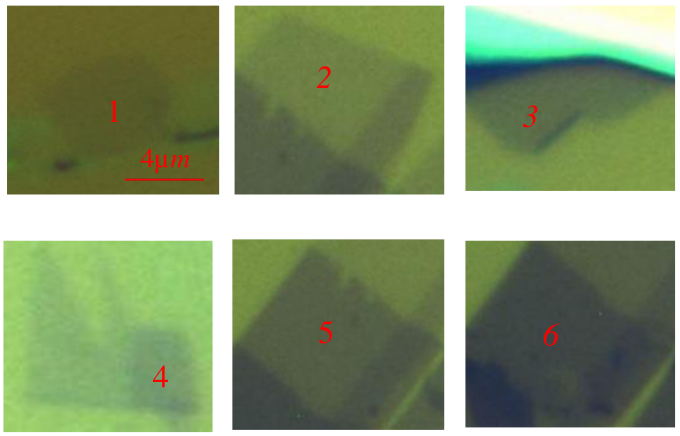

Figure 3.7: Microscope image of a mechanically exfoliated graphene. By measuring the optical contrast relative to the substrate, the number of graphene layers are determined as 1L for monolayer, 2L for bilayer, 3L for trilayer and so on upto six layer of graphene.

Although, we use the same experimental conditions for both measurements. However, measurements were performed on different days, on different flakes and of different size flakes on different substrates. For these reasons, $|\chi^{(3)}| \sim 10^{-16}$ m^2/V^2 should be regarded as an order of magnitude estimate of the susceptibility. This magnitude is one order of magnitude smaller than those estimated from recent four-wave mixing[128] and self-phase modulation[130] experiments, but more than two orders of magnitude larger than that from two-photon absorption experiment and quantum perturbation calculation.[126] Further efforts, from both theoretical and experimental sides, are needed to fully understand third order response of graphene. We also note that the uncertainties are relatively large in this set of measurement, mainly due to necessary adjustments of the alignment when changing flakes and samples. Hence, although Eq. 1 appears to be consistent with the data, we do not view this as a proof of the quadratic dependence.

3.2.6 THG in graphene on glass substrate

To investigate how the nonlinear response of graphene behaves with the transmission geometry, we measure the THG in graphene flake, made by mechanical exfoliation method on the BK7 glass substrate. The lower inset of Fig. 3.9 shows a microscope image of a seven layer graphene flake on a BK7 glass substrate fabricated by mechanical exfoliation using scotch tape. The TH signal

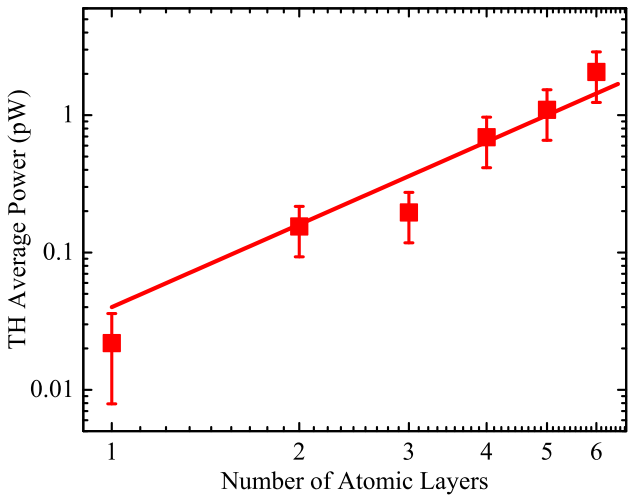

Figure 3.8: The average power of the third harmonic as a function of the number of atomic layers for an average fundamental power of 1 mW (solid squares). The solid line is a quadratic fit ($\chi^{(3)} = 0.8 \times 10^{-16}$ m^2/V^2) of Eq. (1) to the data using parameters appropriate for our experimental conditions, as discussed in the text. Data from Kumar *et al.*[2]

produced by this flake when it is irradiated by a horizontal linearly polarized fundamental beam is summarized in Fig. 3.9. The upper inset of Fig. 3.9 shows the spectra of the TH. From the strength og the TH, we deduced $\chi^{(3)}$ on the order of 10^{-17} m^2/V^2, which is comparable to graphene flake on silicon substrate. Hence, we see that the substrate and the transmission do not affect the $\chi^{(3)}$.

3.2.7 Summary

In summary we have measured the TH emission from graphene and few-layer graphite samples. For a few layers, the emission scales with the cube of the intensity and the square of the number of atomic layers, and it is characterized by an effective third-order susceptibility of the order of $\chi^{(3)}(3\omega;\omega,\omega,\omega) \sim 10^{-16}$ m^2/V^2. This value is larger than that for transparent materials because of the resonant nature of the intermediate and final transitions needed for the TH generation, but it is comparable to the $\chi^{(3)}$'s that are associated with resonant transitions in other materials.[15]

The presence of resonant transitions at ω and 3ω not only enhance $\chi^{(3)}$, but they ensure strong linear (and nonlinear) absorption at both frequencies. This absorption is a detriment to the third-order process, because it reduces the fundamental intensity needed for TH generation and leads to

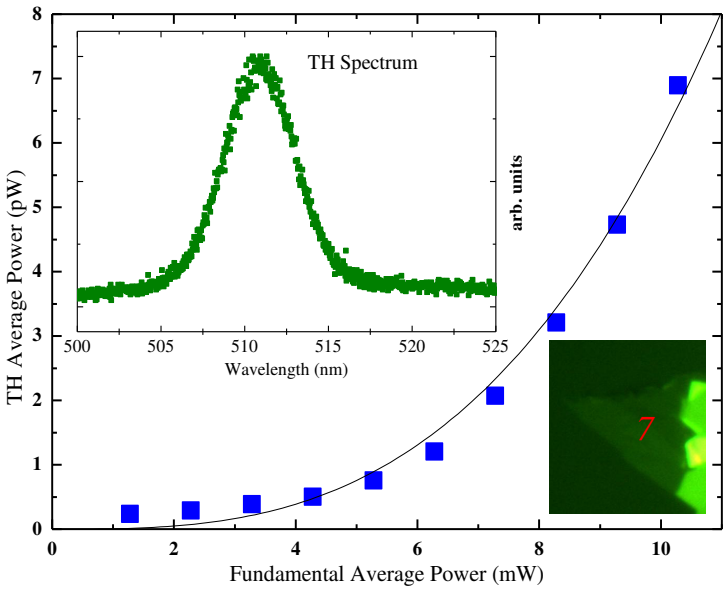

Figure 3.9: (a) The average power of the TH as a function of the average power of the fundamental(solid squares), the spectrum of the TH(solid squares,upper inset), and the microscope image(lower inset) of a seven layer mechanically exfoliated graphene flake on a BK7 glass substrate.

the subsequent absorption of the TH.[131] In fact, one can define a figure of merit (FOM) for the TH process as the ratio of the total number of TH photons generated to the total number of photons (ω and 3ω) absorbed.

It is straight forward to show that this FOM is, in turn, proportional to the ratio $\chi^{(3)}/\alpha$. Thus, while graphene and thin graphite samples (and indeed all materials with resonant transitions) have large $\chi^{(3)}$'s, they do not have unusually large FOMs. For example, for our experimental conditions, a pulse with a fluence of 100 μJ/cm^2 (peak intensity of $\sim$ 0.3 GW/cm^2) would have a TH conversion efficiency of less than 10^{-10}, but would lose 0.023 of its energy to linear absorption.

Chapter 4

Theory of photoexcited quasiparticles: Phonons and excitons

4.1 Introduction to phonons

Phonons are vibrations of the atoms occurring in a rigid crystal lattice. Like a photon, which is a quanta of light, a phonon is a quantum of lattice vibration of a crystalline material. In other words phonon is a wave running through the crystal lattice. Since phonon represents a wave, it has a wavelength and momentum but not mass. Therefore, it is a quasiparticle with a momentum $\hbar\, q$. As in case of electrons in a band we have electron (E-k) dispersion relation similarly in case of phonons we have phonon (E-q) dispersion relation. Phonon dispersion relation represents the variation of phonon frequency ω w.r.t. wave vector q. Phonons strongly affect many physical properties of solids, relating to electrical and thermal conductivities. Therefore, the study of phonons is an important part of material science. Phonons can be classified in two basic types, depending on the movement of the atoms in the crystal lattice.

4.1.1 Optical phonons

Optical phonons are associated with the out-of-phase movement of the atoms in the crystal lattice. Optical phonons can be infrared and/or Raman active depending upon the spectroscopic selection rules. For infrared active phonons the selection rule is that only transitions that cause a change in dipole moment can be observed. Hence, these transitions are generally possible in ionic crystals. The electromagnetic radiation displaces the positive and negative ions of the crystal along opposite directions and hence generates a dipole moment. On the other hand the vibration modes which indirectly interact with radiation through inelastic scattering are called Raman active. Inelastic scattering from phonons is further divided into Raman and Brillouin scattering.

Another selection rule for determining whether a particular optical phonon is Raman active or IR active is based on crystal symmetry. If a crystal possesses inversion symmetry, depending upon the parity, a mode can be either IR active or Raman active. This rule is called *the rule of mutual exclusion*. On the other hand in non-centrosymmetric crystals, modes can be both IR and Raman active. Depending upon whether the displacements are parallel or perpendicular to the direction of wave vector, the optical phonons can be considered as longitudinal (LO) or transverse (TO).

4.1.2 Acoustic phonons

These types of lattice vibrations represent in-phase movements of atoms out of their equilibrium position in crystal lattice. Acoustic phonons modes are somewhat similar to sound waves or water waves depending upon whether the displacement is in the direction of the propagation or perpendicular to the direction of propagation. As with optical phonons, acoustic phonons can also be characterized as longitudinal acoustic or transverse acoustic according to the direction of displacement of the atoms.

Figure 4.1 shows dispersion curves for the optical and acoustic phonons in a typical crystal. The angular frequency of the optical and acoustic phonons is plotted with the wave vector in the first Brillouin zone. The acoustic branch starts at ω, $q = 0$ and then frequency increases in a linear fashion with wave vector q. On the other hand the optical branch is almost flat for small q (large

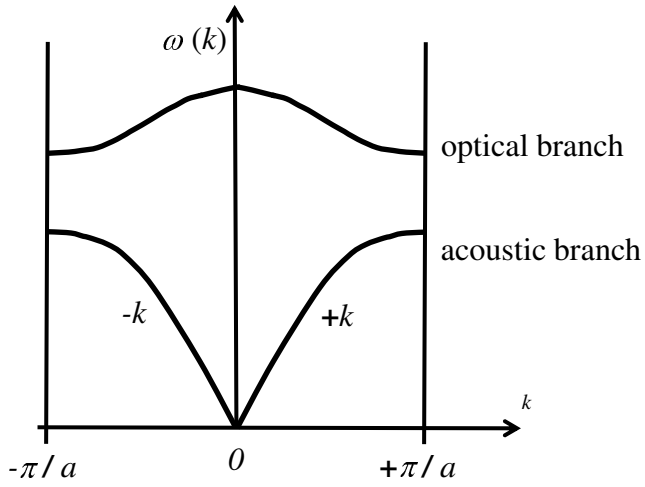

Figure 4.1: Dispersion curves for the optical and acoustic phonon branches in a simple crystal. Figure from Fox.[3]

wavelength) values.

4.1.3 Coherent phonons

Coherent phonons are same kinds of phonons discussed in the last section but with many phonons in one mode with constant phase relation.The coherent lattice vibrations come into play when a high-intensity ultrafast laser pulse shorter than the inverse of a fundamental lattice vibration frequency interact with the crystal. With the advancement of ultrafast lasers, the generation and detection of coherent phonons in different materials has received considerable attention in recent years. The spectroscopic study of coherent phonons is known as coherent phonon spectroscopy. The coherent phonon spectroscopy techniques use a transient absorption microscopy in which an oscillating differential reflection signal vibrating at phonon frequencies is observed by using two ultrafast laser pulses, a pump and a probe, as a function of time delay between the pulses.

4.2 Introduction to excitons

If a photon has energy greater than bandgap of the materials, it can be absorbed by an electron. The absorption of a photon by an electron in the valence band results in a transition, between an allowed energy level, of an electron from the valence band to the conduction band. This transition generates a hole, an empty positively charged state, in the valence band and an electron in the conduction band.

Efficiency of this transition is larger in direct-gap materials as compared to indirect-gap materials. This is due to the fact that the absorbed photon has less momentum as compared to electron momentum. This is because the wave number of the photon is k= p/$\hbar$, where $\hbar$ = h/2π is the reduced Planck constant, and p = h/λ is the linear momentum of the particle. Therefore, photons with wavelength in optical range (400 to 800nm) have k values in the range from 1.57×10^7 to 0.7×10^7 m^{-1}. On the other hand electron wave number corresponds to π/a, where a is the real lattice vector. From here we see that the photon wave vector is negligible as compared to the electron wave vector and it does not change electron momentum but energy.

In other words excited electron remains in same position in k space. Since, in direct band gap materials, the bottom of the conduction band and the top of the valence band occur at the same momentum, the electron transition is more efficient in direct band gap materials. These generated oppositely charged particles, an electron in the conduction band and a hole in the valence band, can attract each other with The Coulomb interaction. Due to their mutual interaction, a bound electron-hole pair can be formed. This bound pair interacting via the Coulomb interaction is called an exciton.

In other words, an exciton is a bound state of an electron and a hole through Coulomb attraction that can move throughout the lattice and can transport energy. An exciton is consider as an electrically neutral quasiparticle, with lower energy than the unbound electron and hole, and hence cannot transport charge. Since an exciton is a bound electron-hole pair, which can move through the material as a bound pair. Therefore, the necessary condition for a stable exciton to form is the same group velocities of electron and hole. A spatially localized electron is like a wave packet

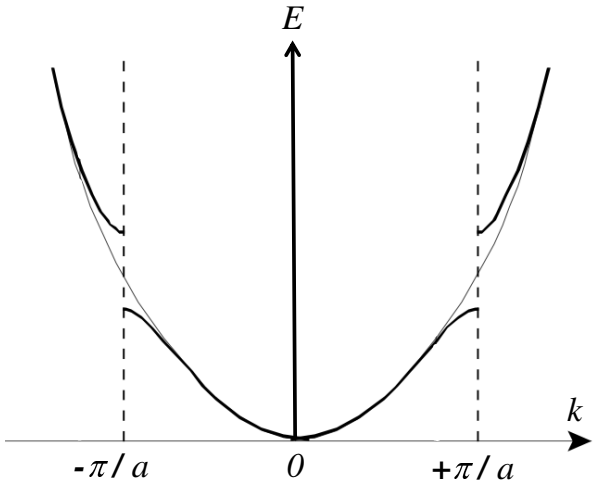

Figure 4.2: The *E-K* dispersion curve of a simple cubic cystal. Figure from Fox.[3]

with a group velocity given by,[3]

$$v_g = \frac{1}{\hbar}\frac{\partial E}{\partial k}, \tag{4.1}$$

where $\partial E/\partial k$ is the gradient of *E-k* dispersion curve shown in Fig. 4.2.

For the same group velocities of electron and hole the above gradient must be the same. We see that this condition satisfied at the zone center. Therefore, exciton formation has a higher probability during a direct transition.

There are two spatial types of excitons, as shown in Fig. 4.3: (a) Wannier-Mott or free excitons, and (b) Frenkel or tightly bound excitons. The basic difference between two types of excitons is the separation between the electron and hole. In case of Wannier-Mott excitons, the mean separation of the electron and hole is much greater than the lattice parameter and hence, are weakly bound to each other.

On the other hand Frenkel excitons are tightly bound excitons in which the mean separation of the electron and hole is smaller as compared to Wannier-Mott excitons. Frenkel excitons have a correlation radius to within a single lattice constant. Excitons are stable for a short period of time. De-excitation of electron to the valence band, results in an effective annihilation of the exciton particle with a simultaneous emission of a photon. In thin films of transition metal dichalcogenides, excitons play important role and have large exciton binding energies. Because of the unusually

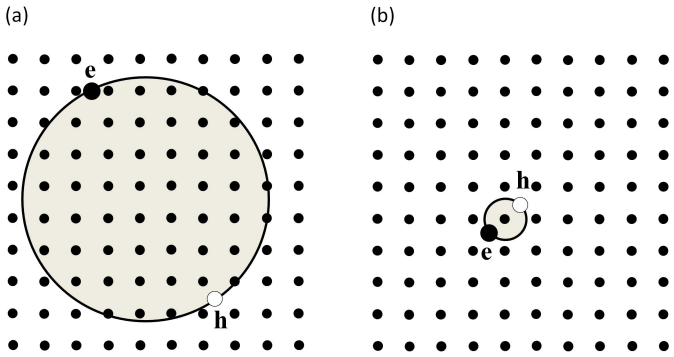

Figure 4.3: Schematic diagram of : (a) Wannier-Mott excitons, and (b) Frenkel excitons. Figure from Fox.[3]

large exciton binding energies in these 2D crystals, their optical properties are dominated by excitons even at room temperature. In particular, real-space transport and recombination of excitons play important roles in optoelectronic applications.

In the following chapters, a detailed study of excitonic dynamics in MoS_2 and $MoSe_2$ by using femtosecond transient absorption spectroscopy will be discussed. The high spatiotemporal resolution allows us to directly measure the exciton diffusion coefficient, exciton lifetime and exciton-exciton annihilation in these transition metal dichalcogenides.

Chapter 5

Experimental techniques: Time-resolved optical spectroscopy

5.1 Introduction

In semiconductors, most of the processes related to subatomic particles are short-lived and extremely fast. In this context the extremely fast means occurring less than few picoseconds. In order to investigate short-lived and fast phenomena, high time resolution is essential. In this dissertation various nonlinear ultrafast processes are discussed with results presented on 2D materials such as MoS_2, $MoSe_2$, Bi_2Se_3 and graphene.

In addition to linear optical spectroscopy which can provide valuable information regarding the various characteristics of electrons, phonons, plasmons, defects etc. in semiconductors, non-linear optical spectroscopy is also very useful to study non-linear characteristics, non-equilibrium phenomenon or transport properties in different materials. Time-resolved optical spectroscopy encompasses a set of techniques for investigating the electronic and structural properties of extremely fast and short-lived excited states. Next section is dedicated to a brief description of the pump-probe technique, one of the powerful techniques of transient spectroscopy.

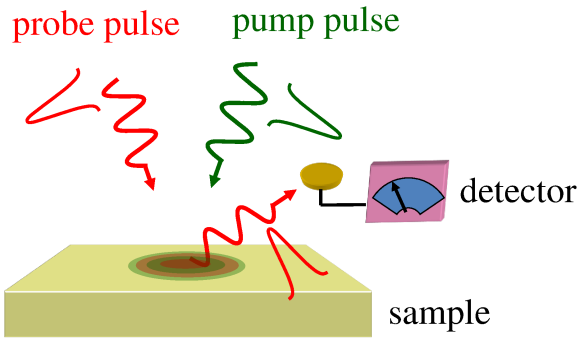

Figure 5.1: Schematic diagram of the pump-probe geometry.

5.2 Differential reflection pump-probe spectroscopy

In the pump-probe technique, two or more ultrashort laser pulses are involved to investigate photoexcited particle dynamics in a chosen sample. A stronger pulse (pump) is used to excite the sample and the photoexcited particle dynamics is monitored by measuring the absorbance of a weaker pulse (probe), as a function of the time delay between the pump and the probe pulses. The Schematics of the pump-probe technique is shown in Fig. 5.1

In this technique the time resolution is dependent upon the precision of the time delay variation and the convolution of pump and probe pulses. For the work presented in this dissertation, the method of choice is based on differential reflection pump-probe spectroscopy.

5.3 Origin of the differential reflection signals

As mentioned earlier, in the usual transient absorption microscopy by using femtosecond pump-probe techniques we can study various ultrafast processes, which can provide valuable atomic scale information, of a given material. In transient absorption microscopy the pump pulse creates a nonequilibrium distribution of photoexcited particles. By measuring the probe reflection as a function of delay time with respect to the pump pulse, we can directly study the ultrafast photoexcited particles dynamics of these nonequilibrium photoexcited particles back to equilibrium.

Generally, a differential reflection signal can be induced by the lattice excitations (phonons) and/or electronic excitations (carriers). Carriers can change the reflection via two major mechanisms. First, free carriers can absorb photons, causing an increase in absorption and therefore a decrease in reflection.

Normally, in the experiments the sign of the differential reflection is positive. That is, the reflection is increased by the presence of the pump pulse. This is inconsistent with the free-carrier absorption. The second mechanism of carrier-induced differential reflection is the effect of phase-space filling. The carriers occupy energy states in the conduction band, reducing absorption. This mechanism gives a positive differential reflection and can be rather strong if the probe photon energy matches the energy states occupied by the carriers. For many materials, in addition to the differential reflection caused by hot carriers we also see oscillating signals superimposed on the carrier dynamics signal. These oscillations in the differential reflection signal usually correspond to the vibration frequencies of the respective material. The lattice excitation can induce oscillatory differential reflection signals via three mechanisms: interference of the probe reflections by the surface and by the strain wave, multiple reflections of the strain wave, and coherent lattice vibration. Raw differential reflection signal has more contribution from carriers, so to quantitatively analyze the oscillations, one subtracts off the background signal and use Fourier filter with a proper cutoff frequency to filter out unwanted signal.

5.4 Differential reflection to probe photoexcited particle dynamics

In this section, we discuss in detail how to monitor the photoexcited particle dynamics with the probe pulse. For the normal incident probe pulse, the linear reflection coefficient of the unexcited sample can be obtained from Snell's law,

$$R_0 = \frac{(n_0-1)^2+\kappa_0^2}{(n_0+1)^2+\kappa_0^2}, \tag{5.1}$$

where n_0 and κ_0 are the real and imaginary parts of the index of refraction. The latter, known as the extinction coefficient, is related to the absorption coefficient (α_0) and light wavelength (λ) by $\kappa_0 = (\lambda/4\pi)\alpha_0$. The photoexcited particles injected by the pump pulse can change the reflection coefficient to

$$R = \frac{(n-1)^2+\kappa^2}{(n+1)^2+\kappa^2} \equiv R_0 + \Delta R. \tag{5.2}$$

In our measurements the probe pulse is tuned to an excitonic resonance, so the absorption is expected to play a dominant role. Hence, we assume real part is unchanged, $n = n_0$, and $\kappa = \kappa_0 + \Delta\kappa$. Furthermore, if $\Delta\kappa$ only causes a small relative change of R, i.e. $\Delta R \ll R_0$, we have

$$\Delta R = -\frac{8n_0\kappa_0}{[(n_0+1)^2+\kappa_0^2]^2}\Delta\kappa. \tag{5.3}$$

Normally, we get $\Delta R/R_0$ on the order of 10^{-3}. Hence, this condition is safely satisfied, and the differential reflection

$$\frac{\Delta R}{R_0} = -\frac{8n_0\kappa_0}{[(n_0+1)^2+\kappa_0^2][(n_0-1)^2+\kappa_0^2]}\Delta\kappa. \tag{5.4}$$

In our scheme, we probe the injected photoexcited particles by saturation of excitonic absorption induced by these particles. In most cases, excitonic nonlinearities, such as absorption saturation, are induced by real exciton populations via phase-space state filling. However, it has been established that excitonic transition strength can be changed by the phase-space state filling effect of free carriers, since the exciton wave function is composed of free-carrier states.[132] Although this effects is generally weaker than those caused by exciton population, it is less selective to photoexcited particle energy distribution. Hence, it can effectively probe photoexcited particles with a high kinetic energy. Recently, we have shown that free carrier induced excitonic nonlinearity can be used to probe ballistic transport of hot carriers[133–138] and coherent plasma oscillation[139] in GaAs. In this effect, the change in extinction coefficient can be described by

$$\Delta\kappa = -\sigma\kappa_0\frac{N}{N+N_s}, \tag{5.5}$$

where N is the photoexcited particle density, N_s is the saturation density and the cross section σ is introduced to describe the effectiveness of photoexcited particles in saturating the probe transitions. Therefore, the differential reflection is related to the photoexcited particle density by

$$\frac{\Delta R}{R_0} = \frac{8n_0\kappa_0^2}{[(n_0+1)^2+\kappa_0^2][(n_0-1)^2+\kappa_0^2]}\sigma\frac{N}{N+N_s}. \tag{5.6}$$

In the experiments, photoexcited particles are injected by interband absorption of the pump pulse. The on-axis peak energy fluence of the pump pulse, F_0, is related to its time average power, P, by

$$F_0 = \frac{4\ln(2)P}{\pi f w^2}, \tag{5.7}$$

where f is the repetition rate of the laser and w is the full width at half maximum of the focused pump spot. We assume that with each absorbed pump photon, one electron-hole pair is injected. The on-axis photoexcited particle density excited near the sample surface can then be written as

$$N_0 = \frac{(1-R_0)\alpha_0 F_0}{\hbar\omega}, \tag{5.8}$$

where α_0 and $\hbar\omega$ are the absorption coefficient and energy of the pump photon, respectively. The lateral distribution of photoexcited particles is Gaussian, identical to the intensity profile of pump spot. From this procedure, we can convert the pump power to injected peak photoexcited particle density, by using the complex index of refraction of $5.4+3.1j$.[65]

5.5 Summary

Spectroscopy in general is the study of light matter interactions. It is one of best tools to study various micro and macroscopic processes in wide variety of materials. The time constants for most of the atomic scale processes are of the order of picoseconds down to a few femtoseconds. Therefore, to observe these processes, the detectors need to be faster than this time scale. The invention of ultrafast laser made it possible to investigate ultrafast transient processes of tempo-

ral durations in the picoseconds and femtosecond regime by femtosecond pump probe transient absorption spectroscopy.

In transient absorption microscopy the pump pulse creates a nonequilibrium distribution of photoexcited particles. By measuring the probe reflection as a function of delay time with respect to the pump pulse, we can directly study the ultrafast photoexcited particle dynamics of these nonequilibrium photoexcited particles back to equilibrium. Generally, a differential reflection signal can be induced by the lattice excitations (phonons) and/or electronic excitations (carriers).

Chapter 6

Results and analysis: Photoexcited quasiparticle dynamics in 2D materials

6.1 Topological insulator Bi_2Se_3

6.1.1 Introduction

As a new novel insulating state of matter, the topological insulator behaves like a bulk insulator with a large bandgap in its interior, but with a gapless surface that is protected by time-reversal symmetry.[41–44] Two-dimensional topologically protected edge states, or quantum spin Hall effect, was predicted in 2005,[45] and soon thereafter demonstrated in HgTe quantum wells.[46] More recently, three-dimensional bulk topological insulators were also predicted[47,48] and demonstrated in several binary bismuth compounds.[49–51]

Optical techniques are standard tools used to study electronic and lattice properties of solids. Several theoretical works have illustrated interesting interactions between topological insulators and light.[140–143] Experimentally, reflection,[144,145] transmission,[145] Kerr[146] and Faraday rotations,[147] and second-harmonic generation[148] of Bi_2Se_3 have been studied in visible,[148] infrared,[145] and terahertz ranges.[146] Very recently, an ultrafast pump-probe experiment was reported, in which oscillatory differential reflection signals are observed.[149]

Previously, ultrafast pump-probe techniques have been used to study phonon dynamics in many different solids. Generally, phonons are generated by an ultrafast pump pulse via excitation of hot carriers that rapidly relax their energy by phonon emission. These phonons can induce differential reflection or transmission signals that show oscillatory behaviors as a function of the time delay between the probe and the pump pulses. However, the oscillation can be induced by three very different mechanisms: interference between multiple probe reflections, reflections of a strain wave at sample boundaries, and coherent lattice vibrations.

If the sample is transparent at the probe wavelength, the probe pulse penetrates into the sample. If an acoustic wave is generated at the sample surface by the pump pulse and propagates into the sample, the part of the probe that is reflected by the sample surface can interfere with that reflected by the propagating acoustic wave. Hence, the overall reflection coefficient oscillates with the probe delay because the phase of the second reflection depends on the location of the propagating acoustic wave. The oscillation period is proportional to the probe wavelength and is inversely proportional to the index of refraction and the sound speed.[150,151] This technique has been used to study the propagation of acoustic waves in many material systems including As_2Te_3,[150,151] GaAs-based multilayer structures,[152–156] GaN[157] and its heterostructures,[158] SiO_2,[159] sapphire,[160] $NdNiO_3$,[161] and several magnetic materials.[162–165]

For strongly absorptive materials, the probe pulse will mainly sense the regions near the surface. An oscillatory differential reflection signal can still be observed, with two different mechanisms. For thin film or multilayer structures, the acoustic wave generated at the surface propagates into the film. Multiple reflections from the back surface or interfaces gives rise to periodic modulations of the dielectric function near the surface, causing oscillatory differential reflection signals. In this case, the period is proportional to the layer thickness and inversely proportional to the sound speed. It is independent of the probe wavelength. This technique can be used to determine the thickness, the sound speed, and the damping of the acoustic waves in several materials including As_2Te_3,[150,151] gold[166] and its nanostructures,[167] silicon,[168,169] germanium,[168] GaAs/AlGaAs heterostructures,[155] and InAs quantum dots.[170]

In case of bulk materials with strong absorption coherent lattice vibration caused by phonons instantaneously generated at the surface can modulate the bond length, and induce oscillatory differential reflection signals. Such oscillations come directly from lattice vibration, and therefore have a frequency solely determined by the modes of the phonons excited. Coherent phonons in many systems have been studied by this process, including GaAs/AlAs superlattices,[171–175] quantum dots of InAs,[176] PbS,[177] CdTe,[178] GaN[179] and its quantum wells,[180] cuprate thin films,[181] bismuth nanowires,[182] silicon membranes,[183] and germanium.[184]

6.1.2 Experimental technique and procedure

The Bi_2Se_3 single crystals are grown via a modified Bridgman process and slow cooled in a constant temperature gradient of approximately 14 K/cm over three weeks. The carrier density in the bulk, determined from Shubnikov de Haas oscillations, is about 1.2×10^{19} /cm^3. The bulk transport properties are similar to those previously observed in metallic samples with comparable carrier density, i.e., the samples are rather metallic.[185] The sample surface had been exposed to air for about two months before the optical pump-probe measurements were taken. However, the main observations are reproducible on a fresh surface obtained by cleaving the sample with an adhesive tape.

Figure 6.1(a) shows schematically the experimental setup. A titanium sapphire laser (Ti:Sa) provides ultrashort pulses with a central wavelength of 800 nm and a repetition rate of 80 MHz. The majority of the output is used to pump an optical parametric oscillator (OPO) with a signal output of 1480 nm. The second harmonic of this output with a central wavelength of 740 nm is obtained by using a beta barium borate (BBO) crystal. This pump pulse is focused to a Gaussian spot of 2.4 μm full width at half maximum (FWHM) at the sample surface by using a microscope objective lens with a high numerical aperture. A small fraction of the 800-nm output of the Ti:Sa is used as the probe pulse, and is focused to the sample through the same lens to a Gaussian spot of 4.0 μm.

Since the objective lens is made of dispersive materials and is rather thick, the pump and probe

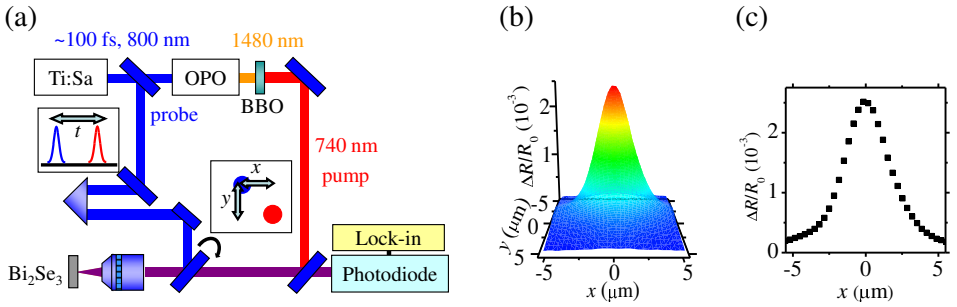

Figure 6.1: Panel (a) shows schematically the experimental system used for the experiment. Panel (b) shows the spatial profiles of the differential reflection signal measured by scanning the probe spot in the $x-y$ plane with a probe delay of 0.4 ps. The peak energy fluence of the pump pulse is 56 μJ/cm^2. Panel (c) shows a cross section on the x axis ($y = 0$). Data from Kumar *et al.*[4]

pulses are expected to be broadened. To determine the actual temporal widths of the pulses, we put a thin GaAs crystal grown along (110) direction at the sample location, and detect the sum-frequency generation of the two pulses as a function of the time delay between the two pulses. The intensity cross-correlation, shown as the gray area in Fig. 6.3(c), has a temporal width of 250 fs. This defines the time resolution of our study. Furthermore, this process allows us to accurately determined the zero probe delay, which is defined as the time when the centers of the probe and the pump pulses overlap.

The reflected probe is collimated by the objective lens, and detected by a photodiode. The differential reflection of the probe, $\Delta R/R_0 = (R - R_0)/R_0$, is defined as the relative change in the reflection (R) caused by the pump pulse. The R_0 is the reflection without the presence of the pump pulse, and is measured to be about 0.50. To measure $\Delta R/R_0$, a mechanical chopper is used to modulate the intensity of the pump pulse with a frequency of several kHz, and a lock-in amplifier slaved to the modulation frequency is used to detect the voltage of the photodiode.

A balanced detection technique is used in order to improve the signal-to-noise ratio.[136] In the balanced detection technique, a portion of the probe beam is taken before entering the sample, and is sent to the other photodiode of the balanced detector as the reference beam. The balanced detector outputs a voltage that is proportional to the difference between optical powers on the two photodiodes.

In the measurements, we first block the pump pulse, and adjust the reference to match the

reflected probe power, such that the balanced detector outputs a zero voltage. We then allow the pump pulse to reach the sample. It injects carriers, which change the reflection coefficient of the sample for the probe pulse. Hence, the balanced detector now outputs a voltage that is proportional to a differential reflection of the probe, $\Delta R/R_0$. The advantage of using the balanced detector is to suppress the intensity noise of the probe pulse. Such a common mode noise is equally distributed on the two photodiodes, and hence is almost cancelled.

To measure the differential reflection as a function of the probe delay, defined as the time delay of the probe pulse with respect to the pump pulse, we change the length of the pump arm by moving the retroreflector in the pump arm. The time resolution in these measurements is about 250 fs, since both pulses are about 180 fs at sample, mainly due to dispersion of the objective lens. The pump and the probe pulses are linearly polarized along perpendicular directions. We have also repeated one measurement with the two pulses polarized along the same direction, and found no difference in the signal. All of the measurements are performed with the sample at room temperature and in the air.

6.1.3 Experimental results

Figure 6.1(b) shows the spatial distribution of the $\Delta R/R_0$ signal measured by scanning the probe spot on the sample surface, along x and y, with a fixed probe delay of 0.4 ps. Here the $x = y = 0$ is defined as where the centers of the pump and the probe spots overlap. The x and y directions are arbitrarily chosen with respect to the crystal orientation, since the sample properties in the $x-y$ plane is expected to be isotropic. The cross section along the x axis is plotted in the Fig. 6.1(c). the average power of the pump beam is 400 μW, corresponding to a peak energy fluence of 56 μJ/cm^2 at the center of the pump spot. Using the reflection coefficient of 0.50 and assuming all of the un-reflected pump photons are absorbed near the surface, a fluence of 1 μJ/cm^2 corresponds to an areal carrier density of 2×10^{12}/cm^2.

For a more quantitative study we took many space scans along x-axis at different probe delays. For the rest of the measurements, due to isotropic nature of the materials and ease of the measure-

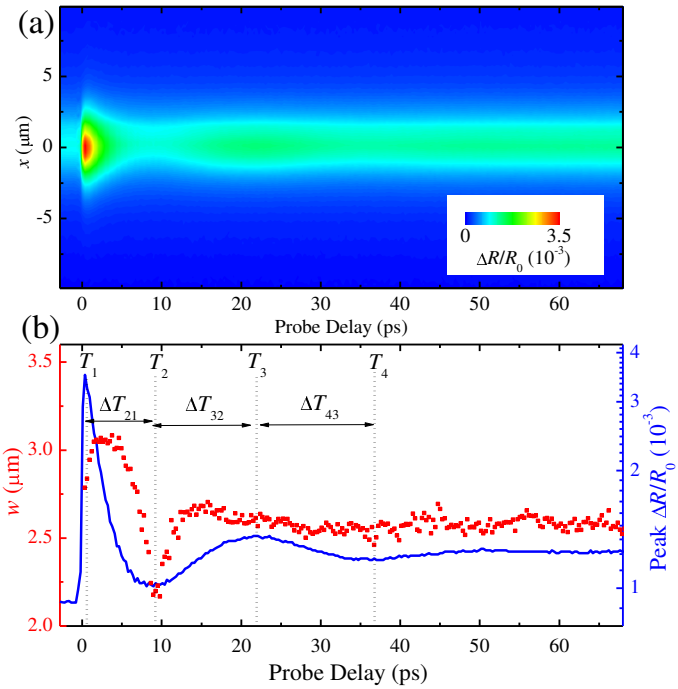

Figure 6.2: Panel (a) shows the differential reflection signal as a function of the probe delay and x, measured with $y = 0$. Panel (b) shows the peak differential reflection signal ($x = y = 0$) as a function of the probe delay (solid line, right axis). The squares (left axis) show the width (FWHM) of the profile as a function of probe delay, obtained through a procedure shown in Fig. 6.3. Data from Kumar *et al.*[4]

ments, we just focused on x-axis for spatial scans. Figure 6.2(a) shows a two dimensional map of $\Delta R/R_0$ with x-axis and probe delay at a fixed $y = 0$. The peak energy fluence of the pump pulse for this measurement is 78 μJ/cm^2.

Figure 6.2(a) shows the variation of the differential reflection signal with time and space. Here time means the delay time between the probe and pump pulse. Spatial variation of the differential reflection signal is obtained by scanning the probe spot on the sample surface with a fixed probe delay. Here the x=y=0 is defined as where the centers of the pump and the probe spots overlap. A cross section of Fig. 6.2(a) with $x = 0$, which represents variation of peak differential reflection signal w.r.t. to probe delay, is shown in Fig. 6.2(b) (right axis). We clearly see an oscillating differential reflection signal.

For more quantitative investigation of these oscillations, we define some characteristic times in Fig. 6.2(b), where T_i is the time for the i-th extreme value, and ΔT_{ji} the time difference between the i-th and j-th extremes. The differential reflection signal reaches a peak at T_1 that is slightly

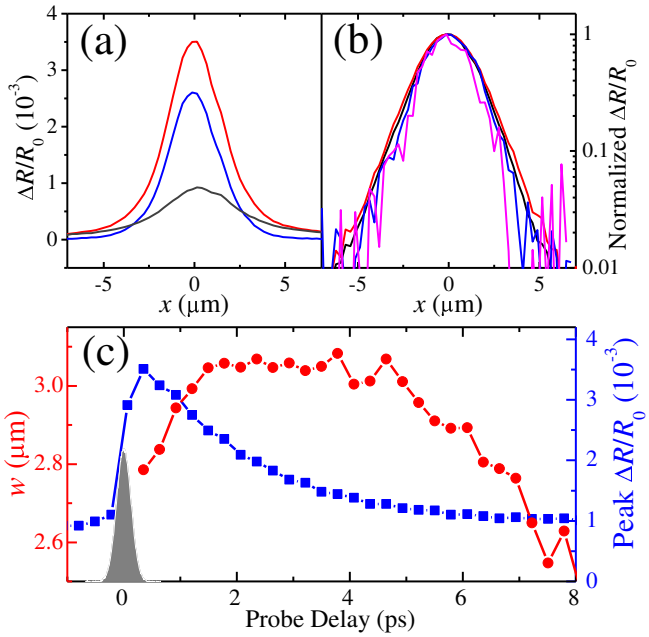

Figure 6.3: Panel (a) shows the spatial profile of differential reflection with a probe delay of 0.35 ps (red/highest) and with negative delays (gray/lowest). The blue/middle curve is the difference. Panel (b) shows the profiles (after removing the background) measured at probe delays of (from wide to thin) 1.78 (red), 0.35 (black), 15.8 (blue), and 10.7 ps (pink), respectively. Panel (c) is the same as Fig. 6.2(b) but with a smaller time range near zero delay. The gray area shows the cross correlation of the pump and the probe pulses. Data from Kumar *et al.*[4]

after zero delay (0.4 ps). After a period of ΔT_{21} = 8 ps, the signal reaches a minimum at T_2. After that, the signal increases for a period of ΔT_{32} = 14 ps followed by another decrease for a period of ΔT_{43} = 15 ps. After T_4 = 37 ps, the signal increases again, until about 50 ps, when the signal reaches a steady level. The time duration of ΔT_{43} = 15 ps corresponds a frequency of 0.033 THz and an energy of 0.14 meV.

Differential reflection signal shown in Fig. 6.2 is composed of DR signal from the present pump pulse plus the previous pump pulse. The signal from the previous pump pulse is called a signal at negative probe delay. Negative signal does not vary with probe delay; it can be easily subtracted from the positive delay DR signal. Figure 6.3(a) represents spatial distribution of $\Delta R/R_0$ along x-axis for negative probe delay (black curve) and positive probe delay (red curve). By subtracting the former curve from the later one we get the differential reflection signal curve (blue curve) associated with the present pump pulse.

In our measurements, the measured spatial profiles are convolutions of actual spatial profile of

DR signal and probe spot. The probe spot has a Gaussian profile with width of about 4 μm. To extract the width of actual spatial profile of DR signal, which has a Lorentz shape, we use a Voigt function in origin software with a fixed Gaussian width of 4 μm. The extracted widths by fitting all the curves with a Voigt function are plotted in Fig. 6.2(b) as the red squares (left axis). With constant shape i.e. Lorentz shape, spatial profiles show pronounced oscillations in the width.

In order to verify that these oscillations are true oscillations of the width and not due to any kind of artifact from fitting process or an experimentation error, and merely reflect the oscillation in height, we have also tried to fit the profiles with Gaussian and Lorentzian functions. Even with the larger mean-square errors, the fits show same oscillations. Hence, the oscillations are true oscillations of profiles width. For further verification, we plot four randomly chosen profiles (normalized) in Fig. 6.3(b). All the four profiles are randomly selected around the probe delay when the width is an extreme. From these four normalized profiles we can easily see that the profile broadens from 0.35 (black) to 1.78 ps (red), and then shrinks at 10.7 ps (pink), and broadens again at 15.8 ps (blue). This broadening trend is consistent with the fit shown in Fig. 6.2(b).

Another evidence that the oscillation in width is not caused by the oscillation in height is that in the first several picoseconds, the width increases while the height drops, as clearly shown in Fig. 6.3(c).

To further investigate the dynamics in Bi_2Se_3 , we did pump fluence dependence of the differential reflection signal and the results are summarized in Fig. 4(a). We note from the curves that the second peak (T_3) shifts systematically with the fluence, showing that the excitation level influences the dynamics.

We plot the characteristic times defined in Fig. 6.2(b) as functions of fluence in Fig. 6.4(b). The T_1 (the rising time) decreases from about 0.8 to 0.3 when the fluence increases from 6 to 100 μJ/cm^2. The interval ΔT_{21} is almost independent of the fluence. However, ΔT_{32} becomes significantly longer (from 8 to 15 ps) when increasing the fluence. Finally, ΔT_{43} is independent of the fluence, and is longer than other intervals. Fig. 6.4(c) shows that the height of the first peak (at time T_1) increases linearly with the fluence.

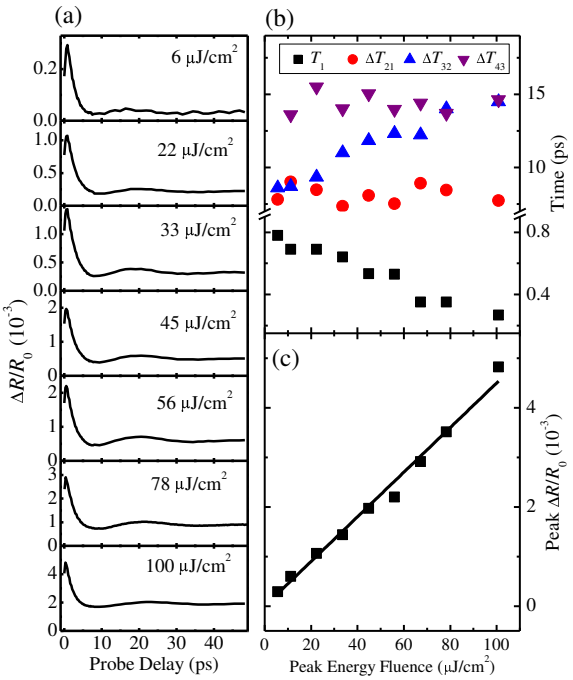

Figure 6.4: Panel (a) shows the peak differential reflection signal ($x = y = 0$) as a function of the probe delay with different pump fluences as indicated in each plot. Panels (b) and (c) summarizes the characteristic times and the peak of the signal as functions of the pump fluence. Data from Kumar *et al*.[4]

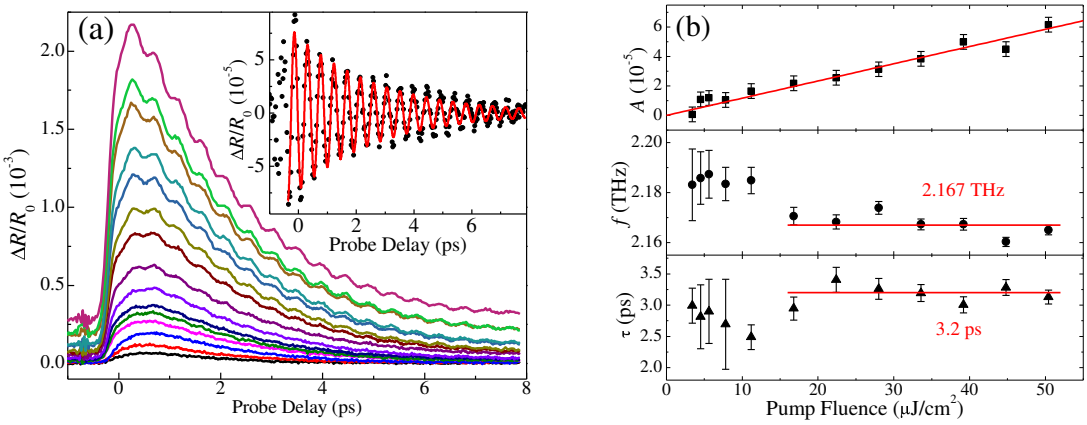

Figure 6.5: Panel (a) shows the peak differential reflection signal ($x = y = 0$) as a function of the probe delay in the first 8 ps, with the pump fluences of (from bottom to top) 0.6, 1.1, 2.2, 3.4, 4.5, 5.6, 7.8, 11.2, 16.8, 22.4, 28, 33.6, 39.2, 44.8, and 50.4 μJ/cm^2. The inset shows the high-frequency oscillation obtained by using a high-pass filter with a cutoff frequency of 2 THz. Panel (b) summarizes the initial amplitude (squares), the frequency (circles), and the decay time (triangles) that are obtained from the fits. Data from Kumar *et al*.[4]

After zooming in first few ps of DR curve, we also see high frequency DR signal in addition to low frequency DR signal. Figure 6.5(a) shows the differential reflection signal as a function of the probe delay for the first 8 ps, with different pump fluences ranging from 0.6 to 50.4 μJ/cm^2 from bottom to top. This fast component of the DR signal is a combination of both low and high frequency osculations.

To explore the high frequency oscillations, we remove the slow varying components from the curves shown in Fig. 6.5(a) by using a high-pass Fourier filter with a cutoff frequency of 2.0 THz. As an example, the points in the inset of Fig. 6.5(a) show the high-frequency component of the top curve with a pump fluence of 50.4 μJ/cm^2. The high-frequency components are fit by using a damped sinusoidal function, $Ae^{-(t-t_0)/\tau}\sin[2\pi f(t-t_1)]$. The result for the pump fluence of 50.4 μJ/cm^2 is plotted as the solid line in the inset of Fig. 6.5(a). Figure 6.5(b) summarizes the initial amplitude (A, squares), the frequency (f, circles), and the decay time (τ, triangles), that are obtained from the fits.

The initial amplitude of the oscillation increases linearly with the pump fluence. The frequency seems to be independent of the fluence. The slight increase (less than 1%) at low fluence could be attributed to the artifact of the Fourier filter when applied to more noisy curves. By averaging the high-fluence data, we deduce a frequency of 2.167 ± 0.002 THz, which corresponds to an energy of 8.974 meV. The decay time deduced from the fits is also independent of the fluence, with an average value of 3.2 ± 0.1 ps.

To explore how pump spot size influence the oscillations, we measure the peak differential reflection signal as a function of the probe delay with two different pump spot sizes of 3 and 11 μm with a fixed peak fluence (17 μJ/cm^2) i.e. the fluence at the center of the spot. As shown by the two curves in Fig. 6.6, similar temporal behaviors ,except slight variation in the background, of the differential reflection are observed. Clearly, the high-frequency oscillations (shown in the inset of Fig. 6.6) are also independent of the spot size.

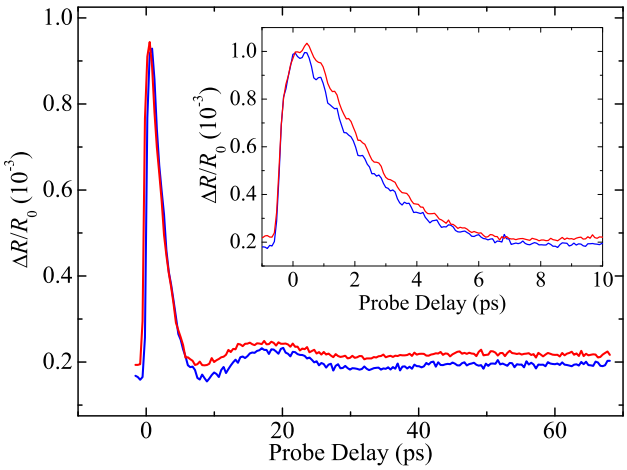

Figure 6.6: The peak differential reflection signal ($x = y = 0$) as a function of the probe delay with different pump spot sizes of 3 μm (blue/lower) and 11 μm (red/upper), respectively. The energy fluence of the pump pulse at the center of the spots is 17 μJ/cm^2 for both measurements. The inset shows the two curves at early probe delays. Data from Kumar *et al.*[4]

6.1.4 Hot carrier dynamics

For the discussion of dynamics related to hot carriers, we will concentrate within few ps of DR signal. As shown in Fig. 6.4, the peak of the differential reflection signal(Fig. 4(c)) increases linearly with the pump fluence and the rise time of peak (squares in Fig. 6.4(c)) decreases systematically with the pump flunece.

Regardless of the dominating mechanism that causes the signal on this time range, the finite rise time is caused by thermalization and energy relaxation of hot carriers. The pump photon energy is 125 meV larger than the probe. If the electrons and the holes are excited with the same excess energy, the pumping states in the conduction band are 62.5 meV higher than the probing states. If the fast component of differential reflection signal is mainly due to the phonons, the rising time reflects the increase of phonon population. Since the phonons are emitted by the hot carriers during their energy relaxation, the rising time measures the time takes for the carriers to reach thermal equilibrium with the lattice.

On the other hand, if the fast component of differential reflection signal is dominated by carriers, the rise of the signal is caused by the movement of carriers from the pumping states to the

probing states by thermalization and energy relaxation. The decay after the peak reflects the movement of the carriers to even lower energy states.

6.1.5 Coherent optical phonons

The coherent relative vibration of atoms in each unit cell causes modulation of the reflection which causes the DR signal in the first few ps to oscillate at High-frequency on the order of 2.167 ± 0.002 THz, shown in Fig. 6.5(a). The oscillation has a frequency of 2.167 ± 0.002 THz [circles in Fig. 6.5(b)], which corresponds to an energy of 8.974 meV. This frequency corresponds to energy of 8.974 meV and has not dependence on the pump fluence. Such a frequency is consistent with the A_{ig}^{I} longitudinal optical phonon frequency determined by Raman spectroscopy (2.16 THz) and the previous pump-probe study (2.13 THz).[149] According to Fig. 6.5(b)(first graph), We see that the initial amplitude of the oscillation is linearly increase with the pump fluence which implies that, the excited optical phonon population is proportional to the pump fluence. The decay time of the oscillation, that is the lifetime of the optical phonons, is 3.2 ± 0.1 ps [triangles in Fig. 6.5(b)], and is also independent of the pump fluence.

Hence, the time-resolved differential reflection study not only provides complementary information on the optical phonon modes in the time domain, but also directly measures the time scale on which the optical phonons decay to acoustic phonons and reveals the coupling strength between different phonon modes.

6.1.6 Coherent acoustic phonons

We attribute the low-frequency oscillation of 0.033 THz to coherent acoustic phonons. The acoustic-mode coherent vibration of the lattice causes modulation of the reflection, with a frequency determined by the phonon energy.[171–184] The frequency corresponds to an energy of 0.14 meV. Unlike in other materials where many periods of oscillation are usually observed,[171–184] only one to two periods are observed here. We see from Fig. 6.2(b) (red squares) that after 40 ps, the spatial profile broadening reaches a quasi-steady value of 2.6 μm. The negative DR signal, caused by previous

pump pulse, has a width of about 4.9 μm. It implies that width again start to broad after 40ps from 2.6 to 4.9 μm. The previous pump pulse arrives at sample about 12.5 ns earlier.

By using the diffusion effect mentioned in the last section, we get a diffusion coefficient of acoustic phonons of 1.2 cm^2/s. This value is consistent, within a factor of four, with the previously reported value of 0.3 cm^2/s of thermal diffusion coefficient in an undoped Bi_2Se_3 sample.[186] The pronounced dip in the width of the profile shown in Fig. 6.2(b) around 8 ps, exactly when the peak differential reflection signal reaches the minimum, and the overall decrease of the width from early delays of several ps (about 3.1 μm) to later delays of about 20 ps (2.6 μm), are not understood. We speculate that it might be related to the decay of optical phonons to acoustic phonons.

6.1.7 Summary

In summary, we have shown that a spatially resolved femtosecond pump-probe technique can be used to study carrier and phonon dynamics in topological insulators. Pronounced oscillations in differential reflection on Bi_2Se_3 were observed with two distinct frequencies. The high-frequency oscillation of 2.167 THz decays in 3.2 ps, and is caused by coherent optical phonons. The frequency is independent of the probe delay, the pump fluence, and the pump spot size. The low-frequency oscillation of 0.033 THz exists for more than 50 ps, and can be attributed to coherent acoustic phonons. We found that the frequency is independent of the spot size. The rising time of the signal shows that the thermalization and energy relaxation of hot carriers are sub-ps in this material, and decrease with the carrier density.

Some of the observed features in this experimental study are not fully understood yet. For example, in the low-frequency oscillation the characteristic time T_{32} increases with carrier density, but not the other two characteristic times; A breathing-like movement of the profile is observed in the first 15 ps, along with an overall decrease of the profile size from several ps to about 15 ps. More experimental and theoretical works are needed to understand these features.

6.2 Transition metal dichalcogenide MoS_2

6.2.1 Introduction

After graphene, MoS_2 is the most extensively studied 2D layered material. Atomically thin MoS_2 has shown several interesting properties related to electronic,[56] optics[53,54] and valleytronics.[35,187] In 2010, two groups independently discovered an indirect-to-direct bandgap transition that occurs when varying the thickness from bulk to monolayer.[53,54]

In 2011, monolayer MoS_2 transistors with a 10^8 on/off ratio and a room-temperature mobility of more than 200 cm^2/Vs have been demonstrated.[56] In 2012, several groups reported observation of valley selective optical excitation and luminescence in monolayer MoS_2.[34,35,187–189] These studies paved ways to apply two dimensional MoS_2 for photonics, electronics, and valleytronics. Studies on *bulk* MoS_2 can provide complementary information for understanding monolayers and their interaction with environments and substrates, since the properties of monolayer MoS_2 are different from, but related to, the bulk. Here in this section we discuss a ultrafast transient absorption microscopy study of exciton dynamics in bulk MoS_2 crystals. By time resolving the dynamics, we observed intervalley transfer, energy relaxation, and recombination of excitons. These results provide fundamental information on exciton dynamics in bulk MoS_2 crystals, and can be used to understand exciton dynamics of MoS_2 bulk and thin atomic layers.

6.2.2 Experimental scheme and expected exciton dynamics

Figure 6.7 shows schematically the transient absorption microscopy setup for bulk MoS_2 . We take a portion of the 780-nm Ti:sapphire output before entering the OPO, and combine it with the idler beam of OPO. By sending both beams to a beta barium borate (BBO) crystal, we generate their sum frequency with a central wavelength of 555-nm. This pulse is focused to the sample surface through a microscope objective lens with a spot size of 1.6 μm (in full width at half maximum). It is used as the pump pulse.

The probe pulse is obtained by second harmonic generation of the 1320 nm signal output of

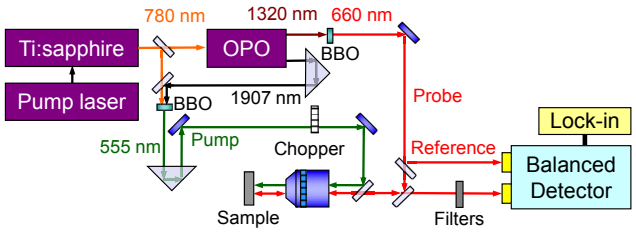

Figure 6.7: Schematics of the transient absorption microscopy system. Data from Kumar *et al.*[5]

OPO in another BBO crystal, with a central wavelength of 660 nm. It is focused to the sample through the same objective lens, with a spot size of 1.3 μm. The reflected probe is collimated by the objective lens, and is sent to one photodiode of a balanced detector. A portion of the probe beam is taken before entering the sample, and is sent to the other photodiode of the balanced detector as the reference beam.

The MoS_2 samples used for this study are natural occurring crystals from SPI Supplies. The background exciton density is below 10^{15} /cm^3. The samples were mounted on glass substrates. The surface of the samples is mechanically cleaved by using an adhesive tape in order to obtain a relative flat, clean, and fresh surface. All the measurements were performed under ambient conditions.

6.2.3 Results and discussion

The black curve in Fig. 6.8(a) (left axis) shows the measured differential reflection signal as a function of the probe delay, with a peak exciton density of 2.1×10^{19} /cm^3. The inset shows the signal near zero probe delay. Clearly, the dynamics has a fast component of less than 1 ps and a slow one persists for several hundred ps. We attribute the slow process to recombination of excitons, *i.e.* exciton lifetime, and the fast process to the dynamical variation of σ associated with evolution of exciton distribution in the conduction and valence bands.

We attribute the initial decay of the signal in the first ps, with a time constant of about 0.35 ps, to this intervalley transfer process. The **Q**-valley electrons still influences the exciton transition, as evidenced by the long-lived signal over 100 ps, but with a smaller cross section. Hence, we

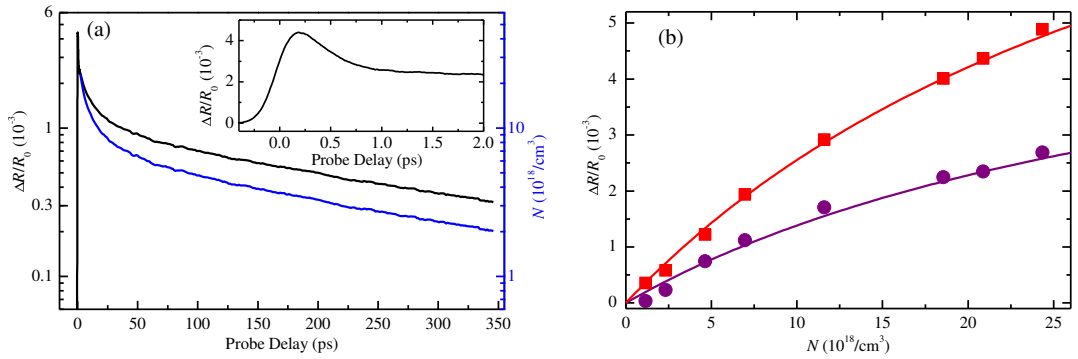

Figure 6.8: (a) Differential reflection as a function of the probe delay (black curve and left axis). The inset shows the signal in early probe delays. The blue curve (right axis) is the exciton density deduced from the measured differential reflection. (b) Differential reflection as a function of injected exciton density for fixed probe delays of 0.2 (squares) and 2.0 ps (circles). The solid lines are calculated from Eq. 5.6 with the same value of $N_s = 3.7 \times 10^{19}$ /cm^3.

attribute the slow dynamics to recombination of excitons in the **Q** valley.

Since the exciton lifetime is on the order of 100 ps, we can assume that exciton density during the first a few ps is a constant, and equal to the injected density. We repeat the measurement shown in the inset of Fig. 6.8 with various pump powers (and hence various injected peak exciton densities). The circles and squares in Fig. 6.8 show the differential reflection signal as a function of the injected exciton density measured at probe delays of 0.2 (the peak) and 2.0 ps, respectively. The dependence is nonlinear, since the injected exciton density is rather high. Both data sets can be fit by using Eq. 5.6, with the same value of N_s.

By fitting many data sets with various probe delays, we deduce a value of $N_s = (3.7 \pm 0.1) \times 10^{19}$ /cm^3, which is used to plot the two solid curves in Fig. 6.8(b). With the known N_s, we can deduce the exciton density as a function of probe delay from the measured differential reflection. The result is plotted as the blue curve in Fig. 6.8(a) (right axis). Hence, although the differential reflection is a nonlinear function of the exciton density, we can reliably deduce the latter from the former.

6.2.4 Summary

We have used a transient absorption microscope to study exciton dynamics in bulk MoS_2 crystals, and reveals several aspects of the exciton dynamics. We find that after the excitons are injected to the more energetic **K** valley, they transfer to the low energy **Q** valley with a time constant of about 0.35 ps. After that, the excitons relax their energy in about 50 ps until they reach thermal equilibrium with the lattice.

6.3 Transition metal dichalcogenide $MoSe_2$

6.3.1 Introduction

As discussed earlier, $MoSe_2$ is an another member of transition metal dichalcogenide's family. In atomically thin 2D TMD structures, the exciton binding energies[21,190–192] are much larger than semiconductor quantum wells - the previously extensively studied quasi-2D systems. Hence, they provide a new platform to study excitons in confined systems. Since the optical properties of these systems are dominated by excitons even at room temperature, for various applications, it is important to understand their excitonic dynamics.

Here we report an ultrafast optical study of the excitonic dynamics in $MoSe_2$ monolayer and bulk samples. So far, most studies on MX_2 have focused on one member of this family, MoS_2. Other members have similar lattice structures as MoS_2, but possess different properties, such as the sizes of the bandgap and the strengths of the spin-orbital coupling.[52] Hence, they can potentially be used to complement MoS_2 in some applications. More importantly, it is possible to use various types of atomic layers as building blocks to assemble multilayer structures and even three-dimensional crystals to achieve desired properties.[27] Therefore, understanding the basic properties of these building blocks is essential.

Recently, strong exciton[25] and trion[191] photoluminescence has been observed in monolayers of $MoSe_2$ in time-integrated measurements. The high temporal and spatial resolution of our tran-

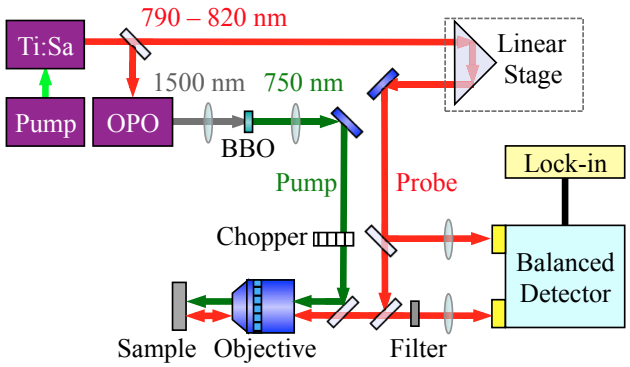

Figure 6.9: Schematics of the transient absorption setup. Data from Kumar *et al.*[6]

sient absorption microscopy measurements allows us to directly study the dynamics of excitons in $MoSe_2$ monolayers. We observe efficient exciton-exciton annihilation at high exciton densities, which reveals the strong interaction between excitons in this strongly confined system. Similar measurements performed on a bulk sample indicate that this process is absent in bulk.

6.3.2 Experimental setup and samples

$MoSe_2$ monolayer samples are fabricated by mechanical exfoliation with an adhesive tape from bulk crystals (2D Semiconductors). By depositing flakes of $MoSe_2$ on silicon substrates with either a 90-nm or a 280-nm SiO_2 layer, we can identify large flakes of $MoSe_2$ monolayers with an optical microscope, by utilizing optical contrasts enhanced by the multilayer substrate.[65] Photoluminescence and Raman spectroscopy are also performed to confirm the thickness of the flakes studied. All the measurements were performed in ambient condition and no signs of sample degradation were observed during the entire study.

The experimental setup to study exciton dynamics in this material is quite similar to the setup described in case of Bi_2Se_3 and MoS_2. The only difference is the choice of pump-probe wavelength combination. The experimental setup for the transient absorption measurements for $MoSe_2$ is shown in Fig. 6.9.

Here Ti:sapphire laser (Ti:Sa) is tuned 790 - 820 nm wavelength range. The majority of the Ti:sapphire laser output is used generate 1500 nm from OPAL. SH of OPAL output from BBO,

which is 750nm, is used as the pump pulse for the measurement. Tuned to the high-energy edge of the A-exciton resonance, the pump pulse injects excitons by resonant excitation. The injected excitons are probed by a 100-fs pulse with a different wavelength in the low-energy side of the resonance. It is obtained directly from the Ti:sapphire laser.

The reflected probe is directed to a photodetector of a balanced detector, whose output is measured by a lock-in amplifier. As discussed in case of Bi_2Se_3 setup, a portion of the probe is taken before entering the objective lens and is sent to the other detector for balanced detection, which improves the signal-to-noise ratio of the system.[133] By using a microscope objective lens, we tightly focus both the pump and the probe pulses to spot sizes of about 1 μm, which is several times smaller than the dimensions of the flakes studied. The pump and the probe spots are overlapped, and are located near the center of the flakes in all the measurements.

6.3.3 Transient absorption to probe excitons

Figure 6.10(a) shows a differential reflection signal of the 810-nm probe pulse as a function of the probe delay. We find that the differential reflection signal decays quickly in the first 50 ps and then slowly over several hundred ps. Since the differential reflection is related to the exciton density, its decay reflects the excitonic dynamics. We note that the peak signal here is below 0.1%. Hence, the pump does not significant change the absorption coefficient of the sample.

In order to establish a precise relation between the differential reflection and the exciton density, we repeat the measurement with different pump fluences. Figure 6.10(b) shows the measured differential reflection near zero probe delay with four different pump fluences. In each case, the rising time of the signal is limited by the instrument response. Hence, the excitons injected by the pump pulse instantaneously change the probe reflection. From the pump fluence, we can estimate the injected exciton density by using an absorption coefficient of 2×10^5/cm[193] and assuming that every pump photon absorbed excites one exciton.

We note that the saturation of the pump absorption can be safely neglected, since the pump only changes the probe absorption by less than 0.1%. Since the exciton lifetime, indicated by the decay

of the signal, is much longer than the rising time, we can ignore the decay of the exciton density during the pump pulse and assume that the exciton density at the peak time equals to the injected density. This procedure allows us to relate the differential reflection signal to the exciton density, as we plot in Fig. 6.10(c). We find that the relation can be accurately described by a saturable absorption model,[15]

$$\frac{\Delta R}{R_0} \propto \frac{N}{N+N_s}, \tag{6.1}$$

where N, and N_s are the exciton density, and the saturation density, respectively. The solid line in Fig. 6.10(c) indicates a fit to the data, with $N_s = (5.8 \pm 0.5) \times 10^{12}/\text{cm}^2$. Such a saturation density corresponds to an average exciton distance of about 4 nm. The exciton Bohr radius, a_B, in monolayer MX_2 have been estimated to be about 1 - 2 nm,[191,194] suggesting a saturation density $(\pi a_B^2)^{-1}$ on the order of $1 \times 10^{13}/\text{cm}^2$. The saturation density deduced here is reasonably consistent with these calculations.

Since the monolayer sample is attached to a multilayer substrate of Si/SiO_2, the reflection of the probe is determined by the complex index of refraction of each layer. Hence, the differential reflection is related to, in a rather complex way, the fractional changes of the absorption coefficient and the real index of refraction of the monolayer $MoSe_2$ induced by the pump. However, when the fractional changes are much smaller than one, the differential reflection is approximately proportional to both fractional changes, as we have shown previously.[195]

To further study the mechanism of the saturable absorption, we repeat the measurement at different probe wavelengths, with a fixed pump wavelength of 750 nm. We observed the same dynamics and the saturation behavior shown in Figs. 6.10(a) - 6.10(c). The peak $\Delta R/R_0$ with a pump fluence of 4 μJ/cm^2 is plotted as the squares in Fig. 6.10(d) (left axis).

Clearly, the spectrum of $\Delta R/R_0$ coincides with the photoluminescence (PL) spectrum [solid line in Fig. 6.10(d)], which is measured with a 633-nm continuous-wave laser excitation. It has been shown that in monolayer $MoSe_2$, the PL spectrum is consistent with the absorption spectrum.[191] Hence, this result indicates that the pump-injected excitons reduce the exciton transition strength. The transient absorption is not dominated by the broadening nor the shifting of the resonance, since

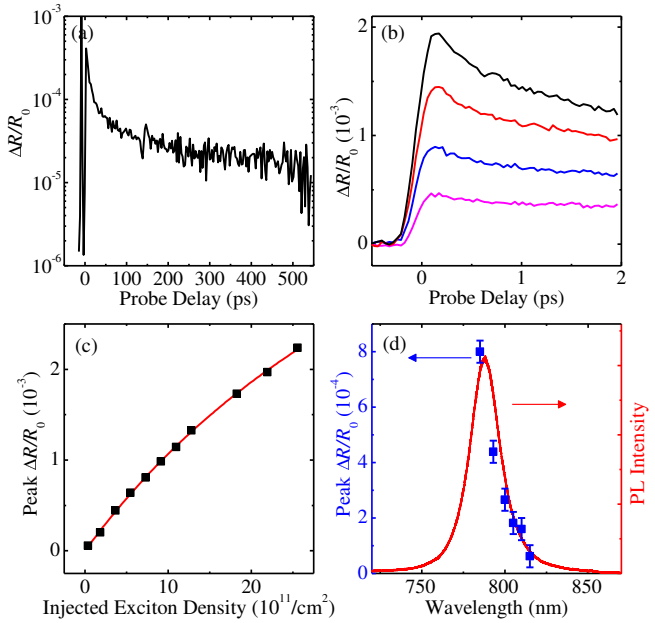

Figure 6.10: (a) Differential reflection of a $MoSe_2$ monolayer measured with a probe wavelength of 810 nm and a pump wavelength of 750 nm. The energy fluence of the pump pulse at the center of the pump spot is 8 μJ/cm^2. (b) Differential reflection single near zero probe delays with pump fluences of (from bottom to top) 10, 20, 40, and 55 μJ/cm^2, respectively. (c) Peak differential reflection signal as a function of the injected exciton density. The solid line is a fit. (d) Peak differential reflection signal as a function of the probe wavelength (squares, left axis). The solid line is a photoluminescence spectrum of sample. Data from Kumar *et al.*[6]

in either case the spectrum would have been significantly different from the PL spectrum.[132]

This is quite different from monolayers of MoS_2, in which previous studies have shown rather complex spectra of transient absorption.[196,197] We note that the probe wavelength range in this measurement is limited by the instruments: Tuning the Ti:Sa to wavelengths shorter than 780 nm would result in inefficient pumping of the OPO and poor signal-to-noise ratio due to the partial overlap of the spectra of the pump and probe pulses.

The observed excitonic absorption saturation and the unusually large exciton binding energy indicate potential applications of $MoSe_2$ monolayers as saturable absorbers for various nonlinear photonic devices.[198] Here, however, our purpose is to use the absorption saturation to study excitonic dynamics. In principle, the solid line in Fig. 6.10(c) allows us to precisely convert the measured $\Delta R/R_0$ to N. In this study, however, most measurements are performed with $N \ll N_s$, so that the $\Delta R/R_0$ is approximately proportional to N.

6.3.4 Exciton-exciton annihilation

We study exciton dynamics at different injection levels. The left column of Fig. 6.11 shows that the decay of the exciton density depends strongly on the initially injected density. When increasing the injected density, a fast decay component develops. Such a density-dependent decay is not expected from a non-interacting exciton system, thus indicating strong exciton-exciton interactions.

It is well known that in strongly confined systems, such as organic crystals, excitation of nearby molecules can result in annihilation of excitons due to their strong interactions.[199–201] The exciton-exciton annihilation has also been observed in one-dimensional structures, such as semiconducting carbon nanotubes.[202,203] However, its observation in quasi 2D systems, such as semiconductor quantum wells, is rare. Since MX_2 monolayers are atomically thin, strong exciton-exciton coupling can be expected. Including exciton-exciton annihilation, the rate equation of the exciton density can be written as

$$\frac{dN}{dt} = -\frac{1}{\tau}N - \frac{1}{2}\gamma N^2, \tag{6.2}$$

where τ and γ are the exciton lifetime and exciton-exciton annihilation rate, respectively.[203] One could attempt to compare the solution of this equation with the data. However, for pedagogical considerations, here we discuss separately contributions of the two mechanisms. This is possible because the exciton-exciton annihilation is only significant in early times when the densities are high, while the single-particle process dominates decays on longer time scales with lower densities. In fact, we find that the data after 150 ps can be satisfactorily fit by a single exponential function, as indicated by the red lines in Fig. 6.11 (left column). Without the first term on the right-hand side, the solution to Eq. 6.2 is simply

$$\frac{N_0}{N(t)} - 1 = \gamma N_0 t, \tag{6.3}$$

where N_0 is the initially injected exciton density at $t = 0$. In viewing of this, we calculate $N_0/N(t) - 1$ from the data shown in each panel in the left column of Fig. 6.11, and plot it as a function of t in the right column. In the first 50 ps, the data are consistent with Eq. 6.3, as indicated by the

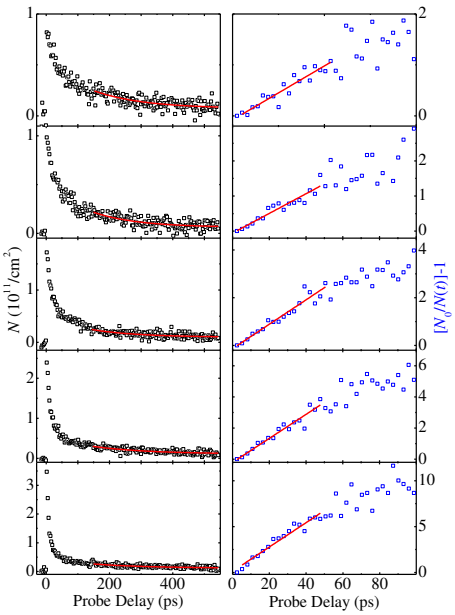

Figure 6.11: Left column: Exciton density, deduced from the measured differential reflection signal, as a function of the probe delay with different injected densities. The red lines are single exponential fits to the data after 150 ps. Right column: the quantity $N_0/N(t)-1$ calculated from data in left column as a function of the probe delay. The red lines are linear fits. Data from Kumar *et al*.[6]

solid lines. We attribute the deviation from linear after 50 ps to the contribution of the first term in Eq. 6.2. From linear fits, shown as the solid lines in Fig. 6.11 (right colume), we deduce the slopes (γN_0). We find that the slope is indeed proportional to N_0, as shown in Fig. 6.12. From a linear fit, shown as the solid line in Fig. 6.12, we obtain an exciton-exciton annihilation rate of $\gamma = 0.33 \pm 0.06$ cm^2/s. We repeat the measurement on two other monolayer samples, and obtained similar results, as summarized in the two insets of Fig. 6.12. The observation of the exciton-exciton annihilation illustrates the strong interaction between excitons in monolayers of $MoSe_2$. In a recent study, strong inter-exciton coupling in monolayers of MoS_2 was revealed, and a fast initial decay of the transient absorption signal was observed; however, no density-dependent behavior reported here was observed.[197]

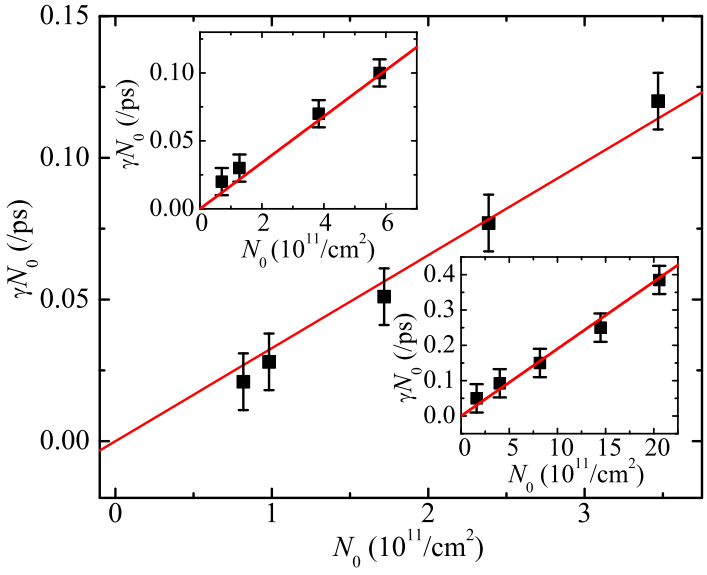

Figure 6.12: Rate of increase of the quantity $N_0/N(t) - 1$, deduced from linear fits shown in the right column of Fig. 6.11, as a function of injected exciton density. The solid line indicate a linear fit. The two insets show similar results from two other samples. Data from Kumar *et al.*[6]

6.3.5 Exciton dynamics in a bulk sample

The observation of the exciton-exciton annihilation in monolayer $MoSe_2$ stimulated us to perform a comparison study on bulk $MoSe_2$. The bulk sample studied is on the same substrate as the monolayer samples, fabricated from the same crystal. The measurement is performed with the same transient absorption setup. Excitons are injected by the 750-nm pump pulse, and probed with the 810-nm pulse.

According to the absorption coefficient at the pump wavelength of 2×10^5/cm,[193] the absorption depth of the pump pulse is about 50 nm. Figure 6.13(a) shows the differential reflection signal measured in a short time range of a few ps, with different pump fluences. As we observed in monolayers, the differential reflection signal rises to a peak quickly, limited by the time resolution.

This indicates the instantaneous saturation effect of the resonantly injected excitons. From these data, we obtain the peak differential reflection signal as a function of the injected exciton density, as shown in Fig. 6.13(b). Here, the bulk exciton density represents its peak value at the center of the pump spot and at the sample surface. It is deduced from the pump fluence and the

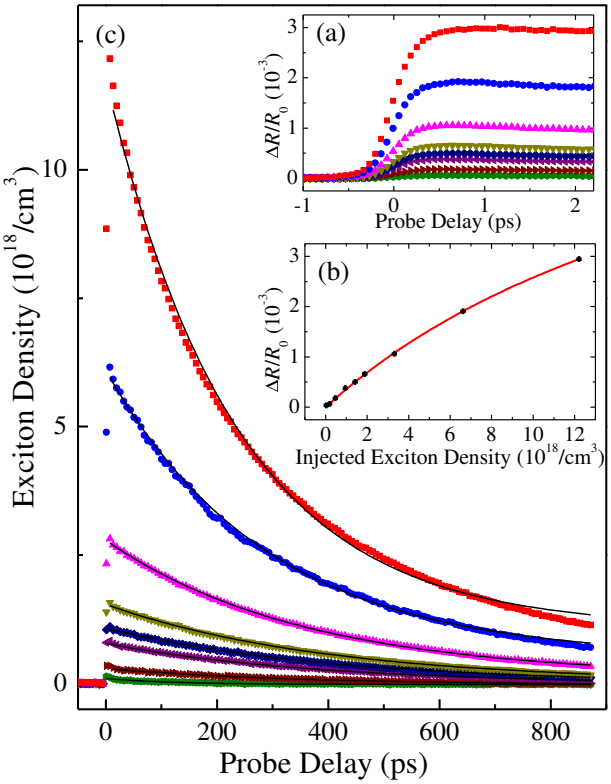

Figure 6.13: Exciton dynamics in bulk $MoSe_2$. (a) Differential reflection signal with the probe delays in a short time range near zero delay measured from a bulk $MoSe_2$ sample. The pump fluences are (from top to bottom) 21.8, 11.8, 5.9, 3.3, 2.5, 1.7, 0.8, and 0.3 μJ/cm^2, respectively. (b) Peak differential reflection signal as a function of the injected peak exciton density. The red line is a fit to the data using Eq. 6.1. (c) Decay of exciton density at different initial injection levels. The solid lines are exponential fits to the data. Data from Kumar *et al.*[6]

absorption coefficient. Similar to the monolayers, the differential reflection signal can be well described by the saturable absorption model (Eq. 6.1), as indicated as the solid line. We obtain a saturation density of $(2.2 \pm 0.3) \times 10^{19}$/cm^3.

Next, we measure the differential reflection signal over a longer time range of about 1 ns with various pump fluences, and deduce the exciton density by using the solid line shown in Fig. 6.13(b). The results are plotted in Fig. 6.13(c). No signature of exciton-exciton annihilation is observed, and all the data can be satisfactorily fit by single exponential functions with time constants in the range of 300 - 400 ps, as indicated as the solid lines in Fig. 6.13(c). We note that the highest density of 1.2×10^{19} /cm^3 used in this measurement corresponds to an areal density of 8.4×10^{11} /cm^2 in the first atomic layer (0.7-nm thick). Finally, we attribute the longer decay time of the

exciton density in bulk sample to longer exciton lifetimes in bulk, probably due to the indirect bandgap and less surface contributions to the exciton recombination.

6.3.6 Summary

In summary, we studied excitonic dynamics in $MoSe_2$ by femtosecond transient absorption and observed exciton-exciton annihilation in monolayers, which is absent in bulk under similar conditions. This process reveals strong coupling between excitons in this strongly confined two-dimensional system. We also found that the exciton density decay time is longer in bulk than monolayers. Furthermore, we observed saturation absorption in both monolayer and bulk, and deduced saturation densities. This observation, combined with the unusually large exciton binding energies, suggest potential uses of $MoSe_2$ monolayers and bulk as saturable absorbers.

Chapter 7

Theoretical foundation of diffusive transport

7.1 Introduction

Transport is the process by which charge carriers move in semiconductors and hence generate currents. There are two basic transport mechanisms in semiconductors: drift and diffusion.

In case of drift the movement of charge takes place due to electric fields, and on the other hand density gradients are main causes of diffusion process. Although there is a net flow of charge in these transport mechanisms, however the system remains in the thermal equilibrium.

When an electric field is applied across the semiconductor, a force on charge carriers develops giving rise to a net movement and net acceleration. This net flow of charge carriers produces current also known as drift current. These charge carriers in a semiconductor are involved in a multiple collisions with atoms resulting in a loss of energy. After each collision charge carrier lose energy and again start to accelerate. This process of colliding and again accelerating gives rise to an average drift velocity v_d and it is related to the applied electric field intensity E and the mobility μ of the charge carriers by,

$$v_d = \mu E. \tag{7.1}$$

The charge carrier drift produces a drift current density J_d. This is the total drift current density due to electrons and holes. The drift current density due to electrons is

$$J_{d(n)} = -env_{d(n)} = -en(-\mu_n E) = +en\mu_n E, \tag{7.2}$$

similarly drift current density due to holes can be represented as

$$J_{d(p)} = epv_{d(p)} = ep(\mu_p E) = ep\mu_p E, \tag{7.3}$$

hence, the total drift current density due to electrons and holes is

$$J_d = (J_{d(n)} + J_{d(p)}) = e(\mu_n n + \mu_p p)E, \tag{7.4}$$

$$= e(\sigma)E, \tag{7.5}$$

where the conductivity (σ) is defined as

$$\sigma = (\mu_n n + \mu_p p). \tag{7.6}$$

In case of diffusion transport mechanism, carriers flow from a region of high concentration toward a region of low concentration. The net flow of these charge carriers produces a diffusion current. According to Fick's law, the flux of charge carriers i.e. the diffusion current density is proportional to the gradient of charge carriers. In the case of electrons as charge carriers, it can be written as:

$$J_{f(n)} = -(-e)D\nabla n, \tag{7.7}$$

where n is the electron density and D is the diffusion coefficient. Similarly for holes as charge

carriers, we have:

$$J_{f(p)} = (e)D\nabla p, \tag{7.8}$$

The total diffusion current density is the sum of diffusion current density due to electrons and holes, which can be written as:

$$J_f = J_{f(n)} + J_{f(p)} = eD\nabla(n+p). \tag{7.9}$$

The total current density is the sum of total drift current density and total diffusion current density:

$$J_{tot} = J_d + J_f. \tag{7.10}$$

The charge carrier mobility demonstrates the movement of charge carriers in a semiconductor in the presence of an electric field. On the other hand diffusion coefficient demonstrates the movement of charge carriers due to a density gradient in a semiconductor. The mobility and diffusion coefficient are related to each other by following equation:

$$\frac{D}{\mu} = \frac{k_B T}{e}, \tag{7.11}$$

this relation between the mobility and diffusion coefficient, is known as the Einstein relation. From the above equation we see that the mobility and diffusion coefficient are strong functions of temperature. Generally, this strong temperature dependence is due to lattice scattering and ionized impurity scattering processes. As we see from the above Einstein relation, measuring the diffusion coefficient and the charge carrier temperature can directly give us the charge carrier mobility.

In our experiments, we directly measure the ambipolar transport in various semiconductors by using ultrafast laser pulses. Excitation by an intense laser pulse generates Gaussian spatial distribution of charge carriers and by studying this spatial distribution dynamics, directly yields the diffusion coefficient of the photoexcited particles. The particles are injected by a focused laser

pulse with a Gaussian shape. Hence, the initial carrier distribution is

$$N(r,0) = N_0 \exp[-\frac{r^2}{\sigma_0^2}], \tag{7.12}$$

where σ_0 is the $1/e$ width of the pump spot. It is related to the full-width at half maxima, w_0, by $w_0 = 2\sqrt{\ln 2}\sigma_0$. After injected, carriers diffusion in the sample plane and recombine. Although exciton formation is unlikely, due to the Coulomb attraction, the electron-hole pair still move as a unit in this ambipolar transport process. The dynamics is described by the ambipolar diffusion equation,[204]

$$\frac{\partial N(r,t)}{\partial t} = D\nabla^2 N(r,t) - \frac{N(r,t)}{\tau}, \tag{7.13}$$

where D and τ are ambipolar diffusion coefficient and carrier lifetime, respectively. Solving this equation, we have,

$$N(r,t) = \frac{\sigma_0^2 N_0}{\sigma^2(t)} \exp[\frac{-t}{\tau}] \exp[-\frac{r^2}{\sigma^2(t)}], \tag{7.14}$$

where $\sigma^2(t) = \sigma_0^2 + 4Dt$. Hence, we expect the profile remains Gaussian, with the squared width increase linearly with time.

7.2 Spatially and temporally resolved optical spectroscopy

Spatially and temporally pump-probe technique is very similar to temporally pump-probe technique discussed in chapter 5. As name indicates, this technique involves both temporally as well spatially resolved degrees of freedom. As discussed in time-resolved pump-probe technique, spatially and temporally resolved pump-probe technique also involve two laser pulses: a pump and a probe. By changing the time delay between the pulses, we can measure the differential reflection signal as a function of time delay and simultaneously by scanning the the probe spot relative to the pump spot, we measure the spatial distribution of the photoexcited particles as a function of time and space.

By using high numerical aperture objective lens, we can focus to a spot size as small as 1.4um.

Tight focus allows the detection of small diffusion coefficient with a high spatial resolution. By calculating FWHM of many space scans in a selected time interval, the diffusion coefficient is estimated. Spatial profiles become broader linearly, with each profile being a Gaussian shape profile, at different time delays. The slope of a linear curve of the FWHM squared with different time delay divided by 16ln(2) indicates the diffusion coefficient.

7.3 Summary

There are two basic transport mechanisms in semiconductors: drift and diffusion. In case of drift the movement of charge takes place due to electric fields and mobility is the main parameter describing the amount of movement, and on the other hand density gradients are main causes of diffusion process and diffusion coefficient is main parameter in this process. The mobility and diffusion coefficient are related to each other by Einstein relation (Eq.7.11).

Spatially and temporally resolved technique is very useful to directly measure the ambipolar transport in various semiconductors. Excitation by an intense laser pulse generates spatial distribution of photoexcited particles in semiconductors. By investigating the spatial and temporal distribution dynamics of photoexcited particles, we can directly measure the diffusion coefficient. With known band structure and excitation energy, mobility can be deducted by using the diffusion coefficient.

Chapter 8

Results and analysis: Diffusive transport

8.1 Introduction

To describe transport properties in semiconductors, diffusion coefficient and hence mobility plays an important role. Spatiotemporal resolved pump-probe techniques can be used to directly measure the diffusion coefficient. In the following sections, results related to transport processes in various 2D materials will be presented in detail. By exploring the expansion of measured spatial profiles as a function of both time and space, the ambipolar diffusion coefficient can be directly deduced. By using the known photoexcited particle temperature, diffusion coefficient can be used to deduce mobility, by the Einstein relation.

8.2 Exciton diffusion in transition metal dichalcogenide MoS_2

The excitons in bulk MoS_2 are excited by using 550nm, 100 fs pump pulses, and monitored by measuring the differential reflection of a 660 nm, probe pulse. The excitons are injected by a focused pump pulse with a Gaussian shape. In order to quantitatively study the exciton dynamics, we measure the Gaussian spatial profiles along $\hat{x}$ axis for many probe delays, with a pump fluence of 10 μJ/cm^2. The results are plotted in Fig. 8.1(a).

Clearly, the profile becomes lower and wider with increasing the probe delay. Figure 8.1(b)

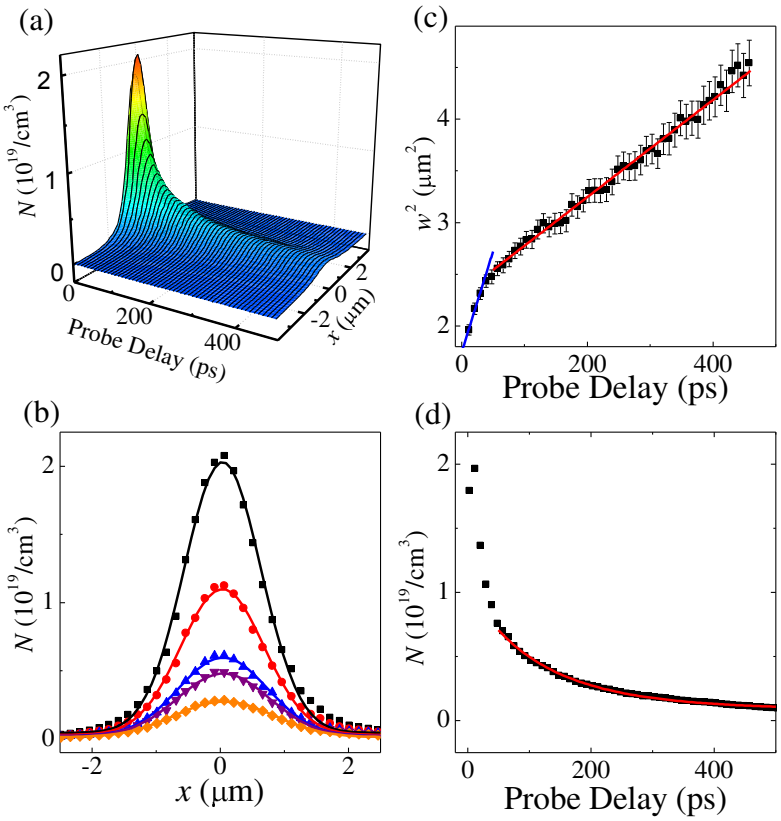

Figure 8.1: (a) Exciton density as a function of probe delay and x over a long delay range of 500 ps. (b) A few examples of the spatial profiles. The probe delays are (from top to bottom) 10, 30, 75, 100, and 200 ps, respectively. (c) Squared width of the spatial profile of the signal as a function of probe delay. The red line is a linear fit to the data points after 50 ps, which corresponds to a diffusion coefficient of 4.2 cm^2/s. The blue line indicates the initial slope, which gives a diffusion coefficient of 18 cm^2/s. (d) the exciton density measured at $x = 0$ with the finite probe spot. The red line indicates a fit that gives a lifetime of 180 ps. Data from Kumar *et al.*[5]

shows a few examples of the measured profiles, with the corresponding Gaussian fits (solid lines). The squared widths deduced from the fits to all the measured profiles are plotted in Fig. 8.1(c). After about 50 ps, the increase becomes linear, as expected from the ambipolar diffusion model. From a linear fit (red line), we deduce a diffusion coefficient of 4.2 $\pm$ 0.4 cm^2/s. We note that although the penetration depth is only on the order of 20 nm due to strong absorption, the diffusion of excitons along perpendicular direction is expected to be much slower due to the layered structure of MoS_2.

By using the Einstein relation, $D/k_BT = \mu/e$, we estimate the exciton mobility, corresponds to the measured D after 50 ps, on the order of 170 $\pm$ 20 cm^2/Vs.

The spatiotemporal resolution of the carrier density also allows us to deduce the exciton lifetime. Figure 8.1(d) shows the measured exciton density as a function of probe delay with the probe spot overlapped with the pump spot ($x = 0$). The decrease of the exciton density is caused by both the exciton recombination and the transport of excitons out of the probing area. To deduce the exciton lifetime, we consider that the intensity of the Gaussian-shaped probe spot, with the center overlapped with the center of the exciton density profile, is

$$I(r) = I_0 \exp[-\frac{r^2}{\sigma_p^2}], \tag{8.1}$$

where I_0 is on-axis peak intensity, and σ_p is the $1/e$ width of the probe spot. By integrating the product of such a sensitivity function with the exciton density profile, we find that the exciton density measured by such a probe,

$$N(x = 0) \propto \frac{1}{\sigma_p^2 + \sigma_0^2 + 4Dt} \exp[\frac{-t}{\tau}], \tag{8.2}$$

Here, the first factor describes the effect of diffusion of excitons out of probing area, and the second factor accounts for recombination. We use Eq. 8.2 to fit the data shown in Fig. 8.1(d), with the known value of D. We obtain a satisfactory agreement with the data (red curve), and deduce a exciton lifetime of 180 ± 20 ps.

We note that since MoS_2 has an indirect bandgap, the radiative recombination of excitons is restricted by crystal momentum conservation. Accordingly, one would expect a long exciton lifetime due to radiative recombination. The short lifetime deduced here is probably limited by nonradiative recombination at defects and surface.

8.3 Exciton diffusion in transition metal dichalcogenide $MoSe_2$

As discussed in chapter 5, because of the unusually large exciton binding energies in 2D thin films of TMD crystals, their optical properties are dominated by excitons even at room tempera-

ture. In particular, real-space transport and recombination of excitons play important roles in optoelectronic applications. Although a recent time-integrated photoluminescence experiment demonstrated electrical control of neutral and charged excitons,[191] the exciton dynamics has not been studied in neither monolayer nor bulk $MoSe_2$.

Here we report a study of exciton dynamics in monolayer and bulk $MoSe_2$ by femtosecond transient absorption microscopy. The high spatiotemporal resolution allows us to directly measure the exciton diffusion coefficient and lifetime. These results provide fundamental parameters for understanding excitons in these structures.

8.3.1 Experimental section

Samples of monolayer $MoSe_2$ are fabricated by mechanical exfoliation with an adhesive tape from bulk crystals. By depositing flakes of $MoSe_2$ on silicon substrates with a 90-nm SiO_2 layer, we can identify thin layers of $MoSe_2$ with an optical microscope, by utilizing optical contrasts enhanced by the multilayer substrate.[63,65] The inset of Fig. 8.2 shows the microscope picture of a large and isolated flake used in this study. The contrast of the flake with respect to the substrate is consistent with a monolayer thickness.[63,65]

Under excitation of a 632.8-nm laser beam, strong photoluminescence with a central wavelength of 788 nm is observed, as shown as the red curve in Fig. 8.2, which is consistent with recently reported photoluminescence peak wavelengths in the range of 784 - 794 nm.[25,191,205] The linewidth is about 22 nm, which is also in the range of the recently reported values of 15 - 50 nm.[191,205] The blue curve in Fig. 8.2 (top and right axes) shows a Raman spectrum of the sample, with two peaks at 242 and 286 cm^{-1}, corresponding to the A_{1g} and E^1_{2g} phonon modes of monolayer $MoSe_2$, respectively. These values, as well as the ratio of the peak heights of about 13, are reasonably consistent with the reported results of monolayer $MoSe_2$.[25,78,205–207]

In the transient absorption microscopy setup, as shown schematically in Fig. 8.3, a 750nm pump and an 810nm probe combination is to get differential reflection signal. The pump pulse is tuned to the high-energy edge of the A-exciton resonance (Fig. 8.2); hence, it resonantly injects

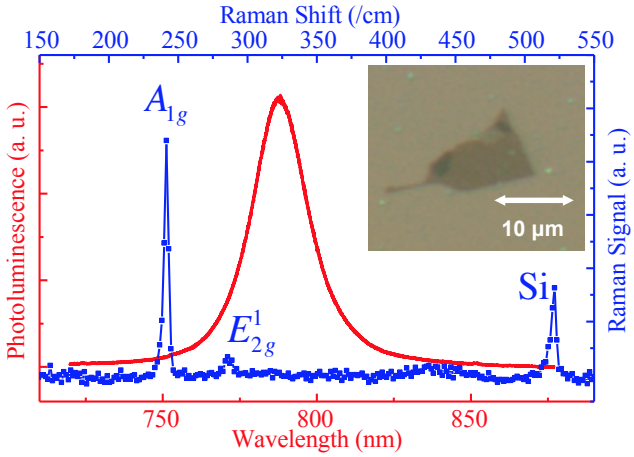

Figure 8.2: Photoluminescence (red, left and bottom axes) and Raman (blue, right and top axes) spectra of the monolayer $MoSe_2$ flake used for the study, which is shown in the inset. Data from Kumar *et al*.[7]

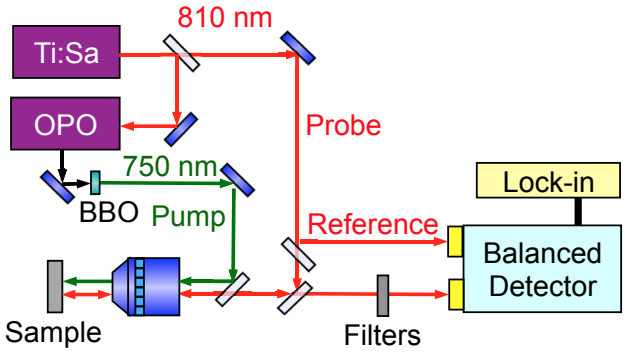

Figure 8.3: Schematics of the transient absorption microscopy setup. Data from Kumar *et al*.[7]

excitons.

The total reflection of the probe is determined by the reflection from the sample surface and from the interfaces of sample/SiO_2 and SiO_2/Si. Consequently, the differential reflection is related to changes of the complex index of refraction of $MoSe_2$ induced by the excitons injected by the pump pulse. Strictly speaking, the relation between the differential reflection and the exciton density can be complex and often non-analytical.

However, for low exciton densities and small magnitudes of differential reflection, the relation is often linear. For our purpose of monitoring exciton dynamics with differential reflection, we verify that the differential reflection is proportional to the exciton density by measuring the differential reflection at early probe delays as a function of the pump fluence. With the known

absorption coefficient at the pump wavelength,[193] we deduce the injected exciton density from the pump fluence by using Beer's Law and assuming each absorbed photon creates one exciton.

We find that a differential reflection of 10^{-4} corresponds to an area exciton density of 10^{11} /cm^2. We use this relation to convert the measured differential reflection to the exciton density. We note that any uncertainties in this process merely change the absolute value of the labeled exciton densities, and would not influence our discussions on exciton dynamics.

8.3.2 Results and discussion

We spatially and temporally resolve the excitonic dynamics by measuring the differential reflection as we scan the probe spot with respect to the pump spot at various probe delays. Figure 8.4(a) shows the deduced exciton density as a function of time and space. The zero probe location is defined where the centers of the probe and pump spots overlap. To analyze the broadening of the profiles, we fit the profiles at different probe delays by Gaussian functions to determined their $1/e$ widths (σ). The results are plotted in Fig. 8.4(b). A significant broadening of the profile can be seen, which is caused by diffusion of excitons out of the excitation region.

The spatiotemporal dynamics of the injected excitons can be described by the diffusion equation.[204] With a Gaussian initial profile, the profile remains Gaussian with the width evolving as $\sigma^2(t) = \sigma_0^2 + 4Dt$, where D and σ_0 are the diffusion coefficient and the width of the initial density profile at $t = 0$, respectively. By fitting the data with this equation, as shown as the red line in Fig. 8.4(b), we deduce a diffusion coefficient of 12 ± 3 cm^2/s. We note that this procedure to measure the diffusion coefficient is not influenced by the decay of the overall exciton density due to the exciton recombination, which does not change the width. Furthermore, the finite probe spot size does not influence the measurement neither, since it merely adds a constant to all the squared widths, and hence does not change the slope.

The spatiotemporal resolution of the exciton density also allows us to measure the exciton lifetime. Figure 8.4(c) shows the measured exciton density as a function of probe delay with the centers of the probe and pump spots overlap ($x = 0$). The decrease of the exciton density

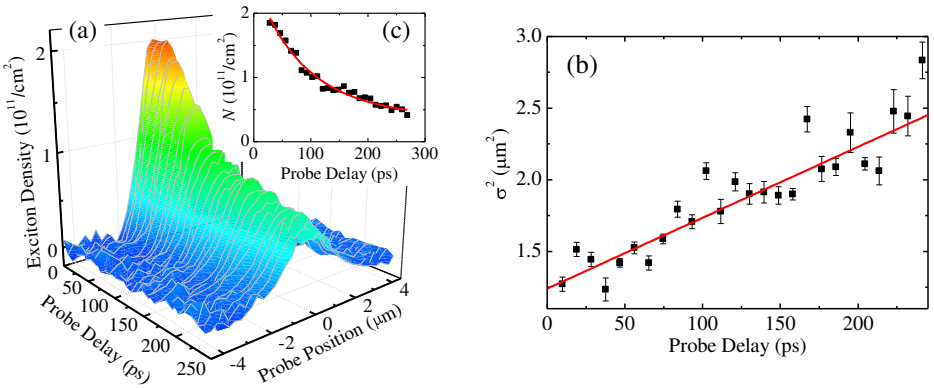

Figure 8.4: (a) Spatiotemporal dynamics of exciton in monolayer $MoSe_2$. (b) Square widths of the profiles at various probe delays determined by Gaussian fits to the profiles shown in (a). The red line is a linear fit. (c) The exciton density measured at the zero probe position as a function of probe delay. The red line is a fit that includes contributions of both the recombination and the diffusion. Data from Kumar *et al.*[7]

is caused by both the diffusion and the exciton recombination. Considering the probe spot is Gaussian with a finite size, σ_p, it is straightforward to show that the exciton density is $N(x=0) \propto \frac{1}{\sigma_p^2+\sigma_0^2+4Dt}\exp[\frac{-t}{\tau}]$. We fit the data shown in Fig. 8.4(c) with this equation, with the known value of D, and find a satisfactory agreement [red curve in Fig. 8.4(c)]. We deduce an exciton lifetime of 130 ± 20 ps.

The measured exciton diffusion coefficient and lifetime reveal fundamental interactions between excitons and their environment in $MoSe_2$ monolayers. From these values, we deduce a diffusion length ($\sqrt{D\tau}$) of about 400 nm and a mean free time (D/v_T^2, where v_T is the thermal velocity) of about 0.2 ps. Study of exciton transport can also provide insight to charge transport properties in $MoSe_2$, which are important for various electronic applications. From the Einstein relation, we obtain an exciton mobility of $\mu = eD/k_BT \sim 480$ cm^2/Vs, where e, k_B, and T are elementary charge, Boltzmann constant, and temperature, respectively. This value is about one order of magnitude higher than an electron mobility of about 50 cm^2/Vs in a seven-layer flake of $MoSe_2$ obtained in a recent transport measurement.[208] We note that the exciton mobility is related to, but different from, the charge mobilities. Excitons are neutral particles, and therefore their interactions with charged impurities and piezoelectric types of phonons are weaker than charge carriers.

We repeat the measurement on a thick flake fabricated from the same crystal and on the same

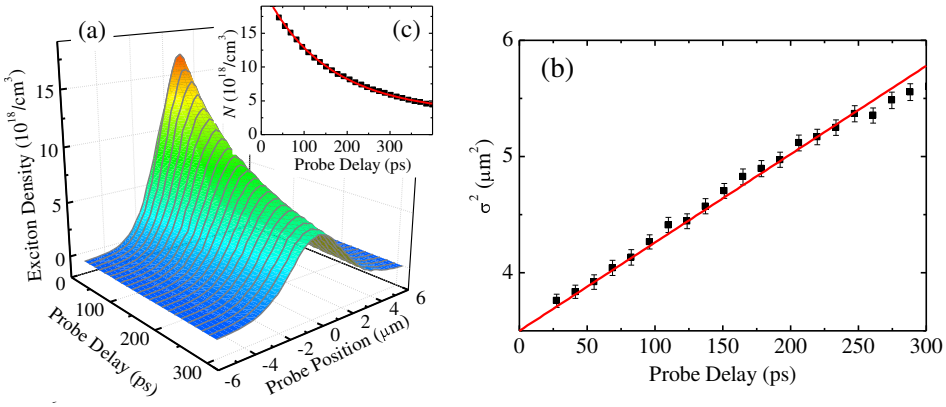

Figure 8.5: (a) Spatiotemporal dynamics of exciton in bulk $MoSe_2$. (b) Square widths of the profiles at various probe delays determined by Gaussian fits to the profiles shown in (a). The red line is a linear fit. (c) The exciton density measured at the zero probe position as a function of probe delay. The red line is a fit that includes contributions of both the recombination and the diffusion. Data from Kumar *et al.*[7]

substrate. The exact number of atomic layers is unknown; however, because it is not transparent, its thickness is at least several hundred nanometers. Since the penetration depth of the pump pulse is about 50 nm, it can be safely treated as a bulk sample. Figure 8.5 summarizes the results from this bulk sample, in the same fashion as Fig. 8.4. By analyzing these data, we obtain a diffusion coefficient and a lifetime of 19 ± 2 cm^2/s and 210 ± 10 ps, respectively. These values correspond to a diffusion length of about 600 nm, a mean free time of about 0.3 ps, and an exciton mobility of about 730 cm^2/Vs. Previously, charge mobilities on the order of 100 cm^2/Vs have been measured in bulk $MoSe_2$.[209] Furthermore, an earlier photoemission measurement yielded an *interlayer* diffusion coefficient on the order of 1 cm^2/s.[210] The significantly faster *intralayer* diffusion observed here illustrates the anisotopic transport property of this layered material.

By comparing our results of monolayer and bulk, we note that the quantum confinement in monolayer does not change the exciton diffusion coefficient dramatically, despite of its significant impact on the nature of the bandgap and the optical properties. This is, however, consistent with previous electrical measurements on MoS_2, where similar mobilities were obtained in flakes with different thicknesses.[56] We suggest that the slightly smaller diffusion coefficient in monolayer is due to additional scattering mechanisms from the substrate. To fully understand this, measurements on monolayer samples that are either suspended or on other types of substrates are desired.

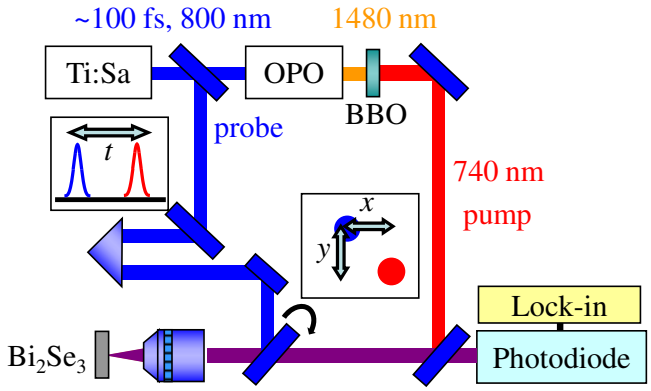

Figure 8.6: Schematics of the transient absorption setup. Data from Kumar *et al.*[4]

Furthermore, the shorter lifetime in monolayer can be attributed to the enhanced recombination due to the direct bandgap.

8.4 Hot carrier diffusion in topological insulator Bi_2Se_3

To explore hot carrier diffusion in topological insulator Bi_2Se_3, hot carriers were excited using 740nm pump pulse with a spot size of 2.4 μm FWHM. The probe wavelength was set to 800nm and focused to a spot size of 4 μm FWHM. The probe spot is scanned with respect to the pump spot on the sample surface by tilting the beam-splitter that sends the probe beam to the objective lens. The time delay between the probe and the pump pulses is controlled by moving a reflector in the probe arm. The respective experimental configuration is shown in Fig. 8.6. With this configuration bunch of space scans were taken at different probe delays.

By using the broadening of spatial profiles of DR signal, we deduce the diffusion coefficient of Bi_2Se_3. The red circles in Fig. 8.7 clearly show that the profile expands from about 2.8 μm to more than 3.0 μm within the first 2 ps. During this time, the height of the profile [blue squares in Fig. 8.7] decreases. If the broadening is caused by diffusion of hot carriers or phonons, the squared width is expected to expand linearly with a slope of about $16\ln(2)D$, where D is the diffusion coefficient.[13] Therefore, the observed expansion corresponds to a diffusion coefficient on the order of 500 cm^2/s. Previous experiments have shown that the thermal diffusion coefficient

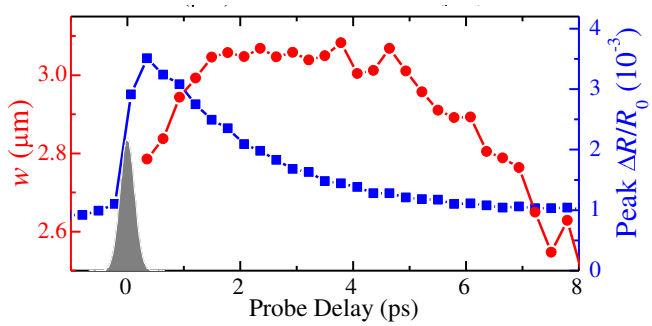

Figure 8.7: The width (FWHM) of the profile as a function of probe delay(the squares, left axis). The solid line (right axis) shows the peak differential reflection signal as a function of the probe delay. Data from Kumar *et al.*[4]

of Bi_2Se_3 is about 0.3 cm^2/s,[186] three orders of magnitude smaller than what we observed. Hence, we conclude that the spatial expansion is caused by diffusion of the photoexcited hot carriers. We note that in the diffusion process the excited electrons and holes move as pairs due to the Coulomb interaction between them. The quantity measured is therefore the ambipolar diffusion coefficient.

The expansion of the profile can reflect the carrier diffusion via two possible mechanisms. If the differential reflection signal is dominated by the carriers, the expansion directly measures the carrier diffusion. If the differential reflection signal is mainly caused by phonons, the expansion is induced by phonon emission of the carriers that have diffused out of the original profile.

8.5 Summary

The carrier dynamics in bulk MoS_2 can be well described by diffusion of photoexcited excitons, with a diffusion coefficient of 4.2 ± 0.4 cm^2/s which corresponds to a mobility of 170 ± 20 cm^2/Vs and a lifetime of 180 ± 20 ps. These results provide fundamental information on exciton dynamics in bulk MoS_2 crystals, and can be used to understand exciton dynamics of MoS_2 thin atomic layers.

In case of $MoSe_2$, we performed time-resolved study on exciton dynamics in monolayer and bulk $MoSe_2$. We obtained exciton lifetimes of 130 ± 20 and 210 ± 10 ps in the monolayer and bulk samples, respectively. The shorter lifetime in monolayer $MoSe_2$ reflects the recombination enhancement due to its direct band structure. By time resolving the evolution of the exciton density

profiles, we directly measured diffusion coefficients of 12$\pm$ 3 and 19 $\pm$ 2 cm^2/s in the monolayer and bulk samples, respectively. Using these results, we further deduced other important parameters of excitons, such as the diffusion length, the mobility, and the mean free time. These parameters are important for understanding excitons and their interactions with the environment in these structures, and potential applications of $MoSe_2$ in optoelectronics and electronics.

Finally, in Bi_2Se_3 the spatial expansion of the differential reflection profile allows us to estimate an ambipolar carrier diffusion coefficient on the order of 500 cm^2/s.

Chapter 9

Valley and spin dynamics in transition metal dichalcogenide $MoSe_2$

9.1 Introduction

As discussed in earlier chapters, semiconducting transition metal dichalcogenides, MX_2 (M=Mo, W; X=S, Se, Te), have drawn considerable attention since 2010.[52] Similar to graphene,[8] the weak van der Waals interlayer coupling in these layered crystals allows fabrication of atomically thin two-dimensional (2D) films.[68] These 2D crystals have properties that are remarkably different from their bulk counterparts,[21,53,54] and have shown potential applications in electronics[56,211,212] and optoelectronics.[19,20,213–215]

Due to their unique spin and valley properties,[34–36] MX_2 2D crystals have also merged as promising materials for spintronics[37–39] and valleytronics,[40] where spin degree of freedom or valley index of electrons is used for information processing.

9.2 $MoSe_2$: Band structure and spin states

Figure 9.1(a) shows a top view of the lattice structure of a MX_2 monolayer. It is composed of one layer of *M* atoms (blue circles) that is sandwiched by two layers of *X* (yellow circles). Since this

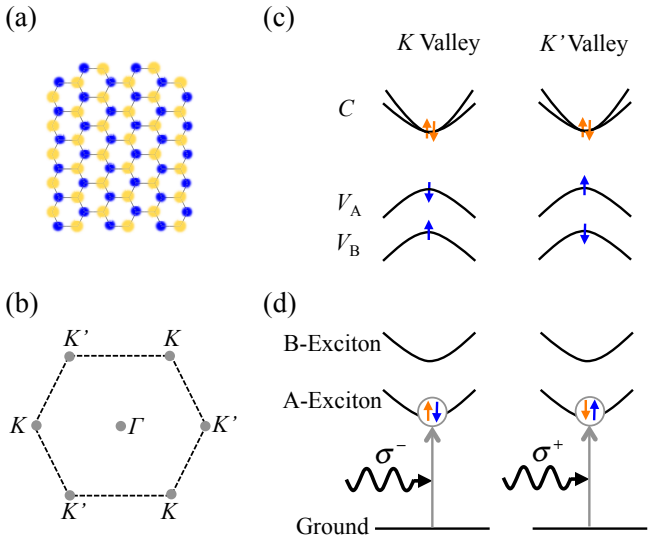

Figure 9.1: (a) Lattice structure of MX_2 2D crystals. Each yellow circle represents two X atoms vertically separated. The blue circles indicate the plane of M atoms located between the two X planes. (b) Energy valleys K and K' in momentum space. (c) Electronic structures in K (left) and K' (right) valleys, showing the conduction (C) and valance (V_A and V_B) bands that their spin states (up and down arrows). (d) Spin configurations of the bright excitons in the two valleys and their coupling to circularly polarized light.

lattice is not inversion symmetric, in momentum space the 6 energy valleys form two inequivalent sets, labeled as K and K' in Fig. 9.1(b), respectively. Figure 9.1(c) shows the conduction band (C) and the valence bands [V_A (spin 3/2), V_B (spin 1/2)] in K (left) and K' (right) valleys, respectively. The large spin splitting in the valance bands (several hundreds of meV) is induced by the spin-orbital coupling in d orbitals of the X atoms.[216–218] The unique aspect of the spin property in MX_2 2D crystals is that, the spin and valley degrees of freedom of holes in the valance bands are inherently coupled: Time-reversal symmetry and the lack of inversion symmetry in space dictate that the spin splitting at different valleys must be opposite.[34,219] As illustrated in Fig. 9.1(c), in the K valleys, the spin-down (spin -3/2) and spin-up (spin +1/2) holes occupy the V_A and V_B bands, respectively; while in the K' valleys the spin occupation is opposite. Since holes in opposite valleys carry opposite Berry curvatures and spin moments, a number of interesting phenomena are resulted, such as spin and valley Hall effects.[34,36,220–223] In both valleys, the conduction bands (C) are degenerate near the bottom of the bands.

One important consequence of these spin and valley structures is the spin- and valley-selective

optical coupling.[34–36] Optical properties of MX_2 2D crystals are dominated by excitons due to their large binding energies. Figure 9.1(d) shows the two exciton bands, A and B, formed by the holes in V_A and V_B, respectively, with electrons in the conduction bands. Since in the K valleys only spin-down holes populate V_A, an A-excitons in K valley is formed by a spin-down hole (-3/2) with either a spin-up (+1/2) or a spin-down (-1/2) electron. The former [shown in Fig. 9.1(d)] has a net spin of -1 (spin-down exciton) and therefore couples to σ^- photons, while the latter, with a net spin of -2, is a dark exciton that does not couple to photons (not shown). On the other hand, in the K' valleys, a bright A-exciton is formed by a spin-up hole (+3/2) and a spin-down electron (-1/2), with a net spin of +1 (spin-up exciton), and hence couples to σ^+ photons. Based on these selection rules, a circularly polarized light can inject spin- and valley-polarized excitons in MX_2 2D crystals,[34–36] which then emit circularly polarized photoluminescence. This effect has been observed by several groups in steady-state photoluminescence experiments.[35,189,194,224–228] Dynamics of spin and valley polarized excitons have also been revealed in time-resolved photoluminescence[229] and transient absorption[230,231] measurements.

Here we demonstrate optical injection and detection of valley- and spin-polarized excitons in $MoSe_2$ monolayers at room temperature by polarization-resolve transient absorption measurements. We deduce a valley relaxation time of 9 ± 3 ps in monolayer samples at room temperature. Previous observations of valley polarization have mostly focused on one member of MX_2, MoS_2,[35,189,194,224–228,230,231] and were limited to low sample temperatures. Our results illustrate potential applications of $MoSe_2$ 2D crystals for room-temperature valleytronics and spintronics.

9.3 Experimental section

Thin flakes of $MoSe_2$ are mechanically exfoliated from bulk crystals, and then deposited on silicon substrates with a 90-nm SiO_2 layer. Monolayer flakes are first identified according to their optical contrasts with an optical microscopy,[63,65] and then confirmed by photoluminescence[25,191,205] and Raman spectroscopy.[25,78,205–207]

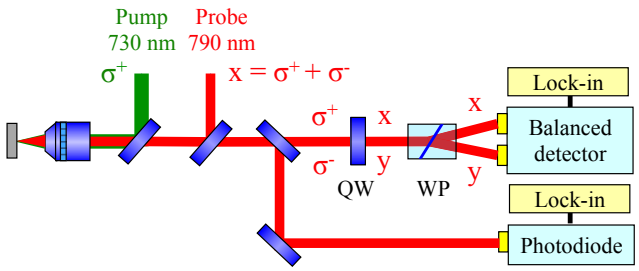

Figure 9.2: Polarization resolved differential reflection setup to measure pump-induced circular dichroism, which reflects spin and valley dynamics of excitons (QW: quarter-wave plate, WP: Wollaston prism).

Figure 9.2 illustrates the experimental setup. A left-circularly polarized (σ^+) pump pulse with a 730-nm central wavelength and 100-fs temporal width resonantly injects excitons in the sample. The pulse is tightly focused to about 1 μm and is located at the center of the monolayer flake to avoid any potential effects from the flake boundary. According to the selection rules illustrated in Fig. 9.1(d), spin-up excitons are injected in the K' valleys. The dynamics of these excitons is probed by using a linearly polarized (x) pulse tuned to the A-exciton resonance (790 nm), by utilizing the dynamical circular dichroism induced by the valley- and spin-polarized excitons.

It has been well established that an exciton population can change the absorption coefficient of a semiconductor by various mechanisms such as phase-space state filling, screening, bandgap renormalization, etc.[232] For low and even moderate densities, the change in absorption coefficient is proportional to the exciton density.[232] In our measurements, this change is monitored by differential reflection, which is defined as the relative change of the probe reflection induced by the excitons, $\Delta R/R_0 \equiv (R(N) - R_0)/R_0$, where $R(N)$ and R_0 are probe reflections with and without excitons, respectively.

The x-polarized probe has two circular components, σ^+ and σ^-, of the equal magnitude. We first consider the σ^- component. The differential reflection of a σ^--polarized light can be written as

$$\frac{\Delta R^-}{R_0} = C_1 N_\downarrow + C_2 N_\uparrow, \tag{9.1}$$

where $N_\downarrow$ and $N_\uparrow$ are the densities of spin-down and spin-up excitons, respectively. The coefficients

C_1 and C_2 describe the effectiveness of spin-down and spin-up excitons in altering the absorption of σ^- probe. Here C_2 originates from spin-insensitive mechanisms, while C_1 is from both spin-insensitive and spin-sensitive processes. Hence, $C_1 > C_2$. That is, the spin-down excitons, or excitons in the K' valley, are more efficient in altering the absorption of σ^- light. Similarly, the differential reflection of the σ^+ component,

$$\frac{\Delta R^+}{R_0} = C_1 N_\uparrow + C_2 N_\downarrow. \tag{9.2}$$

By measuring the sum and difference of these two components, we obtain

$$\frac{\Delta R^+}{R_0} + \frac{\Delta R^-}{R_0} = (C_1 + C_2)(N_\uparrow + N_\downarrow) = (C_1 + C_2)N, \tag{9.3}$$

and

$$\frac{\Delta R^+}{R_0} - \frac{\Delta R^-}{R_0} = (C_1 - C_2)(N_\uparrow - N_\downarrow) = (C_1 - C_2)S, \tag{9.4}$$

where N and S are the exciton and spin (valley) densities, respectively. Furthermore,

$$\frac{\Delta R^+ - \Delta R^-}{\Delta R^+ + \Delta R^-} = \frac{C_1 - C_2}{C_1 + C_2}\frac{S}{N} = \frac{C_1 - C_2}{C_1 + C_2}P, \tag{9.5}$$

where P is defined as spin and valley polarizations of the excitons.

As shown in Fig. 9.2, to separate the two circular components of the probe, a portion of the reflected probe is sent through a quanter-wave plate (QW) with the fast axis oriented such that it converts the two circular components to x and y linear polarizations. A Wollaston prism (WP) separates the two components, which are measured by the two photodiodes of a balanced detector. Since the balanced detector outputs an voltage that is proportional to the difference between the optical powers on the two detectors, it monitors the difference of the two differential reflections, and hence the spin density. This output is measured by a lock-in amplifier synchronized with a mechanical chopper in the pump arm, which modulates the pump intensity at about 3,000 Hz. The other portion of the reflection probe is measured directly by another photodiode, which monitors

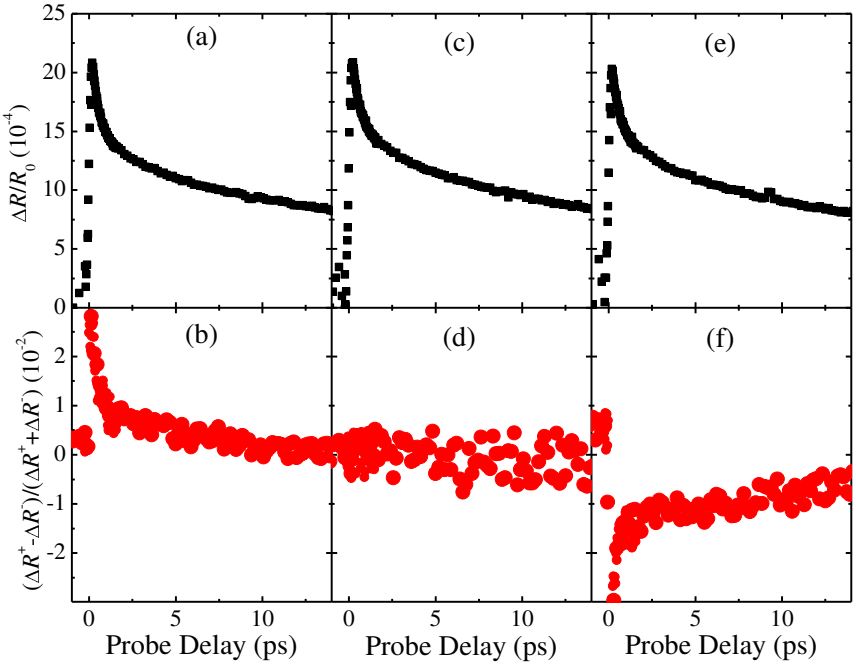

Figure 9.3: Differential reflection (a, c, e) and the ratio between difference and sum of the two circular components (b, d, f) of monolayer $MoSe_2$ measured with pump pulses of σ^+ (a, b), x (c, d), and σ^- (e, f) polarizations, respectively.

the sum of the two spin systems, *i. e.* total exciton density.

9.4 Results and discussion

Figure 9.3(a) shows the measured $\Delta R/R_0$ as a function of the probe delay after excitons are injected by a σ^+-polarized pump pulse with a central wavelength of 730 nm. The peak density of the injected excitons is about 5×10^{11} /cm^2, which is estimated from the pump fluence used and the absorption coefficient of the sample at the probe wavelength. Since $\Delta R/R_0$ measures the total exciton density, its decay reflects loss of exciton density due to recombination. After an initial rapid decay, which has a time constant of about 0.5 ps, the signal decreases slowly. A separate measurement over a longer time range (not shown) yields a relatively long decay time of 130 ps. We attribute the short time constant to thermalization and energy relaxation of excitons, and the long time constant to the exciton lifetime.

Figure 9.3(b) shows $(\Delta R^+ - \Delta R^-)/(\Delta R^+ + \Delta R^-)$ as a function of the probe delay. This quantity

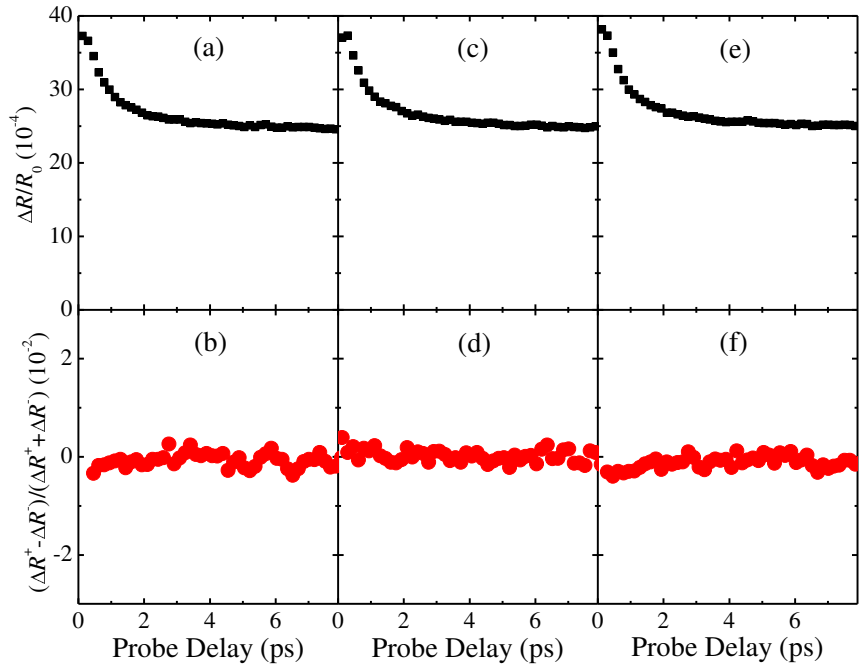

Figure 9.4: Differential reflection (a, c, e) and the ratio between difference and sum of the two circular components (b, d, f) of bulk $MoSe_2$ measured with pump pulses of σ^+ (a, b), x (c, d), and σ^- (e, f) polarizations, respectively.

is obtained by measuring $\Delta R^+ - \Delta R^-$ and $\Delta R^+ + \Delta R^-$ simultaneously with the two detectors shown in Fig. 9.2, and then take the ratio numerically. As shown in Eq. (8.5), this quantity is proportional to the valley and spin polarizations of the excitons. Clearly, a positive polarization is injected by the pump, which decays quickly. We find that the decay can be described by a bi-exponential function (red line), with a short time constant of 0.36 ± 0.05 and a long time constant of 9 ± 3 ps, respectively. We speculate that the short time constant has the same origin as the fast component in the ordinary differential reflection. The long time constant reflects the relaxation of the valley and spin polarization to zero. Hence, it is the valley and spin relaxation time.

Next, we change the pump polarization to x. Since the linearly polarized light has two circular components of the same magnitude, it injects the same number of excitons to the two valleys, without a net valley or spin polarization. Consequently, no spin signal is observed, as confirmed in Fig. 9.3(d). Figure 9.3(c) shows that the exciton recombination is not changed from Figure 9.3(a). Hence, the exciton recombination rate is independent of the valley and spin polarization.

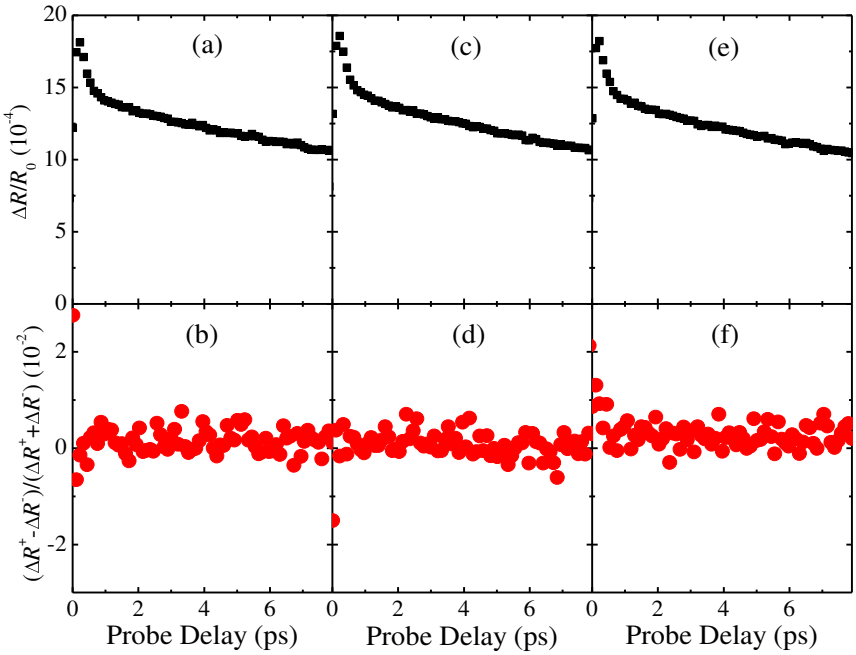

Figure 9.5: Differential reflection (a, c, e) and the ratio between difference and sum of the two circular components (b, d, f) of a few-layer $MoSe_2$ flake with pump pulses of σ^+ (a, b), x (c, d), and σ^- (e, f) polarizations, respectively.

Finally, we change the pump to σ^- to inject excitons with an opposite valley and spin polarization. As clearly shown in Figure 9.3(f), the sign of the spin signal flips, while the dynamics remain the same. The differential reflection signal still remains unchanged, as shown in Figure 9.3(e).

The optical selection rules illustrated in Fig. 9.1(d) holds only for monolayers. In bulk $MoSe_2$ with inversion symmetry, optical transitions become independent of spin and valley. To confirm this, we repeat the measurement summarized in Fig. 9.3 with a thick flake that is fabricated together with the monolayer flake and on the same substrate. The results are plotted in Fig. 9.4. As we expected, no spin polarization is injected nor detected. The exciton lifetime is longer than monolayers, due to the indirect bandgap in bulk. We also studied a few-layer flake as an intermediate case, which contains about 5 - 7 layers, estimated from its optical contrast. As shown in Fig. 9.5, no spin signal is detected, and the exciton lifetime is in between the bulk and the monolayer. The absence of spin-dependent signal in few-layer and bulk samples confirms the selection rule illustrated in Fig. 9.3(d) is unique to monolayers. It also ensures that the spin signal we observed in monolayers is not due to artifacts from the measurement.

Previously, transient absorption technique has been used to study valley dynamics in MoS_2 monolayers at low temperatures.[230,231] Valley relaxation times of a few picosecond and sub-picosecond have been deduced from these measurements. Our study shows that a longer valley relaxation time can be achieved in $MoSe_2$ monolayers even at room temperature. Recently, several group have observed circularly polarized photoluminescence in MoS_2 monolayers;[35,189,194,224–228] but there has been no report on such observations in $MoSe_2$. Based on our results, the exciton lifetime (130 ps) is much longer than the valley relaxation time (9 ps). Furthermore, since nonradiative recombination likely contributes to the lifetime too, the radiative recombination time can be expected to be even longer. Therefore, it is reasonable that time-integrated measurements cannot effectively detect circularly polarized photoluminescence.

We note that the detected peak signal of $(\Delta R^+ - \Delta R^-)/(\Delta R^+ + \Delta R^-)$ is only about 0.02. Although a circularly polarized pump is expected to inject 100% valley polarization, as dictated by the selection rules, such rules are relaxed when moving away from the K and K' points (or the bottom of the bands), due to state mixing. In our measurements, the excitation access energy of the pump is about 120 meV. Hence, it is expected to inject excitons with a valley polarization lower than unity. Furthermore, according to Eq. (8.5), the efficiency of using transient absorption to probe valley polarization is determined by the coefficients C_1 and C_2. In particular, if the mechanisms that cause transient absorption are dominated by valley- and spin-independent ones, such as screening effects, the values of C_1 and C_2 are expected to be close, resulting in a low detection efficiency. Nevertheless, this does not change the conclusion on the measurement of valley relaxation time.

9.5 Summary

We have performed the first experimental study on valley and spin dynamics in monolayer $MoSe_2$, an important member of the newly developed 2D crystals. We demonstrated optical injection of valley- and spin-polarized excitons in this material by a circularly polarized pulse, utilizing the

unique optical selection rules of monolayer transition metal dichalcogenides. Evolution of the injected valley polarization is monitored by measuring dynamical circular dichroism of a probe pulse tuned to the exciton resonance. We obtained a valley relaxation time of 9 ± 3 ps at room temperature. Our study demonstrated a new 2D crystal for room temperature valleytronics and spintronics, and illustrated prospects of using heterostructures formed by different 2D crystals for valleytronics and spintronics.

Chapter 10

Summary and future work

In this dissertation, I used ultrafast laser techniques to study various properties of 2D materials. The majority of the work presented belongs to photoexcited quasiparticles. Hence, the dissertation started with the introduction of general theory of optics, which is necessary to understand the various optical processes that arise due to the interactions of light and matter.

Two important aspects of nonlinear light-matter interactions, one related to second- and third-order nonlinearity, were discussed in Chapter 3.

In Chapter 4 and 5, we considered a detailed study of photoexcited quasiparticle dynamics in 2D materials by using time resolved ultrafast spectroscopy.

Chapter 6 provided results on photoexcited quasiparticle dynamics of Bi_2Se_3, MoS_2, and $MoSe_2$. In first section of the chapter, carrier and phonon dynamics in Bi_2Se_3 crystal were studied. Pronounced oscillations in differential reflection signal were observed with two distinct frequencies and are attributed to coherent optical and acoustic phonons, respectively. The second and third parts of Chapter 5 consisted of a transient absorption microscopy study of charge carrier and exciton dynamics in MoS_2 and $MoSe_2$ crystals.

In Chapter 8, we investigated diffusion coefficient of photo excited particles in MoS_2, $MoSe_2$, and Bi_2Se_3 by including spatial degrees of freedom in time-resolved ultrafast spectroscopy.

Finally, Chapter 9 covers valley and spin dynamics in monolayer $MoSe_2$ by polarization-

resolved femtosecond transient absorption spectroscopy. The results illustrated potential applications of $MoSe_2$ in room-temperature valleytronic and spintronic devices.

The performance of electronic devices has been greatly improved by reducing their size throughout their development. However, due to the continuous reduction in the device size, the current implemented feature size is very close to the physical limit. Hence, one of the major obstacles confronting material science is the difficulty in developing new materials for the advancement of technology, especially artificial materials possessing designed properties. One major approach adopted since the 1980's is to control the dimension in the so-called nanomaterials, including zero-dimensional quantum dots (also known as artificial atoms or nanocrystals) and one-dimensional quantum wires/tubes. The confinement of the electron wavefunctions in these low-dimensional structures has profound influences on their thermal, electronic, and optical properties.

Two-dimensional materials are important forms of nanomaterials and have the great potential to combine superior charge transport with optical properties. However, their development has relied on epitaxial growth of multilayer structures of different materials. This approach only allows limited selections of materials due to the lattice-matching requirement. Furthermore, because the interface between the two layers cannot be atomically sharp, the interface fluctuation can significantly alter the properties as the layer thickness approaches atomic level.

In 2004, an entirely new approach to make 2D materials was developed, and resulted in the discovery of graphene, which is a single layer of carbon atoms packed in a hexagonal lattice arrangement. This discovery was the topic of the 2010 Nobel Prize in Physics. In this approach, single atomic layers are separated from layered crystals through various techniques, and then installed on desired substrates. Due to its exceptional electronic, thermal, and mechanical properties, graphene is well-suited for a variety of applications in many industrial sectors.

Although graphene is a very good 2D material to investigate nonlinear optical effects, pristine graphene lacks a bandgap, a critical property for electronic devices. Following the discovery of graphene, other groups of layered materials like transition metal dichalcogenides and topological insulators have attracted significant attention. Unlike graphene, thin films of these materials be-

have like semiconductors with a large bandgap. As a result, TMDs and topological insulators are considered promising materials for electronic devices.

All of the materials and techniques discussed in this dissertation are expected to play important roles in the advancement of technology. Results presented on these materials show that the techniques used are not just limited to the particular properties of certain materials. These techniques can be extended to study various properties of a wide variety of materials.

Another research area in which new artificial 2D crystals developed by stacking different layered materials on top of each other has recently emerged from research related to these layered materials. It is quite easy to understand the basic principle to construct these heterostructures. For example, take thin films of different layered materials and put them on top of each other in a random fashion. The resulting stack will represent an artificial material assembled in a chosen sequence. It is a fast growing field and very little is known about the basic properties of assembled heterostructures. Since large numbers of layered material classes are present, there are many combinations possible to assemble as a heterostructure. Our aforementioned ultrafast techniques can be used to explore various properties of assembled heterostructures.

References

[1] N. Kumar, S. Najmaei, Q. Cui, F. Ceballos, P.M. Ajayan, J. Lou, and H. Zhao. Second harmonic microscopy of monolayer MoS_2. *Phys. Rev. B*, 87:161403(R), 2013.

[2] N. Kumar, J. Kumar, C. Gerstenkorn, R. Wang, H.Y. Chiu, A.L. Smirl, and H. Zhao. Third harmonic generation in graphene and graphite thin films. *Phys. Rev. B*, 87:121406(R), 2013.

[3] M. Fox. *Optical Properties of Solids*. Oxford University Press, New York, USA, first edition, 2001.

[4] N. Kumar, B.A. Ruzicka, N.P. Butch, P. Syers, K. Kirshenbaum, J. Paglione, and H. Zhao. Spatially resolved femtosecond pump-probe study of topological insulator Bi_2Se_3. *Phys. Rev. B*, 83:235306, 2011.

[5] N. Kumar, J. He, D. He, Y. Wang, and H. Zhao. Charge carrier dynamics in bulk MoS_2 crystal studied by transient absorption microscopy. *J. Appl. Phys.*, 113:133702, 2013.

[6] N. Kumar, Q. Cui, F. Ceballos, D. He, Y. Wang, and H. Zhao. Exciton-exciton annihilation in $MoSe_2$ monolayers. *Phys. Rev. B*, 89:125427, 2014.

[7] N. Kumar, Q. Cui, F. Ceballos, D. He, Y. Wang, and H. Zhao. Exciton diffusion in monolayer and bulk $MoSe_2$. *Nanoscale*, 6:4915, 2014.

[8] K. S. Novoselov, A. K. Geim, S. V. Morozov, D. Jiang, Y. Zhang, S. V. Dubonos, I. V. Grigorieva, and A. A. Firsov. Electric field effect in atomically thin carbon films. *Science*, 306:666, 2004.

[9] M. C. Lemme, T. J. Echtermeyer, M. Baus, and H. Kurz. A graphene field-effect device. *IEEE Electr. Device Lett.*, 28:282, 2007.

[10] M. T. Han, B. Özyilmaz, Y. B. Zhang, and P. Kim. Energy band-gap engineering of graphene nanoribbons. *Phys. Rev. Lett.*, 98:206805, 2007.

[11] Y. M. Lin, C. Dimitrakopoulos, K. A. Jenkins, D. B. Farmer, H. Y. Chiu, A. Grill, and P. Avouris. 100-GHz transistors from wafer-scale epitaxial graphene. *Science*, 327:662, 2010.

[12] C. Berger, Z. Song, X. Li, X. Wu, N. Brown, C. Naud, D. Mayou, T. Li, J. Hass, A. N. Marchenkov, E. H. Conrad, P. N. First, and W. A. de Heer. Electronic confinement and coherence in patterned epitaxial graphene. *Science*, 312:1191, 2006.

[13] B. A. Ruzicka, S. Wang, L. K. Werake, B. Weintrub, K. P. Loh, and H. Zhao. Hot carrier diffusion in graphene. *Phys. Rev. B*, 82:195414, 2010.

[14] F. Bonaccorso, Z. Sun, T. Hasan, and A. C. Ferrari. Graphene photonics and optoelectronics. *Nat. Photonics*, 4:611, 2010.

[15] R. W. Boyd. *Nonlinear Optics*. Academy Press, San Diego, USA, third edition, 2008.

[16] L. Liu, S. B. Kumar, Y. Ouyang, and J. Guo. Performance limits of monolayer transition metal dichalcogenide transistors. *IEEE Trans. on Electron Devices*, 58:3042, 2011.

[17] Y. Yoon, K. Ganapathi, and S. Salahuddin. How good can monolayer MoS_2 transistors be. *Nano Lett.*, 11:3768, 2011.

[18] Z. Yin, H. Li, H. Li, L. Jiang, Y. Shi, Y. Sun, G. Lu, Q. Zhang, X. Chen, and H. Zhang. Single-layer MoS_2 phototransistors. *ACS Nano*, 6:74–80, 2012.

[19] H. S. Lee, S. W. Min, Y. G. Chang, M. K. Park, T. Nam, H. Kim, J. H. Kim, S. Ryu, and S. Im. MoS_2 nanosheet phototransistors with thickness-modulated optical energy gap. *Nano Lett.*, 12:3695–3700, 2012.

[20] M. Shanmugam, T. Bansal, C. A. Durcan, and B. Yu. Molybdenum disulphide/titanium dioxide nanocomposite-poly 3-hexylthiophene bulk heterojunction solar cell. *Appl. Phys. Lett.*, 100:153901, 2012.

[21] K. F. Mak, K. He, C. Lee, G. H. Lee, J. Hone, T. F. Heinz, and J. Shan. Tightly bound trion in monolayer MoS_2. *Nat. Mater.*, 12:207–211, 2013.

[22] B. Shin, Y. Zhu, N. A. Bojarczuk, S. J. Chey, and S. Guha. Control of an interfacial $MpSe_2$ layer in $Cu_2ZnSnSe_4$ thin film solar cells: 8.9% power conversion efficiency with a tin diffusion barrier. *Appl. Phys. Lett.*, 101:053903, 2012.

[23] B. Shin, N. A. Bojarczuk, and S. Guha. On the kinetics of $MoSe_2$ interfacial layer formation in chalcogen-based thin film solar cells with a molybdenum back contact. *Appl. Phys. Lett.*, 102:091907, 2013.

[24] Y. F. Shi, C. X. Hua, B. Li, X. P. Fang, C. H. Yao, Y. C. Zhang, Y. S. Hu, Z. X. Wang, L. Q. Chen, D. Y. Zhao, and G. D. Stucky. Highly ordered mesoporous crystalline $MoSe_2$ material with efficient visible-light-driven photocatalytic activity and enhanced lithium storage performance. *Adv. Funct. Mater.*, 23:1832, 2013.

[25] S. Tongay, J. Zhou, C. Ataca, K. Lo, T. S. Matthews, J. B. Li, J. C. Grossman, and J. Q. Wu. Thermally driven crossover from indirect toward direct bandgap in 2D semiconductors: MoS_2 versus $MoSe_2$. *Nano Lett.*, 12:5576, 2012.

[26] S. Horzum, H. Sahin, S. Cahangirov, P. Cudazzo, A. Rubio, T. Serin, and F. M. Peeters. Phonon softening and direct to indirect band gap crossover in strained single-layer $MoSe_2$. *Phys. Rev. B*, 87:125415, 2013.

[27] A. K. Geim and I. V. Grigorieva. Van der waals heterostructures. *Nature*, 499:419, 2013.

[28] V. V. Gobre and A. Tkatchenko. Scaling laws for van der Waals interactions in nanostructured materials. *Nat. Commun.*, 4:2341, 2013.

[29] S. J. Haigh, A. Gholinia, R. Jalil, S. Romani, L. Britnell, D. C. Elias, K. S. Novoselov, L. A. Ponomarenko, A. K. Geim, and R. Gorbachev. Cross-sectional imaging of individual layers and buried interfaces of graphene-based heterostructures and superlattices. *Nat. Mater.*, 11:764, 2012.

[30] L. Britnell, R. M. Ribeiro, A. Eckmann, R. Jalil, B. D. Belle, A. Mishchenko, Y.-J. Kim, R. V. Gorbachev, T. Georgiou, S. V. Morozov, A. N. Grigorenko, A. K. Geim, C. Casiraghi, A. H. C. Neto, and K. S. Novoselov. Strong light-matter interactions in heterostructures of atomically thin films. *Science*, 340:1311, 2013.

[31] T. Georgiou, R. Jalil, B. D. Belle, L. Britnell, R. V. Gorbachev, S. V. Morozov, Y. J. Kim, A. Gholinia, S. J. Haigh, O. Makarovsky, L. Eaves, L. A. Ponomarenko, A. K. Geim, K. S. Novoselov, and A. Mishchenko. Vertical field-effect transistor based on graphene-WS_2 heterostructures for flexible and transparent electronics. *Nat. Nanotechnol.*, 8:100, 2013.

[32] L. Britnell, R. V. Gorbachev, R. Jalil, B. D. Belle, F. Schedin, A. Mishchenko, T. Georgiou, M. I. Katsnelson, L. Eaves, S. V. Morozov, N. M. R. Peres, J. Leist, A. K. Geim, K. S. Novoselov, and L. A. Ponomarenko. Field-effect tunneling transistor based on vertical graphene heterostructures. *Science*, 335:947, 2012.

[33] M. S. Choi, G. H. Lee, Y. J. Yu, D. Y. Lee, S. H. Lee, P. Kim, J. Hone, and W. J. Yoo. Controlled charge trapping by molybdenum disulphide and graphene in ultrathin heterostructured memory devices. *Nat. Commun.*, 4:1624, 2013.

[34] D. Xiao, G. B. Liu, W. Feng, X. Xu, and W. Yao. Coupled spin and valley physics in monolayers of MoS_2 and other group-VI dichalcogenides. *Phys. Rev. Lett.*, 108:196802, 2012.

[35] T. Cao, G. Wang, W. P. Han, H. Q. Ye, C. R. Zhu, J. R. Shi, Q. Niu, P. H. Tan, E. Wang, B. L. Liu, and J. Feng. Valley-selective circular dichroism of monolayer molybdenum disulphide. *Nat. Commun.*, 3:887, 2012.

[36] Z. Gong, G.-B. Liu, H. Yu, D. Xiao, X. Cui, X. Xu, and W. Yao. Magnetoelectric effects and valley-controlled spin quantum gates in transition metal dichalcogenide bilayers. *Nat. Commun.*, 4:2053, 2013.

[37] S. A. Wolf, D. D. Awschalom, R. A. Buhrman, J. M. Daughton, S. von Molnar, M. L. Roukes, A. Y. Chtchelkanova, and D. M. Treger. Spintronics: A spin-based electronics vision for the future. *Science*, 294:1488, 2001.

[38] I. Žutić, J. Fabian, and S. Das Sarma. Spintronics: Fundamentals and applications. *Rev. Mod. Phys.*, 76:323, 2004.

[39] S. Datta and B. Das. Electronic analog of the electro-optic modulator. *Appl. Phys. Lett.*, 56:665, 1990.

[40] J. Isberg, M. Gabrysch, J. Hammersberg, S. Majdi, K. K. Kovi, and D. J. Twitchen. Generation, transport and detection of valley-polarized electrons in diamond. *Nat. Mater.*, 12:760, 2013.

[41] C. L. Kane and E. J. Mele. A new spin on the insulating state. *Science*, 314:1692, 2006.

[42] J. E. Moore. The quantum spin Hall effect and topological insulators. *Nat. Phys.*, 5:378, 2009.

[43] J. E. Moore. The birth of topological insulators. *Nature*, 464:194, 2010.

[44] X. L. Qi and S. C. Zhang. The quantum spin Hall effect and topological insulators. *Phys. Today*, 63:33, 2010.

[45] C. L. Kane and E. J. Mele. Z_2 topological order and the quantum spin Hall effect. *Phys. Rev. Lett.*, 95:146802, 2005.

[46] M. König, S. Wiedmann, C. Bruene, A. Roth, H. Buhmann, L. W. Molenkamp, X.-L. Qi, and S.-C. Zhang. Quantum spin Hall insulator state in HgTe quantum wells. 318:766, 2007.

[47] L. Fu and C. L. Kane. Topological insulators with inversion symmetry. *Phys. Rev. B*, 76:045302, 2007.

[48] H. Zhang, C. X. Liu, X. L. Qi, X. Dai, Z. Fang, and S. C. Zhang. Topological insulators in Bi_2Se_3, Bi_2Te_3 and Sb_2Te_3 with a single Dirac cone on the surface. *Nat. Phys.*, 5:438, 2009.

[49] Y. Xia, D. Qian, D. Hsieh, L. Wray, A. Pal, H. Lin, A. Bansil, D. Grauer, Y. S. Hor, R. J. Cava, and M. Z. Hasan. Observation of a large-gap topological-insulator class with a single Dirac cone on the surface. *Nat. Phys.*, 5:398, 2009.

[50] D. Hsieh, D. Qian, L. Wray, Y. Xia, Y. S. Hor, R. J. Cava, and M. Z. Hasan. A topological Dirac insulator in a quantum spin Hall phase. *Nature*, 452:970, 2008.

[51] Y. L. Chen, J. G. Analytis, J.-H. Chu, Z. K. Liu, S.-K. Mo, X. L. Qi, H. J. Zhang, D. H. Lu, X. Dai, Z. Fang, S. C. Zhang, I. R. Fisher, Z. Hussain, and Z.-X. Shen. Experimental realization of a three-dimensional topological insulator, Bi_2Te_3. *Science*, 325:178, 2009.

[52] Q. H. Wang, K. Kalantar-Zadeh, A. Kis, J. N. Coleman, and M. S. Strano. Electronics and optoelectronics of two-dimensional transition metal dichalcogenides. *Nat. Nanotechnol.*, 7:699, 2012.

[53] K. F. Mak, C. Lee, J. Hone, J. Shan, and T. F. Heinz. Atomically thin mos_2: A new direct-gap semiconductor. *Phys. Rev. Lett.*, 105:136805, 2010.

[54] A. Splendiani, L. Sun, Y. Zhang, T. Li, J. Kim, C. Y. Chim, G. Galli, and F. Wang. Emerging photoluminescence in monolayer MoS_2. *Nano Lett.*, 10:1271–1275, 2010.

[55] A. Kuc, N. Zibouche, and T. Heine. Influence of quantum confinement on the electronic structure of the transition metal sulfide TS_2. *Phys. Rev. B*, 83:245213, 2011.

[56] B. Radisavljevic, A. Radenovic, J. Brivio, V. Giacometti, and A. Kis. Single-layer MoS_2 transistors. *Nat. Nanotechnol.*, 6:147–150, 2011.

[57] B. Radisavljevic, M. B. Whitwick, and A. Kis. Integrated circuits and logic operations based on single-layer MoS_2. *ACS Nano*, 5:9934–9938, 2011.

[58] H. Wang, L. L. Yu, Y. H. Lee, Y. M. Shi, A. Hsu, M. L. Chin, L. J. Li, M. Dubey, J. Kong, and T. Palacios. Integrated circuits based on bilayer MoS_2 transistors. *Nano Lett.*, 12:4674–4680, 2012.

[59] Y. Zhang, J. Ye, Y. Matsuhashi, and Y. Iwasa. Ambipolar MoS_2 thin flake transistors. *Nano Lett.*, 12:1136–1140, 2012.

[60] S. Bertolazzi, J. Brivio, and A. Kis. Stretching and breaking of ultrathin MoS_2. *ACS Nano*, 5:9703–9709, 2011.

[61] Q. Y. He, Z. Y. Zeng, Z. Y. Yin, H. Li, S. X. Wu, X. Huang, and H. Zhang. Fabrication of flexible MoS_2 thin-film transistor arrays for practical gas-sensing applications. *Small*, 8:2994–2999, 2012.

[62] J. Pu, Y. Yomogida, K. K. Liu, L. J. Li, Y. Iwasa, and T. Takenobu. Highly flexible MoS_2 thin-film transistors with ion gel dielectrics. *Nano Lett.*, 12:4013–4017, 2012.

[63] M. M. Benameur, B. Radisavljevic, J. S. Héron, S. Sahoo, H. Berger, and A. Kis. Visibility of dichalcogenide nanolayers. *Nanotechnology*, 22:125706, 2011.

[64] H. Li, G. Lu, Z. Y. Yin, Q. Y. He, H. Li, Q. Zhang, and H. Zhang. Optical identification of single- and few-layer MoS_2 sheets. *Small*, 8:682, 2012.

[65] A Castellanos-Gomez, N. Agraït, and G Rubio-Bollinger. Optical identification of atomically thin dichalcogenide crystals. *Appl. Phys. Lett.*, 96:213116, 2010.

[66] C. Lee, H. Yan, L. E. Brus, T. F. Heinz, J. Hone, and S. Ryu. Anomalous lattice vibrations of single- and few-layer MoS_2. *ACS Nano*, 4:2695, 2010.

[67] A. Molina-Sanchez and L. Wirtz. Phonons in single-layer and few-layer MoS_2 and WS_2. *Phys. Rev. B*, 84:155413, 2011.

[68] K. S. Novoselov, D. Jiang, F. Schedin, T. J. Booth, V. V. Khotkevich, S. V. Morozov, and A. K. Geim. Two-dimensional atomic crystals. *Proc. Natl. Acad. Sci. U.S.A.*, 102:10451–10453, 2005.

[69] G. Eda, H. Yamaguchi, D. Voiry, T. Fujita, M. Chen, and M. Chhowalla. Photoluminescence from chemically exfoliated MoS_2. *Nano Lett.*, 11:5111–5116, 2011.

[70] Z. Y. Zeng, Z. Y. Yin, X. Huang, H. Li, Q. Y. He, G. Lu, F. Boey, and H. Zhang. Single-layer semiconducting nanosheets: High-yield preparation and device fabrication. *Angew. Chem.-Int. Edit.*, 50:11093, 2011.

[71] M. B. Dines. Lithium intercalation via n-butyllithium of the layered transition metal dichalcogenides. *Mater. Res. Bul.*, 10:287, 1975.

[72] G. L. Frey, K. J. Reynolds, R. H. Friend, H. Cohen, and Y. Feldman. Solution-processed anodes from layer-structure materials for high-efficiency polymer light-emitting diodes. *J. Am. Chem. Soc.*, 125:5998, 2003.

[73] Z. Y. Zeng, T. Sun, J. X. Zhu, X. Huang, Z. Y. Yin, G. Lu, Z. X. Fan, Q. Y. Yan, H. H. Hng, and H. Zhang. An effective method for the fabrication of few-layer-thick inorganic nanosheets. *Angew. Chem.-Int. Edit.*, 51:9052, 2012.

[74] J. N. Coleman, M. Lotya, A. O'neill, S. D. Bergin, P. J. King, U. Khan, K. Young, A. Gaucher, S. De, R. J. Smith, I. V. Shvets, S. K. Arora, G. Stanton, H.-Y. Kim, K. Lee, G. T. Kim, G. S. Duesberg, T. Hallam, J. J. Boland, J. J. Wang, J. F. Donegan, J. C. Grunlan, G. Moriarty, A. Shmeliov, R. J. Nicholls, J. M. Perkins, E. M. Grieveson, K. Theuwissen, D. W. McComb, P. D. Nellist, and V. Nicolosi. Two-dimensional nanosheets produced by liquid exfoliation of layered materials. *Science*, 331:568, 2011.

[75] R. J. Smith, P. J. King, M. Lotya, C. Wirtz, U. Khan, S. De, A. O'Neill, G. S. Duesberg, J. C. Grunlan, G. Moriarty, J. Chen, J. Z. Wang, A. I. Minett, V. Nicolosi, and J. N. Coleman.

Large-scale exfoliation of inorganic layered compounds in aqueous surfactant solutions. *Adv. Mater.*, 23:3944, 2011.

[76] P. May, U. Khan, J. M. Hughes, and J. N. Coleman. Role of solubility parameters in understanding the steric stabilization of exfoliated two-dimensional nanosheets by adsorbed polymers. *J. Phys. Chem. C*, 116:11393, 2012.

[77] K.-G. Zhou, N.-N. Mao, H.-X. Wang, Y. Peng, and H.-L. Zhang. A mixed-solvent strategy for efficient exfoliation of inorganic graphene analogues. *Angew. Chem. Int. Ed.*, 50:10839, 2011.

[78] G. Cunningham, M. Lotya, C. S. Cucinotta, S. Sanvito, S. D. Bergin, R. Menzel, M. S. P. Shaffer, and J. N. Coleman. Solvent exfoliation of transition metal dichalcogenides: Dispersibility of exfoliated nanosheets varies only weakly between compounds. *ACS Nano*, 6:3468, 2012.

[79] C. Altavilla, M. Sarno, and P. Ciambelli. A novel wet chemistry approach for the synthesis of hybrid 2D free-floating single or multilayer nanosheets of MS_2 (M=Mo, W). *Chem. Mate.*, 23:3879, 2011.

[80] A. O'neill, U. Khan, and J. N. Coleman. Preparation of high concentration dispersions of exfoliated MoS_2 with increased flake size. *Chem. Mater.*, 24:2414, 2012.

[81] Y. Y. Peng, Z. Y. Meng, C. Zhong, J. Lu, W. C. Yu, Z. P. Yang, and Y. T. Qian. Hydrothermal synthesis of MoS_2 and its pressure-related crystallization. *J. Solid. State. Chem.*, 159:170, 2001.

[82] Y. Y. Peng, Z. Y. Meng, C. Zhong, J. Lu, W. C. Yu, Y. B. Jia, and Y. T. Qian. Hydrothermal synthesis and characterization of single-molecular-layer MoS_2 and $MoSe_2$. *Chem. Lett.*, 30:772, 2001.

[83] Y. H. Lee, X. Q. Zhang, W. Zhang, M. T. Chang, C. T. Lin, K. D. Chang, Y. C. Yu, J. T. Wang, C. S. Chang, L. J. Li, and T. W. Lin. Synthesis of large-area MoS_2 atomic layers with chemical vapor deposition. *Adv. Mater.*, 24:2320, 2012.

[84] Y. J. Zhan, Z. Liu, S. Najmaei, P. M. Ajayan, and J. Lou. Large-area vapor-phase growth and characterization of MoS_2 atomic layers on a SiO_2 substrate. *Small*, 8:966, 2012.

[85] K. K. Liu, W. Zhang, Y. H. Lee, Y. C. Lin, M. T. Chang, C. Y. Su, C. S. Chang, H. Li, Y. Shi, H. Zhang, C. S. Lai, and L. J. Li. Growth of large-area and highly crystalline MoS_2 thin layers on insulating substrates. *Nano Lett.*, 12:1538, 2012.

[86] S. Balendhran, J. Z. Ou, M. Bhaskaran, S. Sriram, S. Ippolito, Z. Vasic, E. Kats, S. Bhargava, S. Zhuiykov, and K. Kalantar-Zadeh. Atomically thin layers of MoS_2 via a two step thermal evaporation-exfoliation method. *Nanoscale*, 4:461, 2012.

[87] Y. M. Shi, W. Zhou, A. Y. Lu, W. J. Fang, Y. H. Lee, A. L. Hsu, S. M. Kim, K. K. Kim, H. Y. Yang, L. J. Li, J. C. Idrobo, and J. Kong. Van der waals epitaxy of MoS_2 layers using graphene as growth templates. *Nano Lett.*, 12:2784, 2012.

[88] S. Najmaei, Z. Liu, W. Zhou, X. Zou, G. Shi, S. Lei, B. I. Yakobson, J.-C. Idrobo, P. M. Ajayan, and J. Lou. Vapor Phase Growth and Grain Boundary Structure of Molybdenum Disulfide Atomic Layers. *ArXiv e-prints*, 2013.

[89] J. V. Lauritsen, J. Kibsgaard, S. Helveg, H. Topsoe, B. S. Clausen, E. Laegsgaard, and F. Besenbacher. Size-dependent structure of MoS_2 nanocrystals. *Nat. Nanotechnol.*, 2:53, 2007.

[90] LineS. Byskov, JensK. Nørskov, BjerneS. Clausen, and Henrik Topsøe. Edge termination of MoS_2 and CoMoS catalyst particles. *Catalysis Letters*, 64:95–99, 2000.

[91] L. M. Malard, T. V. Alencar, A. P. M. Barboza, K. F. Mak, and A. M. de Paula. Observation of intense second harmonic generation from mos_2 atomic crystals. *Phys. Rev. B*, 87:201401(R), 2013.

[92] H. Zeng, G.-B. Liu, J. Dai, Y. Yan, B. Zhu, R. He, L. Xie, S. Xu, X. Chen, W. Yao, and X. Cui. Optical signature of symmetry variations and spin-valley coupling in atomically thin tungsten dichalcogenides. *Sci Rep.*, 3:1608, 2013.

[93] Y. Li, Y. Rao, K. F. Mak, Y. You, S. Wang, C. R. Dean, , and T. F. Heinz. Probing symmetry properties of few-layer mos_2 and h-bn by optical second-harmonic generation. *Nano Lett.*, 13:3329, 2013.

[94] X. Yin, Z. Ye, D. A. Chenet, Y. Ye, K. O'Brien, J. C. Hone, and X. Zhang. Edge nonlinear optics on a mos_2 atomic monolayer. *Science*, 344:488, 2014.

[95] P. R. Wallace. The band theory of graphite. *Phys. Rev.*, 71:622, 1947.

[96] K. S. Novoselov, A. K. Geim, S. V. Morozov, D. Jiang, M. I. Katsnelson, I. V. Grigorieva, S. V. Dubonos, and A. A. Firsov. Two-dimensional gas of massless Dirac fermions in graphene. *Nature*, 438:197, 2005.

[97] A. H. Castro Neto, F. Guinea, N. M. R. Peres, K. S. Novoselov, and A. K. Geim. The electronic properties of graphene. *Rev. Mod. Phys.*, 81:109–162, 2009.

[98] K. S. Kim, Y. Zhao, H. Jang, S. Y. Lee, J. M. Kim, K. S. Kim, J. H. Ahn, P. Kim, J. Y. Choi, and B. H. Hong. Large-scale pattern growth of graphene films for stretchable transparent electrodes. *Nature*, 457:706, 2009.

[99] S. Bae, H. Kim, Y. Lee, X. F. Xu, J. S. Park, Y. Zheng, J. Balakrishnan, T. Lei, H. R. Kim, Y. I. Song, Y. J. Kim, K. S. Kim, B. Ozyilmaz, J. H. Ahn, B. H. Hong, and S. Iijima. Roll-to-roll production of 30-inch graphene films for transparent electrodes. *Nat. Nanotechnol.*, 5:574, 2010.

[100] S. Gilje, S. Han, M. Wang, K. L. Wang, and R. B. Kaner. A chemical route to graphene for device applications. *Nano Lett.*, 7:3394, 2007.

[101] H. A. Becerril, J. Mao, Z. Liu, R. M. Stoltenberg, Z. Bao, and Y. Chen. Evaluation of solution-processed reduced graphene oxide films as transparent conductors. *ACS Nano*, 2:463, 2008.

[102] X. Wang, L. J. Zhi, and K. Mullen. Transparent, conductive graphene electrodes for dye-sensitized solar cells. *Nano Lett.*, 8:323, 2008.

[103] H. Park, P. R. Brown, V. Buloyic, and J. Kong. Graphene as transparent conducting electrodes in organic photovoltaics: Studies in graphene morphology, hole transporting layers, and counter electrodes. *Nano Lett.*, 12:133, 2012.

[104] F. N. Xia, T. Mueller, R. Golizadeh-Mojarad, M. Freitag, Y. M. Lin, J. Tsang, V. Perebeinos, and P. Avouris. Photocurrent imaging and efficient photon detection in a graphene transistor. *Nano Lett.*, 9:1039, 2009.

[105] F. N. Xia, T. Mueller, Y. M. Lin, A. Valdes-Garcia, and P. Avouris. Ultrafast graphene photodetector. *Nat. Nanotechnol.*, 4:839, 2009.

[106] T. Mueller, F. N. A. Xia, and P. Avouris. Graphene photodetectors for high-speed optical communications. *Nat. Photonics*, 4:297, 2010.

[107] N. M. Gabor, J. C. W. Song, Q. Ma, N. L. Nair, T. Taychatanapat, K. Watanabe, T. Taniguchi, L. S. Levitov, and P. Jarillo-Herrero. Hot carrier-assisted intrinsic photoresponse in graphene. *Science*, 334:648, 2011.

[108] M. C. Lemme, F. H. L. Koppens, A. L. Falk, M. S. Rudner, H. Park, L. S. Levitov, and C. M. Marcus. Gate-activated photoresponse in a graphene p-n junction. *Nano Lett.*, 11:4134, 2011.

[109] A. Urich, K. Unterrainer, and T. Mueller. Intrinsic response time of graphene photodetectors. *Nano Lett.*, 11:2804, 2011.

[110] D. Sun, G. Aivazian, A. M. Jones, J. S. Ross, W. Yao, D. Cobden, and X. D. Xu. Ultrafast hot-carrier-dominated photocurrent in graphene. *Nat. Nanotechnol.*, 7:114, 2012.

[111] M. Liu, X. B. Yin, E. Ulin-Avila, B. S. Geng, T. Zentgraf, L. Ju, F. Wang, and X. Zhang. A graphene-based broadband optical modulator. *Nature*, 474:64, 2011.

[112] M. Liu, X. B. Yin, and X. Zhang. Double-layer graphene optical modulator. *Nano Lett.*, 12:1482, 2012.

[113] L. Ju, B. S. Geng, J. Horng, C. Girit, M. Martin, Z. Hao, H. A. Bechtel, X. G. Liang, A. Zettl, Y. R. Shen, and F. Wang. Graphene plasmonics for tunable terahertz metamaterials. *Nat. Nanotechnol.*, 6:630, 2011.

[114] F. H. L. Koppens, D. E. Chang, and F. J. G. de Abajo. Graphene plasmonics: A platform for strong light-matter interactions. *Nano Lett.*, 11:3370, 2011.

[115] S. F. Shi, X. D. Xu, D. C. Ralph, and P. L. McEuen. Plasmon resonance in individual nanogap electrodes studied using graphene nanoconstrictions as photodetectors. *Nano Lett.*, 11:1814, 2011.

[116] A. Vakil and N. Engheta. Transformation optics using graphene. *Science*, 332:1291, 2011.

[117] P. Tassin, T. Koschny, M. Kafesaki, and C. M. Soukoulis. A comparison of graphene, superconductors and metals as conductors for metamaterials and plasmonics. *Nat. Photonics*, 6:259, 2012.

[118] W. Zhou, J. Lee, J. Nanda, S. T. Pantelides, S. J. Pennycook, and J. C. Idrobo. Atomically localized plasmon enhancement in monolayer graphene. *Nat. Nanotechnol.*, 7:161, 2012.

[119] Q. L. Bao, H. Zhang, B. Wang, Z. H. Ni, Chyx Lim, Y. Wang, D. Y. Tang, and K. P. Loh. Broadband graphene polarizer. *Nat. Photonics*, 5:411, 2011.

[120] I. Crassee, J. Levallois, A. L. Walter, M. Ostler, A. Bostwick, E. Rotenberg, T. Seyller, D. van der Marel, and A. B. Kuzmenko. Giant faraday rotation in single- and multilayer graphene. *Nat. Phys.*, 7:48, 2011.

[121] M. M. Glazov. Second harmonic generation in graphene. *JETP Lett.*, 93:366, 2011.

[122] S. A. Mikhailov. Theory of the giant plasmon-enhanced second-harmonic generation in graphene and semiconductor two-dimensional electron systems. *Phys. Rev. B*, 84:045432, 2011.

[123] S. F. Wu, L. Mao, A. M. Jones, W. Yao, C. W. Zhang, and X. D. Xu. Quantum-enhanced tunable second-order optical nonlinearity in bilayer graphene. *Nano Lett.*, 12:2032, 2012.

[124] J. J. Dean and H. M. van Driel. Second harmonic generation from graphene and graphitic films. *Appl. Phys. Lett.*, 95:261910, 2009.

[125] J. J. Dean and H. M. van Driel. Graphene and few-layer graphite probed by second-harmonic generation: Theory and experiment. *Phys. Rev. B*, 82:125411, 2010.

[126] H. Z. Yang, X. B. Feng, Q. Wang, H. Huang, W. Chen, A. T. S. Wee, and W. Ji. Giant two-photon absorption in bilayer graphene. *Nano Lett.*, 11:2622–2627, 2011.

[127] D. Sun, C. Divin, J. Rioux, J. E. Sipe, C. Berger, W. A. de Heer, P. N. First, and T. B. Norris. Coherent control of ballistic photocurrents in multilayer epitaxial graphene using quantum interference. *Nano. Lett.*, 10:1293, 2010.

[128] E. Hendry, P. J. Hale, J. Moger, A. K. Savchenko, and S. A. Mikhailov. Coherent nonlinear optical response of graphene. *Phys. Rev. Lett.*, 105:097401, 2010.

[129] Z. S. Yang, N. H. Kwong, R. Binder, and Arthur L. Smirl. Stopping, storing, and releasing light in quantum-well bragg structures. *J. Opt. Soc. Am. B*, 22:2144, 2005.

[130] R. Wu, Y. L. Zhang, S. C. Yan, F. Bian, W. L. Wang, X. D. Bai, X. H. Lu, J. M. Zhao, and E. G. Wang. Purely coherent nonlinear optical response in solution dispersions of graphene sheets. *Nano Lett.*, 11:5159–5164, 2011.

[131] S. A. Mikhailov. Theory of the nonlinear optical frequency mixing effect in graphene. *Physica E*, 44:924, 2012.

[132] S. Schmitt-Rink, D. S. Chemla, and D. A. B. Miller. Theory of transient excitonic optical nonlinearities in semiconductor quantum-well structures. *Phys. Rev. B*, 32:6601, 1985.

[133] L. K. Werake, B. A. Ruzicka, and H. Zhao. Observation of intrinsic inverse spin Hall effect. *Phys. Rev. Lett.*, 106:107205, 2011.

[134] B. A. Ruzicka and H. Zhao. Power dependence of pure spin current injection by quantum interference. *Phys. Rev. B*, 79:155204, 2009.

[135] H. Zhao, M. Mower, and G. Vignale. Ambipolar spin diffusion and D'yakonov-Perel' spin relaxation in GaAs quantum wells. *Phys. Rev. B*, 79:115321, 2009.

[136] B. A. Ruzicka, K. Higley, L. K. Werake, and H. Zhao. All-optical generation and detection of subpicosecond ac spin-current pulses in GaAs. *Phys. Rev. B*, 78:045314, 2008.

[137] H. Zhao, E. J. Loren, H. M. van Driel, and A. L. Smirl. Coherence control of Hall charge and spin currents. *Phys. Rev. Lett.*, 96:246601, 2006.

[138] H. Zhao, A. L. Smirl, and H. M. van Driel. Temporally and spatially resolved ballistic pure spin transport. *Phys. Rev. B*, 75:075305, 2007.

[139] H. Zhao, E. J. Loren, A. L. Smirl, and H. M. van Driel. Dynamics of charge current injected in GaAs by quantum interference. *J. Appl. Phys.*, 103:053510, 2008.

[140] J. Maciejko, X. L. Qi, H. D. Drew, and S. C. Zhang. Topological quantization in units of the fine structure constant. *Phys. Rev. Lett.*, 105:166803, 2010.

[141] W. K. Tse and A. H. Macdonald. Magneto-optical and magnetoelectric effects of topological insulators in quantizing magnetic fields. *Phys. Rev. B*, 82:161104, 2010.

[142] W. K. Tse and A. H. Macdonald. Giant magneto-optical Kerr effect and universal Faraday effect in thin-film topological insulators. *Phys. Rev. Lett.*, 105:057401, 2010.

[143] P. Hosur. Circular photogalvanic effect on topological insulator surfaces: Berry-curvature-dependent response. *Phys. Rev. B*, 83:035309, 2011.

[144] N. P. Butch, K. Kirshenbaum, P. Syers, A. B. Sushkov, G. S. Jenkins, H. D. Drew, and J. Paglione. Strong surface scattering in ultrahigh-mobility Bi_2Se_3 topological insulator crystals. *Phys. Rev. B*, 81:241301, 2010.

[145] A. D. Laforge, A. Frenzel, B. C. Pursley, T. Lin, X. F. Liu, J. Shi, and D. N. Basov. Optical characterization of Bi_2Se_3 in a magnetic field: Infrared evidence for magnetoelectric coupling in a topological insulator material. *Phys. Rev. B*, 81:125120, 2010.

[146] G. S. Jenkins, A. B. Sushkov, D. C. Schmadel, N. P. Butch, P. Syers, J. Paglione, and H. D. Drew. Terahertz Kerr and reflectivity measurements on the topological insulator Bi_2Se_3. *Phys. Rev. B*, 82:125120, 2010.

[147] A. B. Sushkov, G. S. Jenkins, D. C. Schmadel, N. P. Butch, J. Paglione, and H. D. Drew. Far-infrared cyclotron resonance and Faraday effect in Bi_2Se_3. *Phys. Rev. B*, 82:125110, 2010.

[148] D. Hsieh, J. W. Mciver, D. H. Torchinsky, D. R. Gardner, Y. S. Lee, and N. Gedik. Nonlinear optical probe of tunable surface electrons on a topological insulator. *Phys. Rev. Lett.*, 106:057401, 2011.

[149] J. Qi, X. Chen, W. Yu, P. Cadden-Zimansky, D. Smirnov, N. H. Tolk, I. Miotkowski, H. Cao, Y. P. Chen, Y. Wu, S. Qiao, and Z. Jiang. Ultrafast carrier and phonon dynamics in Bi_2Se_3 crystals. *Appl. Phys. Lett.*, 97:182102, 2010.

[150] C. Thomsen, J. Strait, Z. Vardeny, H. J. Maris, J. Tauc, and J. J. Hauser. Coherent phonon generation and detection by picosecond light-pulses. *Phys. Rev. Lett.*, 53:989, 1984.

[151] C. Thomsen, H. T. Grahn, H. J. Maris, and J. Tauc. Surface generation and detection of phonons by picosecond light-pulses. *Phys. Rev. B*, 34:4129, 1986.

[152] O. Matsuda, T. Tachizaki, T. Fukui, J. J. Baumberg, and O. B. Wright. Acoustic phonon generation and detection in gaas/al0.3ga0.7as quantum wells with picosecond laser pulses. *Phys. Rev. B*, 71:115330, 2005.

[153] Y. C. Wen, L. C. Chou, H. H. Lin, V. Gusev, K. H. Lin, and C. K. Sun. Efficient generation of coherent acoustic phonons in (111) ingaas/gaas multiple quantum wells through piezoelectric effects. *Appl. Phys. Lett.*, 90:172102, 2007.

[154] P. Babilotte, P. Ruello, D. Mounier, T. Pezeril, G. Vaudel, M. Edely, J. M. Breteau, V. Gusev, and K. Blary. Femtosecond laser generation and detection of high-frequency acoustic phonons in gaas semiconductors. *Phys. Rev. B*, 81:245207, 2010.

[155] A. V. Akimov, A. V. Scherbakov, D. R. Yakovlev, C. T. Foxon, and M. Bayer. Ultrafast band-gap shift induced by a strain pulse in semiconductor heterostructures. *Phys. Rev. Lett.*, 97:037401, 2006.

[156] J. K. Miller, J. Qi, Y. Xu, Y. J. Cho, X. Liu, J. K. Furdyna, I. Perakis, T. V. Shahbazyan, and N. Tolk. Near-bandgap wavelength dependence of long-lived traveling coherent longitudinal acoustic phonons in gasb-gaas heterostructures. *Phys. Rev. B*, 74:113313, 2006.

[157] S. Wu, P. Geiser, J. Jun, J. Karpinski, and R. Sobolewski. Femtosecond optical generation and detection of coherent acoustic phonons in gan single crystals. *Phys. Rev. B*, 76:085210, 2007.

[158] R. L. Liu, G. D. Sanders, C. J. Stanton, C. S. Kim, J. S. Yahng, Y. D. Jho, K. J. Yee, E. Oh, and D. S. Kim. Femtosecond pump-probe spectroscopy of propagating coherent acoustic phonons in inxga1-xn/gan heterostructures. *Phys. Rev. B*, 72:195335, 2005.

[159] O. B. Wright. Thickness and sound-velocity measurement in thin transparent films with laser picosecond acoustics. *J. Appl. Phys.*, 71:1617, 1992.

[160] P. J. S. Van Capel and J. I. Dijkhuis. Optical generation and detection of shock waves in sapphire at room temperature. *Appl. Phys. Lett.*, 88:151910, 2006.

[161] P. Ruello, S. Zhang, P. Laffez, B. Perrin, and V. Gusev. Laser-induced coherent acoustical phonons mechanisms in the metal-insulator transition compound ndnio3: Thermal and nonthermal processes. *Phys. Rev. B*, 79:094303, 2009.

[162] D. Lim, V. K. Thorsmolle, R. D. Averitt, Q. X. Jia, K. H. Ahn, M. J. Graf, S. A. Trugman, and A. J. Taylor. Coherent optical and acoustic phonon generation correlated with the charge-ordering phase transition in la1-xcaxmno3. *Phys. Rev. B*, 71:134403, 2005.

[163] J. Wang, Y. Hashimoto, J. Kono, A. Oiwa, H. Munekata, G. D. Sanders, and C. J. Stanton. Propagating coherent acoustic phonon wave packets in inxmn1-xas/gasb. *Phys. Rev. B*, 72:153311, 2005.

[164] D. Wang, A. Cross, G. Guarino, S. Wu, and R. Sobolewski. Time-resolved dynamics of coherent acoustic phonons in cdmnte diluted-magnetic single crystals. *Appl. Phys. Lett.*, 90:211905, 2007.

[165] J. Qi, J. A. Yan, H. Park, A. Steigerwald, Y. Xu, S. N. Gilbert, X. Liu, J. K. Furdyna, S. T. Pantelides, and N. Tolk. Mechanical and electronic properties of ferromagnetic ga1-xmnxas using ultrafast coherent acoustic phonons. *Phys. Rev. B*, 81:115208, 2010.

[166] O. B. Wright. Ultrafast nonequilibrium stress generation in gold and silver. *Phys. Rev. B*, 49:9985, 1994.

[167] A. Vertikov, M. Kuball, A. V. Nurmikko, and H. J. Maris. Time-resolved pump-probe experiments with subwavelength lateral resolution. *Appl. Phys. Lett.*, 69:2465, 1996.

[168] H. Y. Hao and H. J. Maris. Study of phonon dispersion in silicon and germanium at long wavelengths using picosecond ultrasonics. *Phys. Rev. Lett.*, 84:5556, 2000.

[169] B. C. Daly, T. B. Norris, J. Chen, and J. B. Khurgin. Picosecond acoustic phonon pulse propagation in silicon. *Phys. Rev. B*, 70:214307, 2004.

[170] A. Devos, F. Poinsotte, J. Groenen, O. Dehaese, N. Bertru, and A. Ponchet. Strong generation of coherent acoustic phonons in semiconductor quantum dots. *Phys. Rev. Lett.*, 98:207402, 2007.

[171] A. Yamamoto, T. Mishina, Y. Masumoto, and M. Nakayama. Coherent oscillation of zone-folded phonon modes in gaas-alas superlattices. *Phys. Rev. Lett.*, 73:740, 1994.

[172] R. N. Kini, A. J. Kent, N. M. Stanton, and M. Henini. Generation and detection of terahertz coherent transverse-polarized acoustic phonons by ultrafast optical excitation of gaas/alas superlattices. *Appl. Phys. Lett.*, 88:134112, 2006.

[173] P. Walker, R. P. Campion, A. J. Kent, D. Lehmann, and C. Jasiukiewicz. Excitation and detection of high-frequency coherent acoustic phonons in low-symmetry superlattices. *Phys. Rev. B*, 78:233307, 2008.

[174] M. F. Pascual Winter, A. Fainstein, B. Jusserand, B. Perrin, and A. Lemaitre. Optimized optical generation and detection of superlattice acoustic phonons. *Appl. Phys. Lett.*, 94:103103, 2009.

[175] R. Beardsley, A. V. Akimov, B. A. Glavin, W. Maryam, M. Henini, and A. J. Kent. Optical detection of folded mini-zone-edge coherent acoustic modes in a doped gaas/alas superlattice. *Phys. Rev. B*, 82:041302, 2010.

[176] G. Cerullo, S. De Silvestri, and U. Banin. Size-dependent dynamics of coherent acoustic phonons in nanocrystal quantum dots. *Phys. Rev. B*, 60:1928, 1999.

[177] M. Ikezawa, T. Okuno, Y. Masumoto, and A. A. Lipovskii. Complementary detection of confined acoustic phonons in quantum dots by coherent phonon measurement and raman scattering. *Phys. Rev. B*, 64:201315, 2001.

[178] A. V. Bragas, C. Aku-Leh, S. Costantino, A. Ingale, J. Zhao, and R. Merlin. Ultrafast optical generation of coherent phonons in cdte1-xsex quantum dots. *Phys. Rev. B*, 69:205306, 2004.

[179] Y. K. Huang, G. W. Chern, C. K. Sun, Y. Smorchkova, S. Keller, U. Mishra, and S. P. Denbaars. Generation of coherent acoustic phonons in strained gan thin films. *Appl. Phys. Lett.*, 79:3361, 2001.

[180] G. W. Chern, K. H. Lin, Y. K. Huang, and C. K. Sun. Spectral analysis of high-harmonic coherent acoustic phonons in piezoelectric semiconductor multiple quantum wells. *Phys. Rev. B*, 67:121303, 2003.

[181] I. Bozovic, M. Schneider, Y. Xu, R. Sobolewski, Y. H. Ren, G. Lupke, J. Demsar, A. J. Taylor, and M. Onellion. Long-lived coherent acoustic waves generated by femtosecond light pulses. *Phys. Rev. B*, 69:132503, 2004.

[182] A. A. Kolomenskii, S. N. Jerebtsov, H. D. Liu, H. Zhang, Z. X. Ye, Z. P. Luo, W. H. Wu, and H. A. Schuessler. Observation of coherent acoustic and optical phonons in bismuth nanowires by a femtosecond pump-probe technique. *J. Appl. Phys.*, 104:103110, 2008.

[183] A. Bruchhausen, R. Gebs, F. Hudert, D. Issenmann, G. Klatt, A. Bartels, O. Schecker, R. Waitz, A. Erbe, E. Scheer, J.-R. Huntzinger, A. Mlayah, and T. Dekorsy. Subharmonic resonant optical excitation of confined acoustic modes in a free-standing semiconductor membrane at ghz frequencies with a high-repetition-rate femtosecond laser. *Phys. Rev. Lett.*, 106:077401, 2011.

[184] N. V. Chigarev, D. Y. Paraschuk, X. Y. Pan, and V. E. Gusev. Coherent phonon emission in the supersonic expansion of photoexcited electron-hole plasma in ge. *Phys. Rev. B*, 61:15837, 2000.

[185] N. P. Butch, K. Kirshenbaum, P. Syers, A. B. Sushkov, G. S. Jenkins, H. D. Drew, and J. Paglione. Strong surface scattering in ultrahigh-mobility bi_2se_3 topological insulator crystals. *Phys. Rev. B*, 81(24):241301, Jun 2010.

[186] S. D. George, S. Augustine, E. Mathai, P. Radhakrishnan, V. P. N. Nampoori, and C. P. G. Vallabhan. Effect of Te doping on thermal diffusivity of Bi_2Se_3 crystals: A study using open cell photoacoustic technique. *Phys. Status Solidi A*, 196:384, 2003.

[187] H. Zeng, J. Dai, W. Yao, D. Xiao, and X. Cui. Valley polarization in MoS_2 monolayers by optical pumping. *Nat. Nanotechnol.*, 7:490–493, 2012.

[188] K. F. Mak, K. He, J. Shan, and T. F. Heinz. Control of valley polarization in monolayer MoS_2 by optical helicity. *Nat. Nanotechnol.*, 7:494–498, 2012.

[189] G. Sallen, L. Bouet, X. Marie, G. Wang, C. R. Zhu, W. P. Han, Y. Lu, P. H. Tan, T. Amand, B. L. Liu, and B. Urbaszek. Robust optical emission polarization in MoS_2 monolayers through selective valley excitation. *Phys. Rev. B*, 86:081301, 2012.

[190] A. Ramasubramaniam. Large excitonic effects in monolayers of molybdenum and tungsten dichalcogenides. *Phys. Rev. B*, 86:115409, 2012.

[191] J. S. Ross, S. Wu, H. Yu, N. J. Ghimire, A. M. Jones, G. Aivazian, J. Yan, D. G. Mandrus, D. Xiao, W. Yao, and X. Xu. Electrical control of neutral and charged excitons in a monolayer semiconductor. *Nat. Commun.*, 4:1474, 2013.

[192] H.-P. Komsa and A. V. Krasheninnikov. Effects of confinement and environment on the electronic structure and exciton binding energy of MoS_2 from first principles. *Phys. Rev. B*, 86:241201, 2012.

[193] A. R. Beal and H. P. Hughes. Kramers-Kronig analysis of the reflectivity spectra of 2H-MoS_2, 2H-$MoSE_2$ and 2H-$MoTe_2$. *J. Phys. C: Solid State Phys.*, 12:881–890, 1979.

[194] A. M. Jones, H. Y. Yu, N. J. Ghimire, S. F. Wu, G. Aivazian, J. S. Ross, B. Zhao, J. Q. Yan, D. G. Mandrus, D. Xiao, W. Yao, and X. D. Xu. Optical generation of excitonic valley coherence in monolayer WSe_2. *Nat. Nanotechnol.*, 8:634, 2013.

[195] R. Wang, B. A. Ruzicka, N. Kumar, M. Z. Bellus, H.-Y. Chiu, and H. Zhao. Ultrafast and spatially resolved studies of charge carriers in atomically thin molybdenum disulfide. *Phys. Rev. B*, 86:045406, 2012.

[196] H. Shi, R. Yan, S. Bertolazzi, J. Brivio, B. Gao, A. Kis, D. Jena, H. G. Xing, and L. Huang. Exciton dynamics in suspended monolayer and few-layer MoS_2 2D crystals. *ACS Nano*, 7:1072, 2012.

[197] S. Sim, J. Park, J.-G. Song, C. In, Y.-S. Lee, H. Kim, and H. Choi. Exciton dynamics in atomically thin MoS_2: Interexcitonic interaction and broadening kinetics. *Phys. Rev. B*, 88:075434, 2013.

[198] Q. Bao, H. Zhang, Y. Wang, Z. Ni, Y. Yan, Z. X. Shen, K. P. Loh, and D. Y. Tang. Atomic layer graphene for the mode locking of fiber lasers. *Adv. Funct. Mater.*, 19:3077–3083, 2009.

[199] M. D. McGehee and A. J. Heeger. Semiconducting (conjugated) polymers as materials for solid-state lasers. *Adv. Mater.*, 12:1655, 2000.

[200] A. Kohler, J. S. Wilson, and R. H. Friend. Fluorescence and phosphorescence in organic materials. *Adv. Mater.*, 14:701, 2002.

[201] A. Suna. Kinematics of exciton-exciton annihilation in molecular crystals. *Phys. Rev. B*, 1:1716, 1970.

[202] L. Luer, S. Hoseinkhani, D. Polli, J. Crochet, T. Hertel, and G. Lanzani. Size and mobility of excitons in (6,5) carbon nanotubes. *Nat. Phys.*, 5:54, 2009.

[203] Y. Z. Ma, L. Valkunas, S. L. Dexheimer, S. M. Bachilo, and G. R. Fleming. Femtosecond spectroscopy of optical excitations in single-walled carbon nanotubes: Evidence for exciton-exciton annihilation. *Phys. Rev. Lett.*, 94:157402, 2005.

[204] L. M. Smith, D. R. Wake, J. P. Wolfe, D. Levi, M. V. Klein, J. Klem, T. Henderson, and H. Morkoç. Picosecond imaging of photoexcited carriers in quantum wells: Anomalous lateral confinement at high densities. *Phys. Rev. B*, 38:5788, 1988.

[205] P. Tonndorf, R. Schmidt, P. Bottger, X. Zhang, J. Borner, A. Liebig, M. Albrecht, C. Kloc, O. Gordan, D. R. T. Zahn, S. M. de Vasconcellos, and R. Bratschitsch. Photoluminescence emission and Raman response of monolayer MoS_2, $MoSe_2$, and WSe_2. *Opt. Express*, 21:4908, 2013.

[206] H. T. Wang, D. S. Kong, P. Johanes, J. J. Cha, G. Y. Zheng, K. Yan, N. A. Liu, and Y. Cui. $MoSe_2$ and WSe_2 nanofilms with vertically aligned molecular layers on curved and rough surfaces. *Nano Lett.*, 13:3426, 2013.

[207] D. S. Kong, H. T. Wang, J. J. Cha, M. Pasta, K. J. Koski, J. Yao, and Y. Cui. Synthesis of MoS_2 and $MoSe_2$ films with vertically aligned layers. *Nano Lett.*, 13:1341, 2013.

[208] S. Larentis, B. Fallahazad, and E. Tutuc. Field-effect transistors and intrinsic mobility in ultra-thin $MoSe_2$ layers. *Appl. Phys. Lett.*, 101:223104, 2012.

[209] R. Fivaz and E. Mooser. Mobility of charge carriers in semiconducting layer structures. *Phys. Rev*, 163:743, 1967.

[210] A. Rettenberger, P. Leiderer, M. Probst, and R. Haight. Ultrafast electron transport in layered semiconductors studied with femtosecond-laser photoemission. *Phys. Rev. B*, 56:12092, 1997.

[211] B. Radisavljevic and A. Kis. Mobility engineering and a metal-insulator transition in monolayer MoS_2. *Nat. Mater.*, 12:815, 2013.

[212] H. Qiu, T. Xu, Z. Wang, W. Ren, H. Nan, Z. Ni, Q. Chen, S. Yuan, F. Miao, F. Song, G. Long, Y. Shi, L. Sun, J. Wang, and X. Wang. Hopping transport through defect-induced localized states in molybdenum disulphide. *Nat. Commun*, 4:2642, 2013.

[213] W. J. Zhang, J. K. Huang, C. H. Chen, Y. H. Chang, Y. J. Cheng, and L. J. Li. High-gain phototransistors based on a CVD MoS_2monolayer. *Adv. Mater.*, 25:3456, 2013.

[214] R. S. Sundaram, M. Engel, A. Lombardo, R. Krupke, A. C. Ferrari, P. Avouris, and M. Steiner. Electroluminescence in single layer MoS_2. *Nano Lett.*, 13:1416, 2013.

[215] S. Tongay, J. Zhou, C. Ataca, J. Liu, J. S. Kang, T. S. Matthews, L. You, J. B. Li, J. C. Grossman, and J. Q. Wu. Broad-range modulation of light emission in two-dimensional semiconductors by molecular physisorption gating. *Nano Lett.*, 13:2831, 2013.

[216] Z. Y. Zhu, Y. C. Cheng, and U. Schwingenschlogl. Giant spin-orbit-induced spin splitting in two-dimensional transition-metal dichalcogenide semiconductors. *Phys. Rev. B*, 84:153402, 2011.

[217] A. Molina-Sanchez, D. Sangalli, K. Hummer, A. Marini, and L. Wirtz. Effect of spin-orbit interaction on the optical spectra of single-layer, double-layer, and bulk MoS_2. *Phys. Rev. B*, 88:045412, 2013.

[218] L. F. Sun, J. X. Yan, D. Zhan, L. Liu, H. L. Hu, H. Li, B. K. Tay, J. L. Kuo, C. C. Huang, D. W. Hewak, P. S. Lee, and Z. X. Shen. Spin-orbit splitting in single-layer MoS_2 revealed by triply resonant Raman scattering. *Phys. Rev. Lett.*, 111:126801, 2013.

[219] T. Cheiwchanchamnangij and W. Lambrecht. Quasiparticle band structure calculation of monolayer, bilayer, and bulk MoS_2. *Phys. Rev. B*, 85:205302, 2012.

[220] W. X. Feng, Y. G. Yao, W. G. Zhu, J. J. Zhou, W. Yao, and D. Xiao. Intrinsic spin hall effect in monolayers of group-VI dichalcogenides: A first-principles study. *Phys. Rev. B*, 86:165108, 2012.

[221] Z. Li and J. P. Carbotte. Longitudinal and spin-valley hall optical conductivity in single layer MoS_2. *Phys. Rev. B*, 86:205425, 2012.

[222] X. Li, F. Zhang, and Q. Niu. Unconventional quantum Hall effect and tunable spin Hall effect in Dirac materials: Application to an isolated MoS_2 trilayer. *Phys. Rev. Lett.*, 110:066803, 2013.

[223] W. Y. Shan, H. Z. Lu, and D. Xiao. Spin hall effect in spin-valley coupled monolayers of transition metal dichalcogenides. *Phys. Rev. B*, 88:125301, 2013.

[224] G. Kioseoglou, A. T. Hanbicki, M. Currie, A. L. Friedman, D. Gunlycke, and B. T. Jonker. Valley polarization and intervalley scattering in monolayer MoS_2. *Appl. Phys. Lett.*, 101:221907, 2012.

[225] H. Zeng, J. Dai, W. Yao, D. Xiao, and X. Cui. Valley polarization in MoS_2 monolayers by optical pumping. *Nat. Nanotechnol.*, 7:490, 2012.

[226] K. F. Mak, K. He, J. Shan, and T. F. Heinz. Control of valley polarization in monolayer MoS_2 by optical helicity. *Nat. Nanotechnol.*, 7:494, 2012.

[227] S. F. Wu, C. M. Huang, G. Aivazian, J. S. Ross, D. H. Cobden, and X. D. Xu. Vapor-solid growth of high optical quality MoS_2 monolayers with near-unity valley polarization. *ACS Nano*, 7:2768, 2013.

[228] S. Wu, J. S. Ross, G.-B. Liu, G. Aivazian, A. Jones, Z. Fei, W. Zhu, D. Xiao, W. Yao, D. Cobden, and X. Xu. Electrical tuning of valley magnetic moment through symmetry control in bilayer MoS_2. *Nat. Phys.*, 9:149, 2013.

[229] D. Lagarde, L. Bouet, X. Marie, C. R. Zhu, B. L. Liu, T. Amand, P. H. Tan, and B. Urbaszek. Carrier and polarization dynamics in monolayer mos_2. *Phys. Rev. Lett.*, 112:047401, 2014.

[230] C. Mai, A. Barrette, Y. Yu, Y. G. Semenov, K. W. Kim, L. Cao, and K. Gundogdu. Many-body effects in valleytronics: Direct measurement of valley lifetimes in single-layer MoS_2. *Nano Lett.*, 14:202, 2013.

[231] Q. Wang, S. Ge, X. Li, J. Qiu, Y. Ji, J. Feng, and D. Sun. Valley carrier dynamics in monolayer molybdenum disulfide from helicity-resolved ultrafast pump-probe spectroscopy. *ACS Nano*, 7:11087, 2013.

[232] S. Schmitt-Rink, D. A. B. Miller, and D. S. Chemla. *Phys. Rev. B*, 35:8113, 1987.